The Design of a Tagged Photon Spectrometer and its use in measuring the photodisintegration of the Deuteron in the energy range 80 - 135 MeV.

Thesis

Submitted by

Alan McPherson, B.Sc. (Hons.)

for the degree of

Doctor of Philosophy

Department of Natural Philosophy

University of Glasgow

OCTOBER 1989

To Gran and Mamie

ABSTRACT

The work described in this thesis was conducted at the Kelvin Laboratory, University of Glasgow and at the Institut Für Kernphysik der Universität Mainz, between October 1982 and January 1986.

Presented in this thesis are new results on the photodisintegration of the deuteron in the photon energy range 80 - 135 MeV, the intermediate energy range, using *tagged* bremsstrahlung photons. This thesis also describes the design and construction details of the *tagged* photon spectrometer employed for the above measurements. The *tagged* photon spectrometer was specifically designed for the 180 MeV electron racetrack microtron at the Institut Für Kernphysik der Universität Mainz, MAMI - A. The system was designed to enable bremsstrahlung photons in the energy range 80 - 174 MeV to be *tagged* at fluxes of up to $5 \times 10^7 s^{-1}$.

Using the *tagged* photon spectrometer the differential cross section for the reaction $D(\gamma, p)n$ was measured for the photon energies in the range 80 - 135 MeV, and for the angular range $\theta_p = 50°$ - $130°$ the center of mass proton emission angle. Results are presented for the selected photon energies of 87,95,104,113,122 and 128 MeV for the complete angular range. Measurements were performed simultaneously, for the quoted energy and angular ranges. The cross section information was then extracted using a purpose written data analysis program, which used time correlations and kinematic constraints to identify deuteron type events.

Comparisons were made between several well known theoretical descriptions of deuteron photodisintegration and the presented data. The magnitude of the errors assigned to the measurements prevented any reliable indication in favour of one approach over another. However, the possibilities of a measurement of the cross section to an accuracy of better than 5 % look very promising using this apparatus.

DECLARATION

The data and equipment design presented in this thesis were produced by a collaboration between the nuclear structure research groups at the Universities of Glasgow, Edinburgh and Mainz, in which I undertook the principal rôle. The analysis and interpretation of the data is entirely my own work. This thesis has been composed by myself.

Alan McPherson

ACKNOWLEDGEMENTS

During the time I have spent at the Kelvin Laboratory, University of Glasgow and at the Institut Für Kernphysik der Universität Mainz, many people have provided me with encouragement, support, understanding and much advice. I am extremely grateful for this support and encouragement, especially after the untimely deaths of both my mother and father during the later stages of my studies and the writing of this thesis. I hope that all those concerned are already in no doubt of my profound appreciation.

My thanks must begin with my two supervisors at the Kelvin Laboratory, Dr. Jim Kellie and Dr. Sam Hall. Their encouragement and sound advice has been of great importance in the completion of this experimental investigation in photonuclear physics. I hope that their dedication to experimental physics and to teaching, never faulters and that they can find some small reward in the production of this thesis. Without all their hard work and long hours on the *tagged* photon spectrometer, it would surely never have come into being.

I acknowledge the financial support of the Science and Engineering Research Council to enable me to complete my studies. I would also like to acknowledge Professor E. Laing who as head of the Department of Natural Philosophy of the Univerity of Glasgow, funded my attendence at several conferences and schools, the Institute of Physics should also be mentioned in this regard.

I would also like to acknowledge the assistance of Professor J. Reid and Dr R.O. Owens, who in there capacity as directors of the Kelvin Laboratory provided the facilities of the Kelvin Laboratory, and access to the skilled technical support present at the Laboratory. Arrick Wilkinson and Andy Sibbald in particular

deserve thanks, for the work in maintaining the VAX 11/780 for all of its many users.

I am grateful to Professor Ehrenberg and Professor Schoch at the Institut Für Kernphysik, for affording me the use of the Institutes facilities. During my short time at the Institute the staff and technicians were of great assistance, especially when I was forced to employ my undistinguished German. Special thanks are due to the Institutes members of the collaboration, Professor Bertolt Schoch, Johannes Vogt, Franz Zettl, Guido Leisenfeld and Reinhard Beck.

A special mention should be made to my fellow research students at the Kelvin Laboratory. If humour and good fellowship were a source of income, then those of us who have been lucky enough to have been at the Kelvin Laboratory, would be rich indeed. My thanks to Dr. Ian Anthony, Dr. Gary Miller, Dr. Sung Lai Wang, Dr. Peter Wallace and Dr. Steven Dancer. It is not just research students who should be mentioned in this regard, so my thanks to Dr. Cameron McGeorge and Dr. John Annan.

During the past 10 years I have had the good fortune to reside with my grandmother and aunt, Gran and Mamie, to whom this thesis is dedicated. There constant support and encouragement throughout my graduate and undergraduate studies have been very special to me and always will. I cannot say more.

Finally I would like to thank my wife Anne, for always being there. This thesis is as much through your hard work as mine. I love you.

Contents

Chapter 1

Photo induced Reactions - Measurement Techniques

1.1 Introduction

This thesis describes the design and construction of a *tagged* photon spectrometer, which has been used in conjuction with the 180 MeV electron microtron at the Institut Für Kernphysik in Mainz, West Germany. The system was designed to perform experiments on photonuclear reactions in the intermediate energy region, and produces *tagged* photons at rates of up to $5 \times 10^7 s^{-1}$ in the energy range 80 - 174 MeV. This thesis describes the first experiment performed using the *tagged* spectrometer, which was an investigation into the photodisintegration of the deuteron in the photon energy range 80 - 135 MeV.

In the following sections of this chapter the motivation for using *tagged* sources will be discussed, and several methods of *tagging* photons examined.

1.1.1 Photodisintegration Experiments - General

The electromagnetic interaction has several attractive features as a means of investigating nuclear properties. Since the interaction is weak when compared to the strong interaction, the presence of an electromagnetic field does not strongly perturb the nuclear system under investigation, and the electromagnetic probe can, either in the form of real or virtual photons, penetrate deep into the interior of a nuclear system. However, for many years there have been difficulties associated with the production of real photon fluxes which have prevented experimentalists realising the full potential of the electromagnetic probe. In particular it has proved difficult to obtain real photon fluxes of known energy, to enable the identification of reaction channels, known magnitude to simplify normalisation procedures, and sufficient intensity to enable reactions with small cross sections to be examined in a reasonable timescale.

One commonly used method for the production of high energy real photon fluxes is that of electron bremsstrahlung. Bremsstrahlung is produced when an electron is scattered on a nuclear charge, and the resulting loss of energy by the electron is transformed into a photon. The photon energy is given by

$$E_\gamma = E_o - E' \tag{1.1}$$

where E_o is the incident electron energy and E' is the scattered electron energy. However the photon spectrum produced from electron bremsstrahlung is continuous, with photon energies ranging downwards from E_o (the end point energy) to lower energies. To obtain photons of known incident energy from this

type of spectrum, a subtraction or unfolding technique[1][2] is used. Here the same experiment is performed for several different, but closely spaced end point energies. If two bremsstrahlung spectra are superimposed on each other, one from an end point energy of E and the second from an end point of $E - \Delta E$, subtraction of these spectra produces a photon spectrum peaked within the range E to $E - \Delta E$. If the reaction product spectra are similarly subtracted, it can be inferred that the resulting spectra was produced by photons in the defined energy range.

It is obvious that this method is very time consuming. The experiment is performed several times, yet only a fraction of the data is useful. In addition the magnitude of the photon flux, required to normalise the resultant cross section, is calculated from the calculated shape[3] of the bremsstrahlung spectrum at the end point energy, where the spectrum is varying most rapidly. This results in the estimated magnitude of the photon flux being subject to large systematic errors.

In an attempt to circumvent this problem, several very specific experiments have used specialised techniques (which did not rely on a precise knowledge of the photon flux) to measure absolute photo cross sections. One of the most elegant was the experiment of Hughes[4] *et al.* Hughes' experiment was an absolute measurement of the differential cross section of the deuteron in the intermediate energy range, at the angle of 0° for the outgoing protons. Unlike previous experiments, although Hughes made use of a bremsstrahlung photon beam, the measurement was independent of the shape of the bremsstrahlung spectrum. This was achieved by the simultaneous measurement of the deuteron photodisintegration cross section and the known cross section for Compton scattering,

which produces recoil electrons, at the same forward angle. Since the Compton effect cross section is well known, by taking the ratio of the two measured quantities the photodisintegration cross section could be deduced. Although the experimental difficulties of measurements at 0° are many, the experimental results quote a 6 % accuracy for the measurement. Clearly the reason for the quality of the experimental results is that the measurement is independent of any knowledge of the shape or magnitude of the bremsstrahlung spectrum.

We can see that to make photodisintegration experiments more accurate, evaluation of the photon energy and flux must not be dependent upon the calculation of the magnitude or shape of the bremsstrahlung spectrum. This independence may be achieved in two ways; as in the experiment by Hughes by comparing a known cross section to that of the desired cross section, or alternatively we can attempt to measure the photon flux directly. It was to resolve this problem of the determination of the photon energy and photon flux, that the technique of photon *tagging* was first investigated.

1.2 Tagged Photon Techniques

Photon *tagging* is a technique which can be used to produce quasi-monochromatic photons. This is achieved by the detection of a secondary product, from the process in which the photon originated. The detector used for this purpose is called the *tagging* detector. The energy of a single photon can be determined by measuring the energy or angle of the secondary product in the *tagging* detector. If the secondary product is also coincident with a product from the target intercepting the photon flux, then if random coincidences are discounted, it can be inferred that the reaction product was produced by the original single photon.

If the number of events in the *tagging* detector is counted, the corresponding number of incident photons on the target should be known. However, not all photons produced may be incident on the target due to collimation of the photon beam. It is therefore important that the probability, that an event detected in the *tagging* detector can be associated with a photon incident on the target, is known accurately, since then the magnitude of the incident photon flux would be known. This factor is called the *tagging* efficiency and should optimally be as close to 1 as possible.

In most cases the *tagging* efficiency of a system can be measured. For example by using a photon detector of a known efficiency placed directly in the photon beam, the efficiency can be evaluated by recording the count rates in the *tagging* detector, photon detector and the coincidence rate between the two. To provide a measure of the background rates the measurement is also carried out in the absence of the photon beam.

The *tagging* efficiency is then given by

$$E = \frac{I_m}{L_m - (t_m/t_b)L_b} \tag{1.2}$$

where I_m is the rate of coincidences between the photon detector and the *tagging* detector, L_m and L_b are the rates of the *tagging* detector for the measurement and the background respectively, t_m and t_b being the live time for the measurement and background data respectively.

The useful flux of the *tagged* photon beam produced is restricted by the number of random coincidences and by the permissible counting rate of the *tagging* detector. There are two distinct sources of random coincidences. Firstly, coincidences where two events are detected within the coincidence resolving time of the system. Such events have to be rejected as they result in ambiguity in the photon energy. Secondly, conicidences where the particle detector event is produced by a photon outside the energy range covered by the *tagging* detector, thus giving a completely spurious photon energy. Such events may be able to be rejected on kinematic grounds.

The performance of a *tagging* system can be assessed in terms of the magnitude of the *tagged* photon flux, the *tagging* efficiency and the relative real to random rates. Indeed, the optimisation of these quantities is probably the most important task of designing a *tagging* facility.[5][6][7]

In recent times three main tagging techniques have been used[8][9];

- Laser backscattering
- In-flight positron annihilation
- Tagged bremsstrahlung.

In the following sections the advantages and disadvantages of the various methods will be discussed and their performance characteristics examined.

1.2.1 Laser Backscattering

The basis of this method, is relativistic Compton scattering. A photon produced from a relatively low energy laser, can acquire energy by being involved in large angle Compton scattering. When a laser beam is directed onto an ultra-relativistic electron beam at a shallow angle, photons which emerge in the direction of the electron beam have been backscattered, as shown in Fig. 1.1.

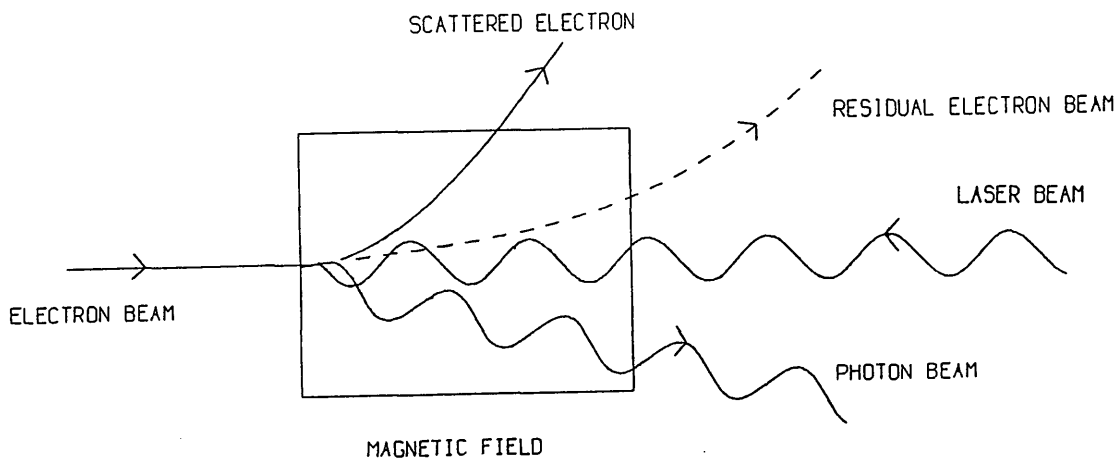

Figure 1.1 Schematic representation of laser backscattering technique.

The residual electron beam and the Compton electrons are magnetically deflected from the beam path, so that only the high energy backscattered photons are incident on the photonuclear target.

The Compton electrons are then momentum analysed. A good approximation[10] for the energy of a backscattered photon, E_γ, is given by

$$E_\gamma = \frac{4\gamma^2 E_L}{\frac{4\gamma E_L}{m_e c^2} + \Theta^2\gamma^2 + 1} \tag{1.3}$$

where Θ is the angle the photon emerges at with respect to the electron direction, E_L is the energy of the laser beam, and γ is given by

$$\gamma = \frac{E_o}{m_e c^2} \tag{1.4}$$

where E_o is the primary beam energy, c is the speed of light and m_e is the rest mass of the electron. From an examination of these equations we can see that E_o must be very large indeed, if photons in the intermediate energy range are to be produced. In fact an electron beam of several GeV is required.

The equation also indicates that good energy resolution is possible, if collimation of the photon beam minimises $\delta\Theta$ the angular acceptance and if the energy and angular spread of the electron beam is small. However, this reduces the *tagged* flux.

Alternatively, the energy information can be obtained from the scattered electron energy, E', since

$$E_\gamma = E_o - E' \tag{1.5}$$

This approach provides a moderate photon energy resolution, but results in larger *tagged* fluxes. The *tagged* flux is dependent on the electron beam current, the power of the laser and the collimation needed.

Tagged photon beams, produced using this method, have up to now had the serious drawback of small *tagged* photon fluxes. However, a major advantage of the laser backscattering technique is that a polarised laser beam may be employed as the initial photon source, and since the initial polarisation is preserved in the scattering process, in practice 75 - 100 % linear polarisation can be obtained.

Examples of this kind of facility are found in use at Frascati[11][12][13] and Brookhaven[14]. Presently at Frascati, the Adone storage ring is used to provide a high duty factor electron beam. The laser used is a high powered Ar - Ion laser. Using a 1.5 GeV beam, photon energies of 78.5 MeV are possible with a *tagged* photon flux of $2 \times 10^5 s^{-1}$, an energy resolution of 8 % and a polarisation of 100 % .

1.2.2 Positron Annihilation

This method of producing *tagged* photons, a technique used at Saclay, uses the gamma rays emitted from electron positron annihilation. If the annihilation occurs when the electron positron pair is at rest, two 511 keV gamma rays would be produced, a total energy equal to that of the rest energies of the constituents. However, more energy can be introduced into the reaction if the annihilation

takes place in-flight using highly relativistic positrons. In this case, the resultant photons are Doppler shifted in energy, one to a higher energy and one to a lower energy. This is shown schematically in Fig. 1.2.

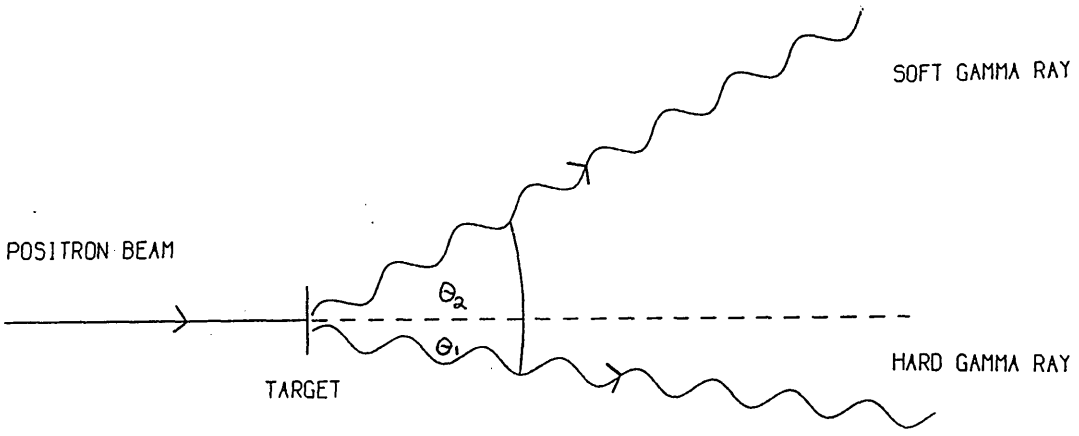

Figure 1.2 Schematic representation of in-flight positron annihlation *tagging* technique

The gamma ray energy, of the hard or higher energy photon is given by[10]

$$E_{\gamma_{HIGH}} = E_+ - \frac{2mc^2}{\theta^2_{2(\gamma_{LOW})}} \tag{1.6}$$

where E_+ is the positron energy, and $\theta_{2(\gamma_{LOW})}$ is the emisson angle of the soft or low energy photon. The high energy photons of interest are emitted at forward angles, and in coincidence with the lower energy photons. It is the lower energy photon which is used as the *tagging* mechanism.

The positrons are produced by allowing a high energy electron beam to be

incident on a converter of high Z. However the efficiency of the positron production is low; the reduction in the beam is around 10^{-4}. The positron beam is then incident on an annihilation target to produce the coincident photon pairs. The high energy photons are then collimated before interacting in the target.

This technique presents several difficulties to the experimentalist. Photons from the annihilation process are accompanied by bremsstrahlung photons from the annihilation target. It is therefore necessary to take careful measures to suppress the large bremsstrahlung background while keeping a large proportion of the annihilation photons. Count rates of *tagged* photons on the photonuclear target are also restricted by the instantaneous count rates possible in the low energy gamma ray detector. The resultant *tagged* photon flux can be as low as $10^4 s^{-1}$ when a conventional pulsed electron beam accelerator is used. The situation however would be greatly improved if a high duty factor accelerator were to be employed. One major disadvantage of photon beams produced by this method is that no polarisation can be imparted to the photons.

1.2.3 Tagged Bremsstrahlung

Using this technique, detection of scattered electrons in the bremsstrahlung process is used to provide an experimental signal to *tag* individual photons. When a high energy electron beam is incident upon a thin radiator, the high energy bremsstrahlung photons are emitted predominately in the primary beam direction. The incident electron beam and the bremsstrahlung scattered electrons are then passed through a magnet system, which separates the electrons from the photon beam direction. The bremsstrahlung scattered electrons are momentum

analysed by the magnet system or spectrometer, and detected on the focal plane of the spectrometer magnet. This allows both timing and energy information on the photon to be obtained. A schematic diagram of the process is shown in Fig. 1.3.

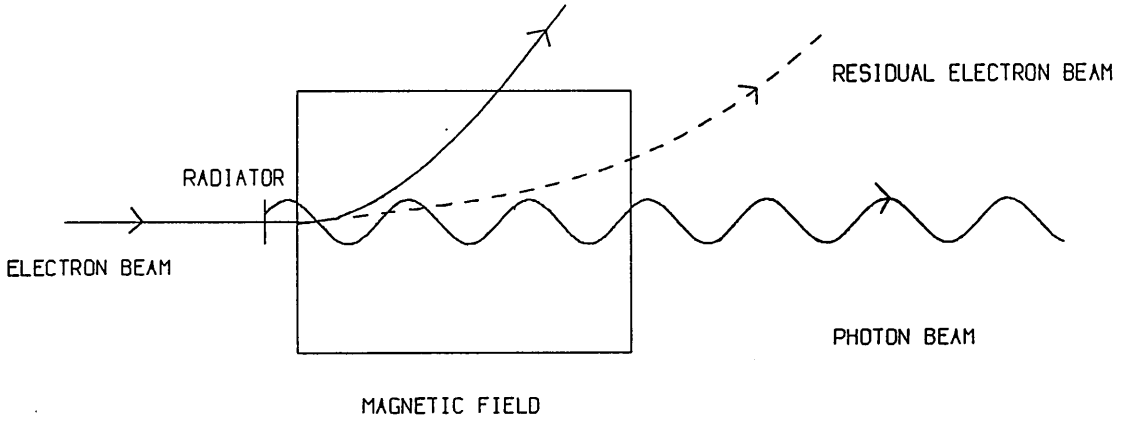

Figure 1.3 Schematic representation of electron bremsstrahlung *tagging* technique.

The energy of the bremsstrahlung photon, E_γ, is given by

$$E_\gamma = E_o - E_e \tag{1.7}$$

where E_o is the primary beam energy, and E_e the detected electron energy. In the design of such a spectrometer, both the acceptance of a large range of electron energies and the provision of a reasonable energy resolution are essential. Furthermore, detection of the polarisation of the *tagged* photon beam is possible with careful design of the spectrometer magnets. To provide the polarisation

information on the *tagged* photons, it has been shown[15] that the spectrometer magnets must be capable of determining the angle at which the scattered electron emerges from the bremsstrahlung radiator. Using this technique the degree of linear polarisation can be as much as 60 % .

To make best use of the *tagged* photon technique either a continuous electron beam or a beam with a high duty factor is desirable. Otherwise the ratio of the real to random rates of the detected events will be poor. Additionally, if the beam is pulsed, then the resultant *tagged* count rate will be more seriously restricted by the instantaneous count rate possible in the focal plane detectors.

The bremsstrahlung radiator used is also important. This is necessarily thin ($\approx 10^{-5}$ radiation lengths) to reduce focal plane background due mainly to Möller scattering and multiple scattering of electrons in the radiator. A thin radiator also minimises angular spreading of the bremsstrahlung photons and scattered electrons, which is important if the system is to produce an acceptable value of the *tagging* efficiency.

Tagging bremsstrahlung photons is the most widely applied of the three methods, of obtaining *tagged* photons. There are several examples of such facilities which have been used in recent years, such as the systems at Bonn[16], Sendai[17] and Ilinois[18]. The *tagging* system at Sendai has been able to produce a *tagged* photon beam of $3 \times 10^6 s^{-1}$, with a tagging efficiency of 50 % at an energy resolution of 3 %. This was achieved using a beam stretcher to produce a high duty factor beam from a pulsed linear accelerator. The characteristics of the Bonn *tagging* system, which used the 500 MeV synchrotron at that facility are somewhat different. Here the *tagging* efficiency is 98 % over a wide range

of photon energies with an energy resolution of 2 % . However, the *tagged* photon flux is only $2 \times 10^5 s^{-1}$. The duty cycle of the Bonn synchroton is 0.03, which accounts for the low *tagged* flux.

1.2.4 Comparison of Tagging Techniques

The principles of the three *tagging* techniques described have been known for many years. However, it was only with the advent of DC accelerators such as storage rings or microtrons that photon *tagging* has became an important means of producing well defined photon fluxes. Since the fraction of random events in a *tagging* measurement is proportional to the instantaneous electron current, a facility based on a DC machine will always provide better data then one dependent on a pulsed machine having the same average current.

The benefits of using a continuous wave beam or a high duty factor beam, can be utilised by each of the methods, to improve the magnitude of the *tagged* photon flux, reduce beam related background and hence reduce random coincidence events. However, it is *tagged* bremsstrahlung which is inherently the most attractive option. It employs well proven technology and matches or can improve upon the performance characteristics of the other two methods. In particular, as will be demonstrated in this thesis, the *tagged* bremsstrahlung facilities can produce a *tagged* flux 10 - 100 time larger than the other methods considered. Additionally, partially polarised beams are available at these larger fluxes.

Chapter 2

The Tagged Photon Spectrometer

2.1 Introduction

The *Tagged Photon Spectrometer*, shown in Fig. 2.1, is situated in the magnet hall of the accelerator complex at the Institute Für Kernphysik in Mainz, and occupies a position in the beam line of MAMI-A the 180 MeV racetrack microtron. In following sections of this chapter the racetrack microtron and *tagging* spectrometer will be described. The description of the spectrometer is divided into two sections, one on the spectrometer magnet system and one on the focal plane detector which acts as the *tagging* detector of the system. Finally, the characteristics of the *tagged* photon beam produced from the combination of microtron and spectrometer are presented.

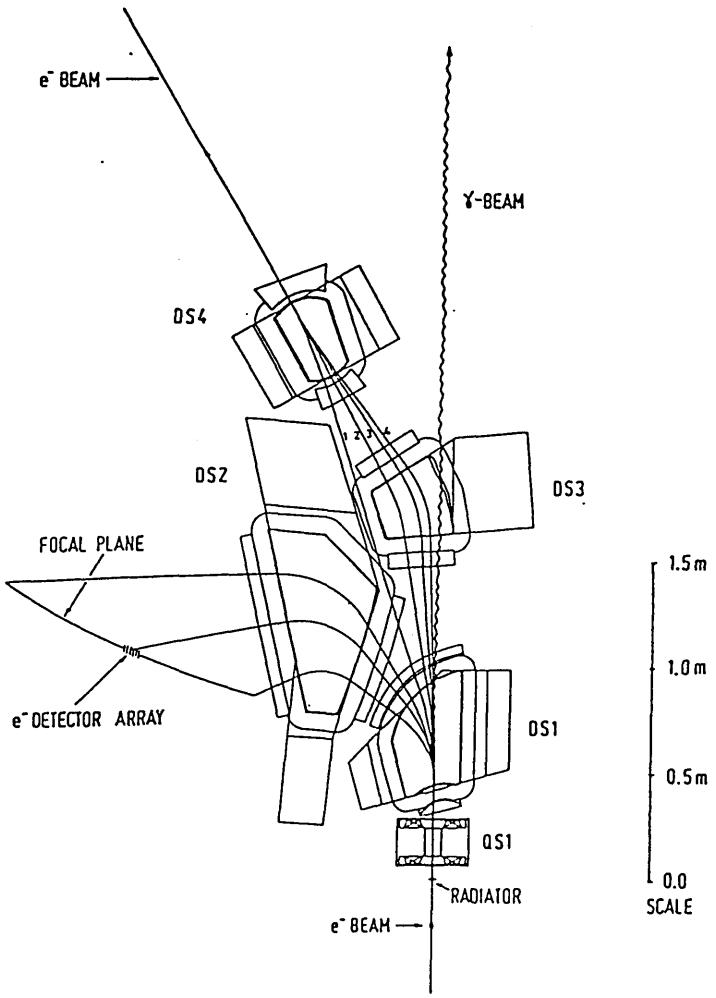

Figure 2.1 A plan view of the Mainz microtron *tagged* photon spectrometer, showing the focal plane position, and the four main beam trajectories through the system.

2.2 The Racetrack Microtron

The general lay-out of a microtron is shown in Fig. 2.2. Conventional accelerators produce electron pulses which have a fine microstructure consisting of a series of sharp peaks which are very close together(300pS). However, this output can only be sustained for a very short time, typically a few μS. The electron beam in a conventional accelerator is accelerated to hundreds of MeV in a very short distance, requiring a great deal of power which must be dissipated before the next electron pulse. Microtrons accelerate electrons very gradually over a very long path length. If this were performed on a linear accelerator the length of the accelerator would be prohibitive. In the racetrack microtron, the inherent problem of the length of a low power accelerator required for a reasonable energy gain, has been overcome by using strong end magnets to *fold* the beam into expanding loops, as shown in Fig. 2.2. As can be seen in Fig. 2.2 the expanding loops have a common side which is the accelerating section of the microtron. This need only be a low power linear accelerator, as shown in more detail in Fig. 2.3. Microtrons can be operated with a duty cycle of 100 % and in addition have a very good energy resolution, a very good emittance, and furthermore a high intensity output current is possible

The accelerator at the Institut Für Kernphysik in Mainz, which operates in continous wave (c.w.) mode[20], is a cascade of two racetrack microtrons with a Van de Graaff as a pre-accelerator. The Van de Graaff pre-accelerator injects a beam of some 2 MeV into the first racetrack microtron, the beam being brought to an energy of 14 MeV in 20 orbits. This is then used to feed the second

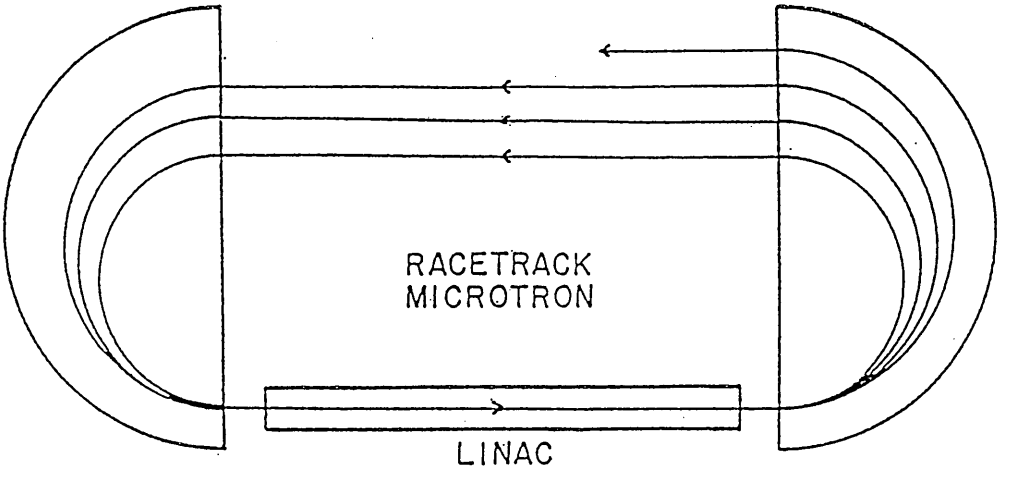

Figure 2.2 The expanding loops of the electron trajectory in a racetrack microtron.

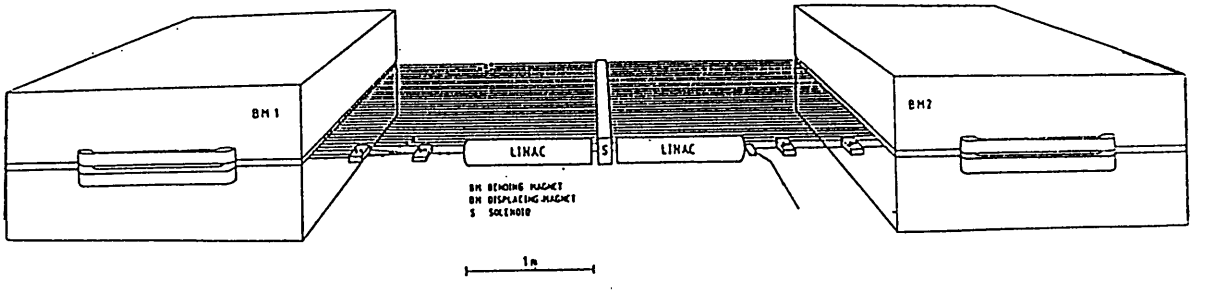

Figure 2.3 A racetrack microtron - general layout.

microtron stage, which brings the beam to an energy of 180 MeV in a further 43 orbits. A diagram of the accelerator layout is shown in Fig. 2.4.

Each racetrack microtron consists of two 180° bending magnets and a linear accelerator, the linear accelerator section of each microtron being fed by the same 50 kW c.w. klystron. Semicircular paths are described by the electrons in the two end magnets so that each orbit has the linear accelerator (linac) section in common, as shown. In each orbit the beam gains δE in energy which increases the orbit path length, by an integral number of r.f. path lengths of the linac, so that the beam is kept in phase. The 30 KeV energy spread in the 180 MeV beam of MAMI-A, is achieved by the good phase stability of the microtron. If an electron gains more than δE in energy, then it will describe a slightly larger semicircular path and will arrive later for the next linac traversal. This corresponds to a lower energy gain, and conversely if the energy gained is less than δE, then a higher energy gain results.

Due to the large number of orbits needed to provide the 180 MeV beam, it is inevitable that some orbit corrections will be necessary. The behaviour of the beam in each orbit is detected, by chopping the output beam of the Van de Graff using an electrostatic deflector. This produces pulses of 12 nS fwhm in duration. These electron pulses can then be detected by beam position monitors, placed at strategic sections along beam path. From the signals from the beam monitoring system, orbit corrections can be made by means of steering coils at either end of each return path. This optimisation of the beam is completed automatically by the computing system, an HP1000 microcomputer, or can be performed manually.

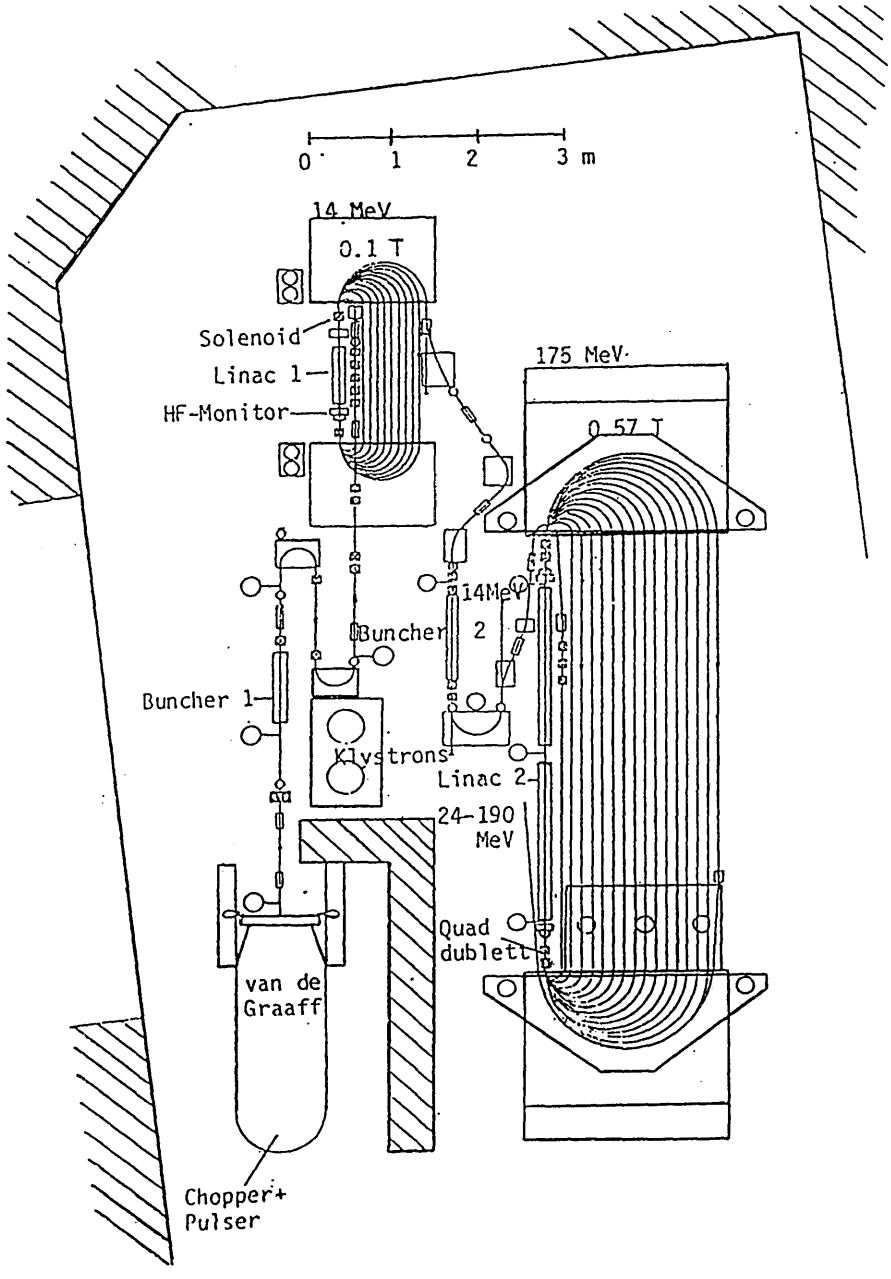

Figure 2.4 Plan view of the 180 MeV Mainz microtron, showing the Van de Graff pre-accelerator and the first and second stage racetrack microtrons.

The electron beam produced from the racetrack microtron has excellent characteristics, having an energy resolution of 30 keV in 180 MeV and an emittance of 0.04π mm.sr vertically and 0.09π mm.sr horizontally. This allows the production of an electron beam of typically 1 mm in diameter at the bremsstrahlung radiator of the *tagging* spectrometer. The maximum beam current provided by the system is $\approx$ 100 μA. However, for the purposes of *tagged* photon spectrometer, beam currents of 60 nA are sufficient to provide a *tagged* photon rate of several $\times 10^7$ per second.

2.3 The Magnetic Spectrometer

This section describes the magnetic spectrometer of the *tagging* facility, and is shown in Fig. 2.1. The magnet system which was designed[21] at the Kelvin Laboratory, Glasgow University, has two primary functions; firstly, to collect and analyse electrons scattered from the bremsstrahlung radiator, and secondly, to transport the residual beam away from the experimental area. As can be seen the spectrometer is of the quadrupole, dipole, dipole (QDD) type, with the other two dipoles in the system performing the beam transportation tasks. A QDD spectrometer was chosen as it provides certain desirable characteristics[22], needed to produce a *tagged* photon beam, namely;

- A large momentum acceptance, such that $\rho_{max} : \rho_{min} = 2 : 1$
- A large acceptance solid angle for the electrons within the momentum range being analysed, to provide a large *tagged* photon flux.
- Good electron energy resolution, of around 10^{-3}.
- A small spatial extent in the non-bend plane direction for electrons in the focal plane, to aid electron detection.
- A sufficiently compact system, to enable the target to be as close as possible to the radiator, to reduce the photon beam spot size.
- The use of two dipoles to facilitate the separation of the main beam from the momentum analysed electrons.

The bremsstrahlung radiator is situated 0.2 m from the first magnet the quadrupole QS1, which focuses the scattered electrons in the plane perpendicular to the bend of the incident beam, before entry into the dipoles DS1 and DS2. This focusing in the non-bend plane direction, increases the solid angle acceptance of the spectrometer. In addition the inclusion of an entrance quadrupole in the system aids the reduction of aberrations in the magnet optics. The magnetic spectrometer system is adjusted so that the incident electron beam, of energy E_o, only passes through DS1. The magnetic field of DS1 is set so that the second dipole DS2, analyses the bremsstrahlung recoil electrons in the energy bite from E_{max} to E_{min}, where $E_{max} : E_{min} = 2 : 1$.

Furthermore, for a given incident beam energy E_o, the range of the spectrometer may be altered by changing the ratio $E_o : E_{max}$. This then has the effect of changing the output trajectory of the main beam from DS1. Fig. 2.1 shows the four main beam trajectories used, resulting from four different ratios of $E_o : E_{max}$. Variations in the spectrometer resolution are presented in Table 2.1, for an incident beam energy of 180 MeV and three of the energy ranges which can be selected by the spectrometer. Another benefit of varying the value of $E_o : E_{max}$, is that a reasonable resolution can be maintained in all the spectrometer ranges. This can be illustrated in the following way;

The limiting value of the angular spread of the bremsstrahlung scattered electrons is given by the cone of half angle ϕ, where

$$\phi = \frac{4M_e k}{E_o E} \tag{2.1}$$

Tagging spectrometer resolution and image sizes								
Trajectory	E [MeV]	k [MeV]	β [mrad]	Electron resolution $R \times 10^{-3}$	ΔE [MeV]	Photon resolution $P \times 10^{-3}$	Vertical image [mm]	Horizontal image [mm]
1	100	80	9	0.27	0.027	0.34	2.2	4.5
1	75	105	13	0.5	0.030	0.40	8.0	0.6
1	50	130	23	1.5	0.075	0.60	17.0	1.2
2	50	130	23	2.6	0.130	1.00	7.0	1.8
2	25	155	45	6.6	0.165	1.06	3.3	4.6
3	25	155	45	4.5	0.113	0.73	25.0	6.7
3	12.5	167.5	83	22.0	0.280	1.67	3.6	15.8

Table 2.1 Properties of the tagging spectrometer magnets with an incident beam energy of 180 MeV. Where E is the scattered electron energy, k is the photon energy and β is the angle between the incident and scattered electron.

where M_e is the rest energy of the electron, k and E being the photon and electron energies after the bremsstrahlung interaction. Calculations have shown [21],[23] that 95 % of the bremsstrahlung scattered electrons are found within this cone. If the ratio E_o/E_{max} is fixed at say 7.2 (the ratio for trajectory 3), then in order to obtain a *tagged* photon energy of 80 MeV, E_o would have to be reduced to 92.9 MeV, giving a value for ϕ of 133 mrad. However a value of 9 mrad is obtained when $E_o/E_{max} = 1.8$ (the ratio for trajectory 1) and $E_o = 180$ MeV are used. The resolution of the spectrometer is dominated by second order and higher order aberration coefficients, so that the resolution is proportional to ϕ^2 and higher order terms. Obviously, for low photon energies, fixing the ratio E_o/E_{max} would result in the spectrometer having poor resolution and a very low efficiency, since the angular spread of the bremsstrahlung electrons would be greater than the designed maximum acceptance angle of the spectrometer. A summary of the energy ranges possible using the *tagging* spectrometer are given in Table 2.2.

Trajectory	E_o/E_{max}	E_{max}	E_{min}	k_{min}	k_{max}
1	1.8	100.0	50.00	80.0	130.00
2	3.6	50.0	25.00	130.0	155.00
3	7.2	25.0	12.50	155.0	167.50
4	14.4	12.5	6.25	167.5	173.75

Table 2.2 *Tagging* spectrometer energy ranges for an incident electron energy of 180 MeV. (All energies in MeV)

Table 2.2 shows that the system can *tag* photons in the energy range 80 to 173.5 MeV for an incident beam energy of 180 MeV.

Having a variable main beam exit trajectory from DS1, makes beam handling more complicated than it would be for a spectrometer with a fixed E_o : E_{max}. For this reason the magnets DS3 and DS4 are incorporated in the system. They make it possible for the final main beam to exit from the system along a single trajectory irrespective of the settings in DS1 and DS2. This has enabled the spectrometer to be incorporated into the experimental system at Mainz, without any major alterations to the existing beam line.

Since the characteristics of the electron beam are minimally degraded when the beam leaves the spectrometer, as shown in Table 2.3, it is also possible to operate the spectrometer in a parasitic mode.

Trajectory	Vertical divergence (mm)	Vertical divergence (mrad)	Horizontal divergence (mm)	Horizontal divergence (mrad)
1	3.6	0.11	3.3	0.14
2	4.4	0.05	3.6	0.06
3	3.4	0.07	2.9	0.16
4	2.1	1.11	4.6	0.17

Table 2.3 Parameters of the electron beam after passing through the *tagging* system.

In this mode of operation the bremsstrahlung radiator is allowed to intercept only the outer fringes of the electron beam. The effective beam current incident on the radiator is of sufficient intensity to provide a reasonable *tagging* flux of photons. However, most of the main beam passes through the magnet system and exits from DS4 with the beam properties unimpared. Therefore the same beam can be used to run more than one experiment simultaneously.

Tests of the spectrometer were made using an α - particle source situated at the radiator position. This source was used to measure the resolution and dispersion of the spectrometer at two positions along the focal plane, corresponding to the central momentum trajectory and to the highest momentum trajectory analysed, as shown in Fig. 2.1. The source used was a 2 mm diameter 80 μ Ci open ^{242}Cm source, chosen due to its high specific activity. An unsealed source was used to ensure that energy broadening would not be significant and that the counting rate of several hundred counts per minute could be achieved within the geometric constraints of the tests. The ^{242}Cm isotope emits 2 α particles of energies 6.113 MeV (74 %) and 6.070 MeV (26 %) separated in momentum by 0.352 % and is ideal for enabling the spectrometer dispersion to be measured.

Circular collimators were employed to test measurements at half angles of 11 and 35 mrad, corresponding to the opening angles for 75 and 37.5 MeV electrons from an incident electron energy of 180 MeV. A collimated silicon surface barrier detector was used to count the α particles incident on the focal plane. Both the detector and the collimator were mounted so that they could be moved in the plane perpendicular to the incident α particle direction.

Source opening half-angle (mrad)	Electron Momentum Trajectory	Resoution %	Dispersion mm/ %	Vertical Image (fwhm) mm
11	Central	0.063	11.3	6.8
11	High	0.058	15.1	4.0
35	Central	0.072	11.6	—
35	High	0.102	15.0	4.4

Table 2.4 Results of α - particle test measurements on the *tagging* spectrometer.

The results of these tests and comparisons with the calculations from the beam transport code TURTLE[24] are shown in Figs. 2.5, 2.6, 2.7 and Table 2.4. The TURTLE computer code uses Monte Carlo techniques to trace the paths of a random sample of particles through a magnet system. Table 2.4 shows the data with the effect of the finite slit widths unfolded from the measured peak shapes. Figs. 2.5 and 2.6 show the results of scanning the focal plane horizontally with the slit width at 0.5 mm. The peaks are well resolved for both opening angles at both the central and high momentum trajectories. A comparsion with the TURTLE calculation shows the measured peak position to be in agreement with the computer prediction. Fig. 2.7 shows the result of a vertical scan, with a slit of dimensions 1.2 mm vertical and 4mm horizontal. Again there is satisfactory agreement with the calculations. A detailed account of the spectrometer and beam handling magnets is presented by Kellie[21].

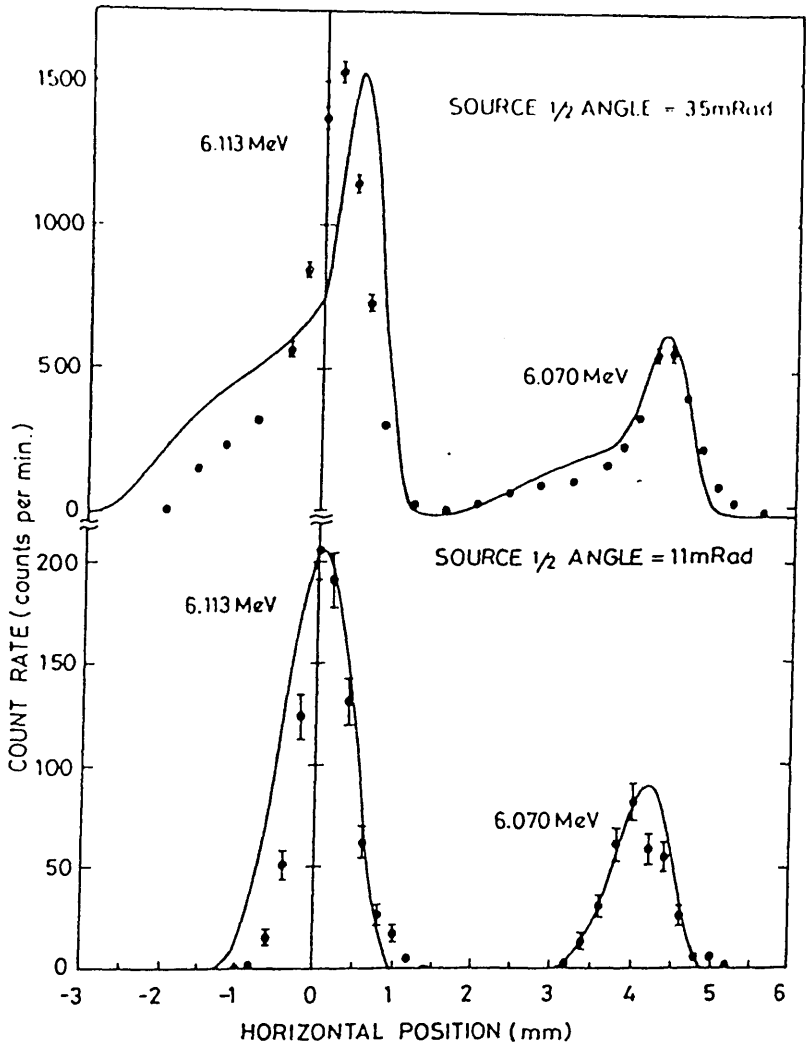

Figure 2.5 Horizontal distributions of α-particles from a ^{242}Cm source at the object position measured at the central momentum position in the focal plane of the *tagging* spectrometer. The lines are the results of calculations using the code TURTLE[24].

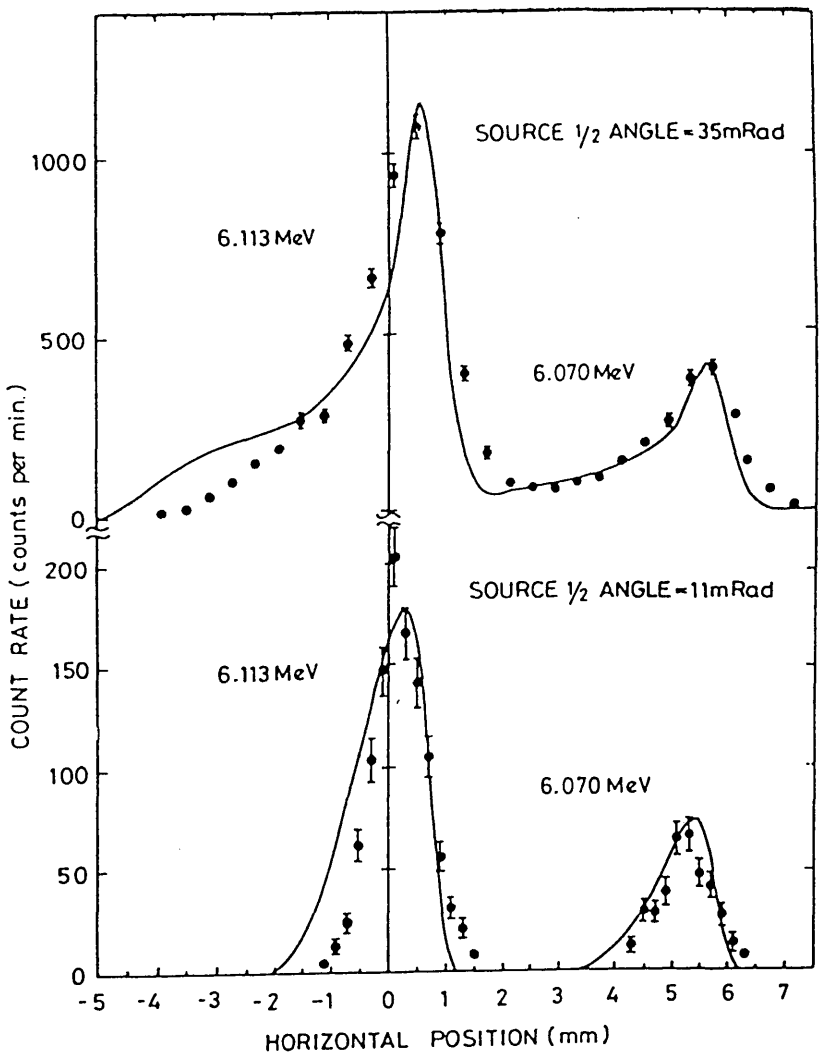

Figure 2.6 Horizontal distributions of α -particles from a ^{242}Cm source at the object position measured at the high momentum position in the focal plane of the *tagging* spectrometer. The lines are the results of calculations using the code TURTLE[24].

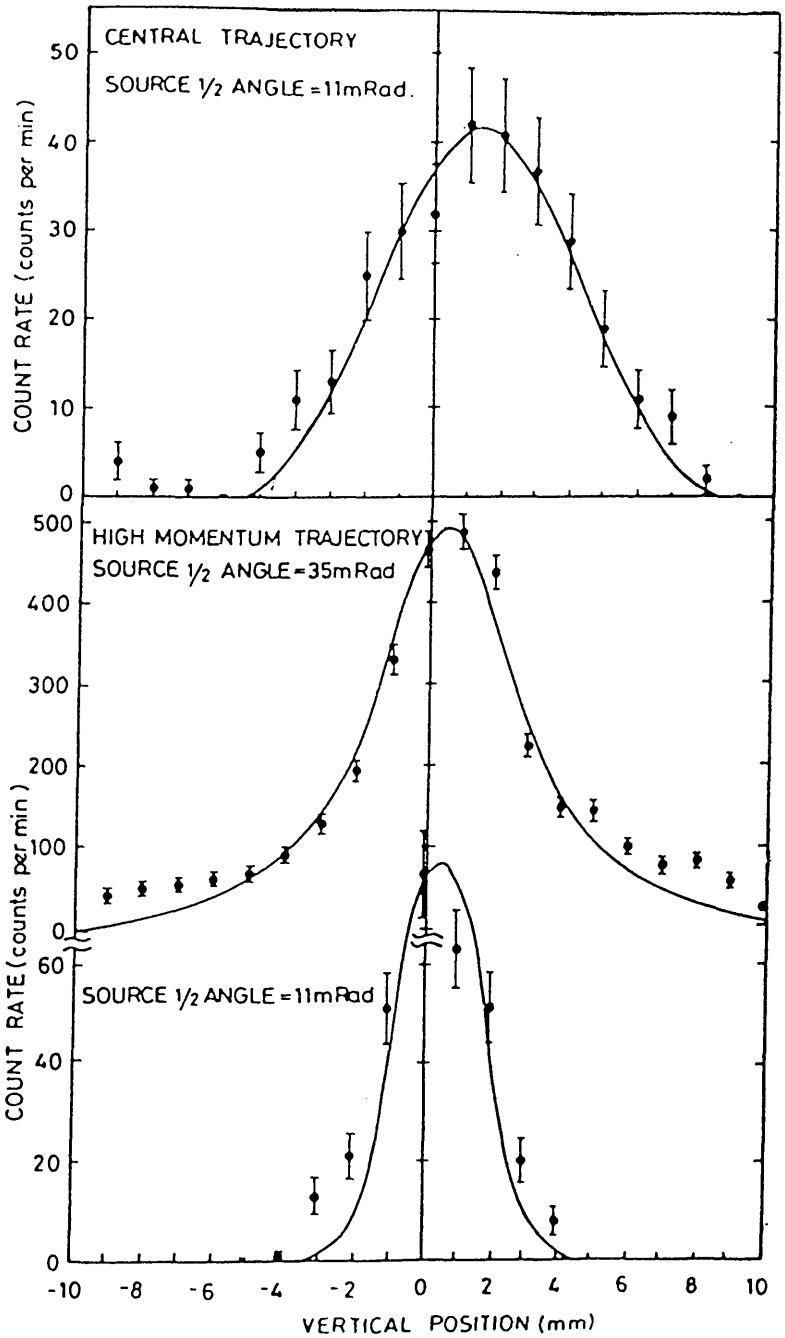

Figure 2.7 Vertical distributions of α-particles from a ^{242}Cm source at the object position measured at the central momentum position in the focal plane of the *tagging* spectrometer. The lines are the results of calculations using the code TURTLE[24].

2.4 The Focal Plane Detector

2.4.1 Introduction

The focal plane detector of the *tagging* system is of prime importance. It is this detector which is the *tagging* detector and is used to measure the magnitude of the *tagged* photon flux, and determine the energies of individual photons. The design and development of a fast electron detector, for the focal plane of the *tagging* spectrometer, was based on the following performance specifications;

- Fast Timing: A resolution of 1.5 nS or better to minimise random coincidences with the particle detectors.
- Good Energy Resolution : An uncertainty of less than 1 MeV in the *tagged* photon energy.
- High Count Rate Capability : A rate of 100 MHz summed over the focal plane was indicated, to produce a large *tagged* photon flux.
- Good Background Rejection : Since the focal plane detector must be operated within 1 m of the main beam line and the photon beam collimators.
- High Efficiency: When detecting high energy electrons.

Situated on the curved 1.3 m long focal plane of the QDD spectrometer, the detector consists of 92 scintillators and accompanying photomultipliers. Scattered electrons from the bremsstrahlung interaction, do not meet the curve of the focal plane normally, but at an angle dependent on the distance along the focal plane. The variation of incident electron angle along the focal plane is shown in Fig. 2.8. However scintillators are positioned in such a way, that they are half overlapping with respect to the incoming bremsstrahlung scattered electrons, so that each incident electron will pass through two adjacent scintillators, as shown in Fig. 2.9. The detector also contains its own purpose built electronics system, which digitises the timing and energy information and presents it in a form acceptable to the data collection system. There are three types of output provided, 92 single scintillator outputs, 91 overlap or coincidence channel outputs and 12 OR outputs, one for each group of 8 coincidence channels. The single scintillator outputs are used to facilitate the optimisation of the detector.

2.4.2 Detector and Mechanical Details

The focal plane detector, stands in air just outside the 150 μm aluminium exit window of the spectrometer vacuum box. Scintillator segments of dimensions $2\times17\times60$ mm are optically coupled to 18 mm diameter photomultipliers by means of a twisted segment perspex light guide. Shown in Fig. 2.10, is a schematic representation of the construction and orientation of the light guide and scintillator elements. The optical and mechanical bond between the two sections is made

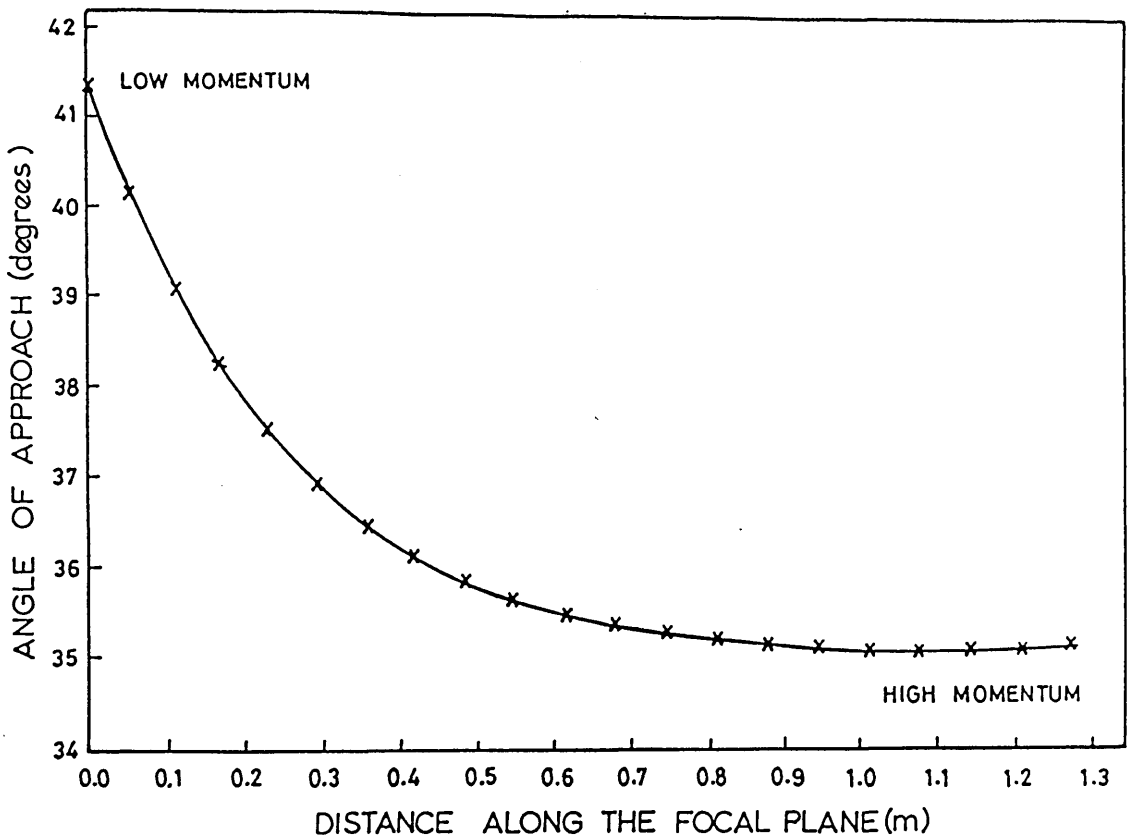

Figure 2.8 Electron trajectory angles relative to the focal plane.

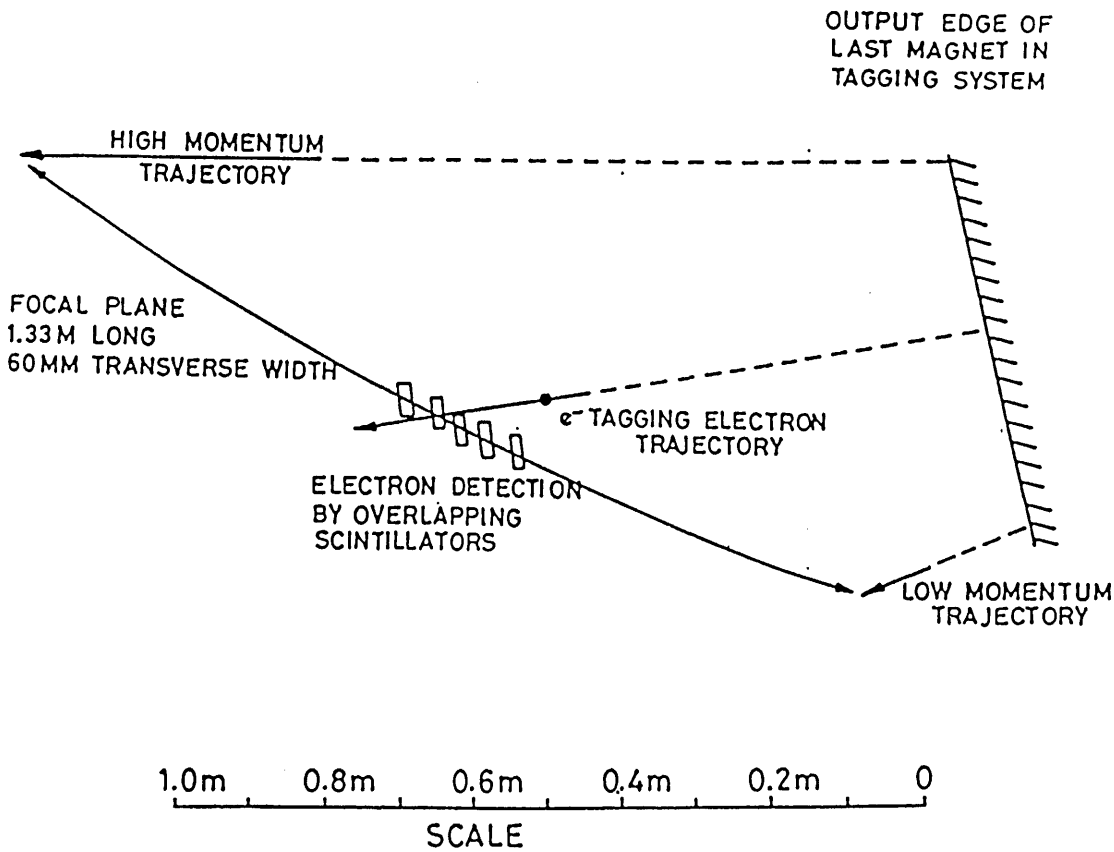

Figure 2.9 Spectrometer focal plane geometry, showing the central, low and high momentum trajectories.

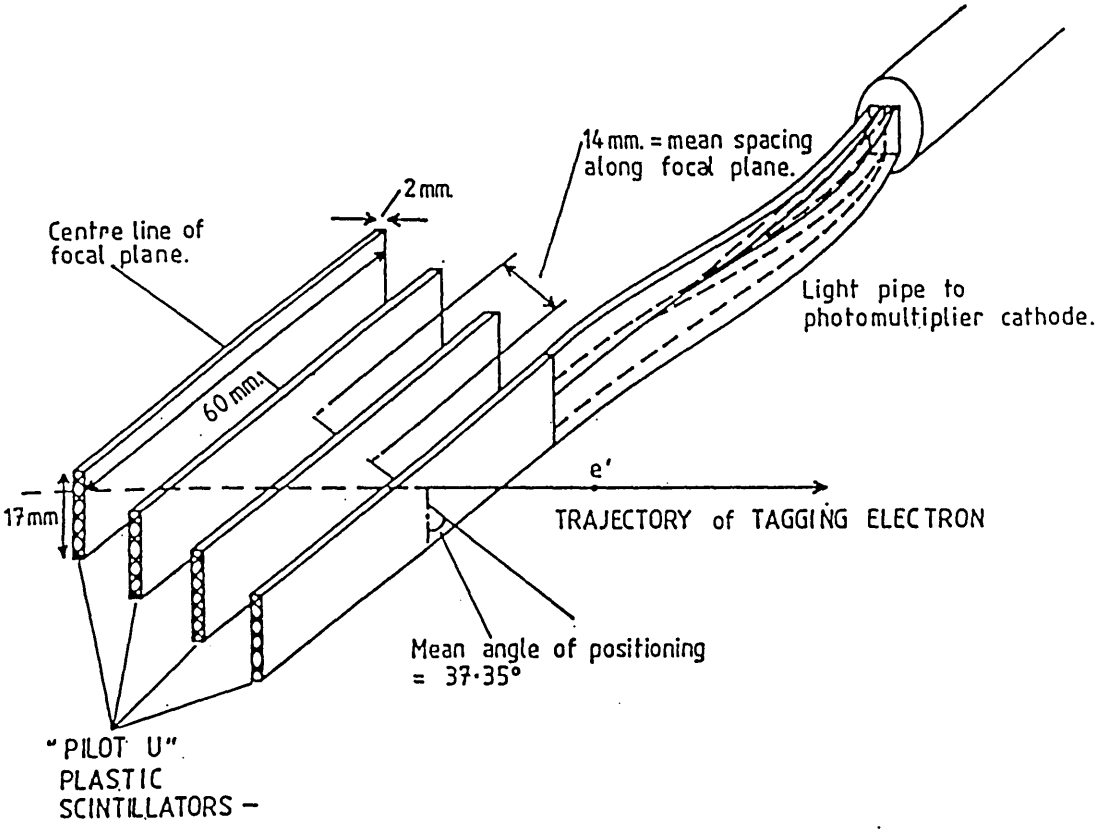

Figure 2.10 Construction and orientation of the scintillator elements.

using an optical glue NE581. The light guide consists of two perspex strips, twisted to ensure they overlap at one end, so that the light collected is directed to the most active part of the photocathode. A diagram of the light guide and scintillator assembly is shown in Fig. 2.11. As a further aid to light collection the unglued end of the scintillator is painted with NE560 reflector paint. Light proofing of the light guide and scintillator assembly, is achieved by inserting the assembly into a Mylar sleeve, which also serves to aid specular light collection. In addition to this, the assembly is placed in a black plastic envelope.

A clear rubber silicone compound, SILASTIC 734 RTV is used to make the light guide to photomultiplier optical contact. This gives much the same optical contact as a silicone grease, but has the advantage that it can be easily removed when needed. Since the SILASTIC rubber compound provides a weak mechanical bond, it does not exhibit the creepage problems associated with silicone grease.

To hold the scintillators and photomultipliers in their given positions on the focal plane, a metal support was constructed. This consists of four levels, shown in Fig. 2.12. Each scintillator and photomultiplier assembly is supported by two retaining springs, with the fine adjustment of the scintillator position made by a stopping screw. The attitude of the scintillators to the incident electrons is defined by a series of slots, shown in Fig. 2.13(a) as level 2, the retaining piece ensuring that the scintillators are centred correctly in the slots. The photomultipliers are similarly located by a series of aligned apertures in the two lower levels, shown as levels 3 and 4 in Fig. 2.13(b).

The location of the focal plane detector in the experimental area, is fixed by using two plates embedded in the concrete floor. Metal pins were secured

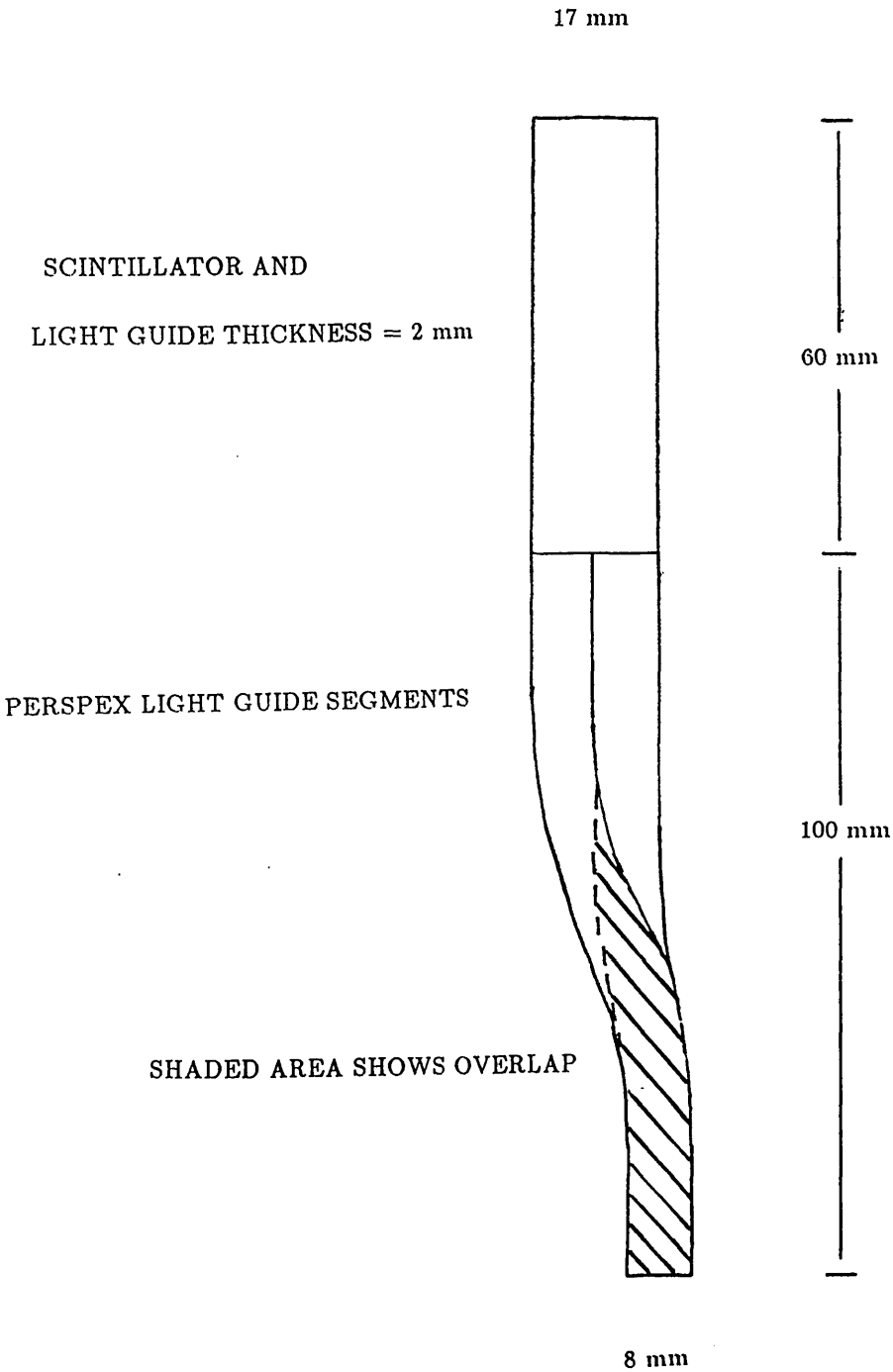

Figure 2.11 Scintillator / light guide assembly.

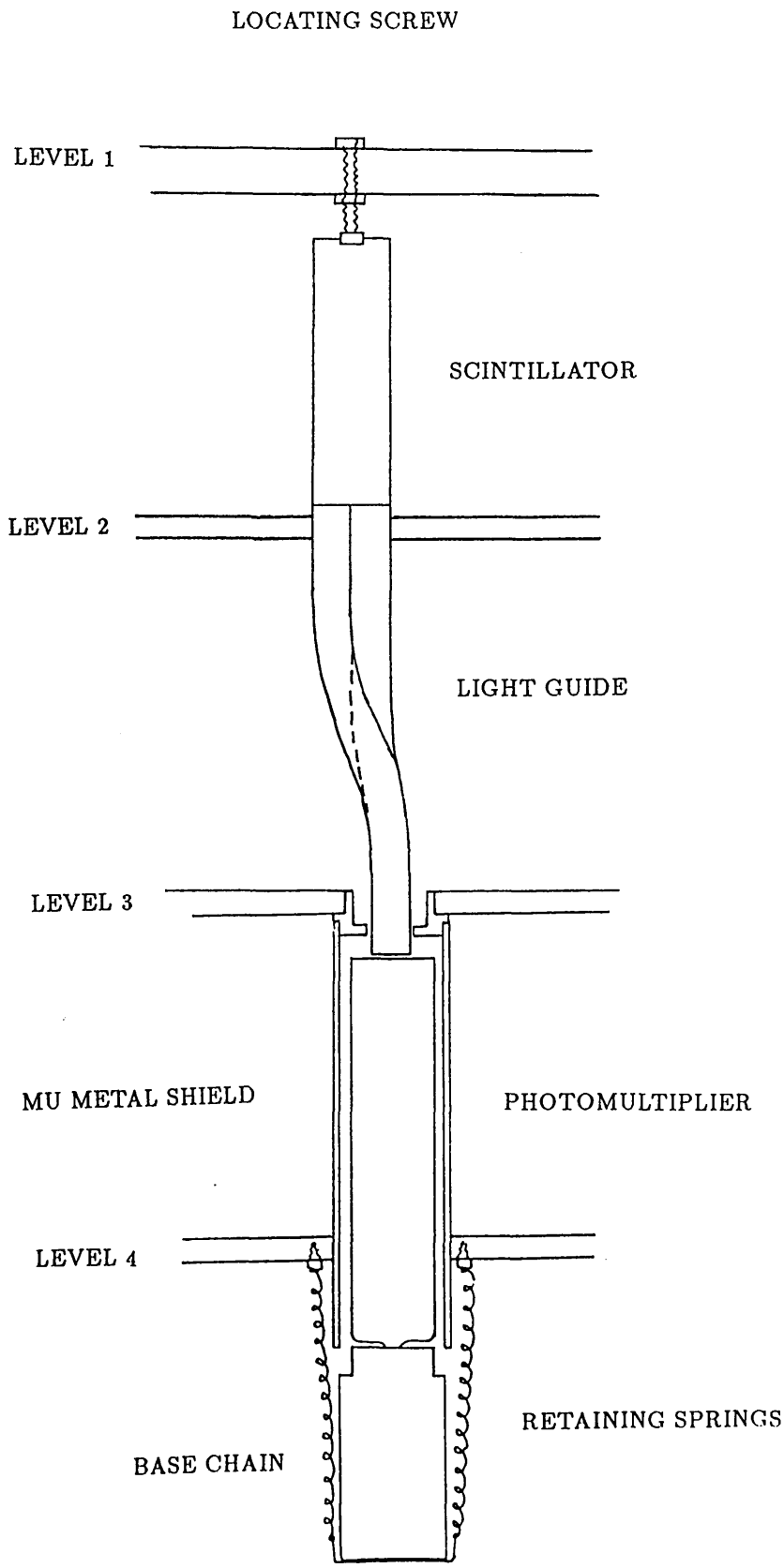

Figure 2.12 Schematic diagram showing the four levels of the photomultiplier - scintillator support.

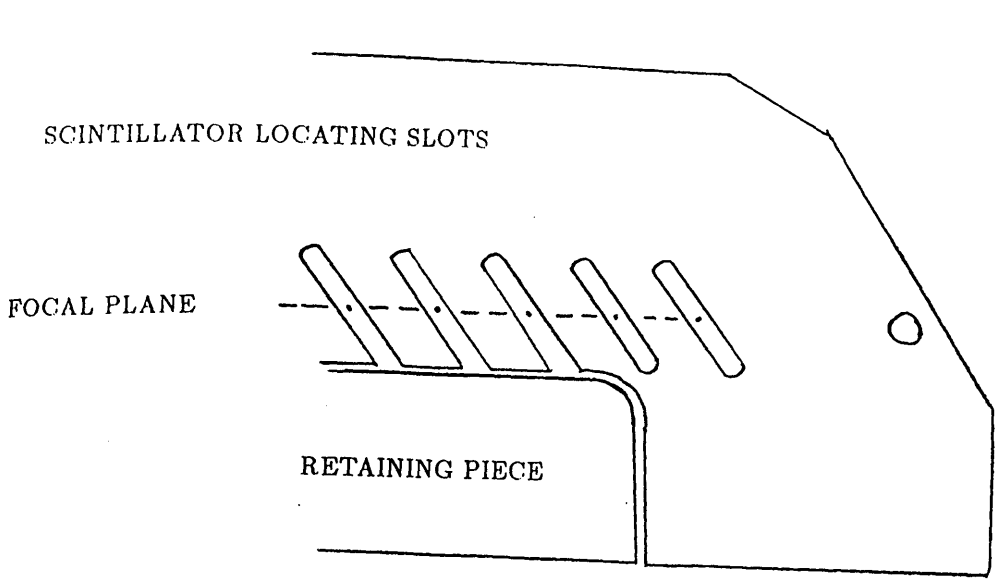

Figure 2.13 (a) A section of the scintillator locating slots and retaining piece.

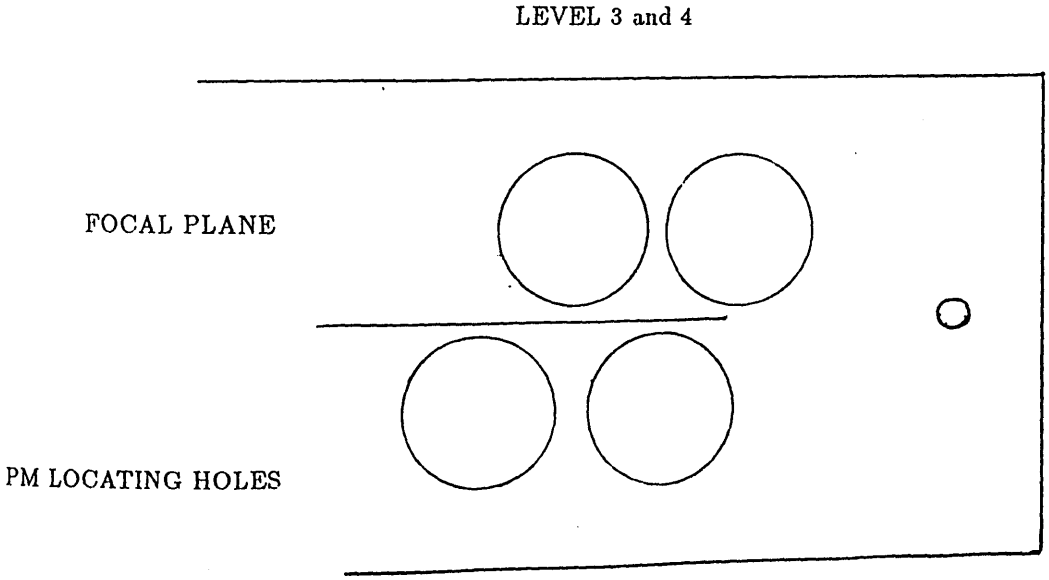

Figure 2.13 (b) A section of the photomultiplier locating apertures.

to the stand of the detector, which when inserted in the locating holes of the floor plates, position the detector to within 1 mm of its designed placement. The plates themselves were positioned using the location of the spectrometer magnets as reference points.

2.4.3 Background Considerations

As shown in Fig. 2.1, the focal plane is in close proximity to both the main beam line, the photon beam collimators and the spectrometer magnets. In addition to background arising from these sources, there is background emanating from bremsstrahlung scattered electrons which are not incident on the focal plane of the spectrometer. Most of these scattered electrons impinge on the vacuum box, between the beam exit window and the yoke of DS2, producing an electron and gamma shower. To suppress the background produced from these sources, an output can only be produced if two adjacent scintillators are activated within a short period of time, i.e. a coincidence is produced. During the optimisation of the focal plane array the coincidence resolving time for each channel was set at 10 nS.

The angular acceptances of the array channels are dependent upon the size and spacing of the scintillators, and are set predominately in the direction of the directly produced bremsstrahlung electrons. As a result of these measures, measurements of random coincidences with the particle detectors are found to be negligible at a focal plane detector rate of $10^6 s^{-1}$. Furthermore, when in

operation in the absence of the bremsstrahlung radiator the counting rate from the entire focal plane is found to be 1 per second.

2.4.4 Energy Resolution

Energy information on the scattered electrons incident on the focal plane, is given by the position on the focal plane of the scintillators activated, since the variation of electron momentum along the focal plane is known. Calculations show that the variation of the electron momentum along the focal plane is not linear. Also from Fig. 2.8, we see that the angle of approach of the electrons to the focal plane varies along its length. To be able to achieve an energy resolution of $\approx$ 1 % with equal momentum bites for each section of the detector, yet still retain some form of coincidence channel output to reduce background, would have entailed the manufacture of individually shaped scintillators. This would have been prohibitive in cost, design and manufacturing time. There would also have been a danger of introducing a variation in channel response. Consequently, a second option was chosen, which used equal channel size. This however resulted in the momentum bite varying from channel to channel.

Equality of channel size can be achieved by two means. The spacing of the scintillators could be kept constant and the angle of the scintillators to the focal plane varied, so that each scintillator presents a perpendicular target to the incident electrons. Alternatively, the scintillators can be kept at a constant angle to the focal plane and the spacing of the scintillators can vary. This means the

incident electrons are only approximately perpendicular to the scintillators.

The focal plane scintillators are necessarily closely packed making it impossible to locate the photomultipliers directly on to the scintillators, and consequently for either method the optical connection between scintillator and photomultiplier can only be accomplished by the use of light guides. The equal channel size with varying momentum bite was selected to allow the shape of the light guides to be standardised.

To present the scintillators approximately perpendicularly to the incoming electrons, a median angle of approach of 37.5° for the bremsstrahlung electrons was chosen. With this choice of median angle any electron will meet the focal plane scintillators at an angle of 90 ± 4°. The spacing of the scintillators along the focal plane, as can be seen from Fig. 2.14, is given by,

$$spacing = \frac{\Delta X}{\sin \theta_i} \tag{2.2}$$

where ΔX is the coincidence channel size and θ_i is the angle of approach. The scintillator width was set at 17 mm, so the size of a half overlap channel was 8.5 mm. However, inaccuracies in the positioning of the scintillators were estimated to be as much as 0.5 mm. This produces *holes* in the focal plane; i.e. places where no overlap exists and which therefore do not produce a coincidence output. To minimise this the coincidence channel size was set at 8.25 mm. Although this increases the probability of an electron passing through 3 adjacent scintillators and giving two coincidence outputs, such events are easily recognisable during

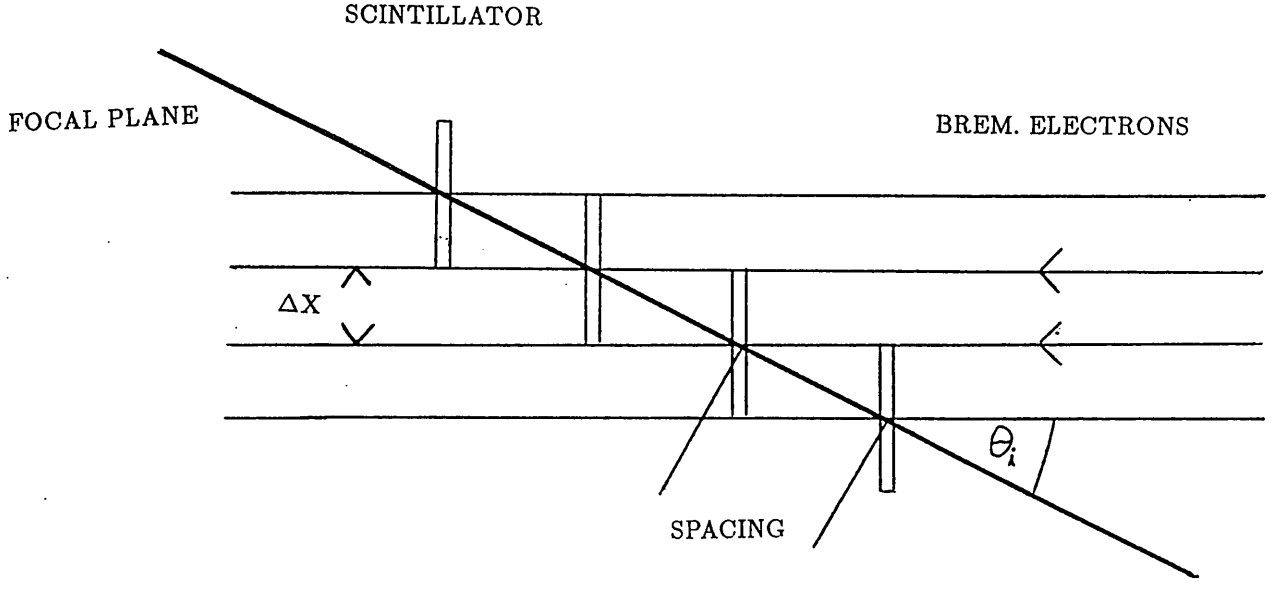

Figure 2.14 Relative positioning of the scintillators along the focal plane.

the analysis of the data and can be counted as real events rather than background events.

The resultant variations in the momentum bite, examined by each of the coincidence channels, is shown in Fig. 2.15. This figure shows that the variations encountered are minimal and that for most purposes the variation can be neglected.

2.4.5 Timing and Detector Electronics

In the design of the detector and the accompanying electronics, speed of response was an important consideration, both to reduce random coincidences with the particle detectors and to give precison timing for the time-of-flight measurements of the particle detectors. The uncertainty in the time of arrival of the electrons at the focal plane introduced by the spectrometer is 0.5 nS. This is caused by electrons of the same energy taking slightly different paths to the same point on the focal plane. To achieve less than 1.5 nS resolution, fast scintillators, photomultipliers and electronics were required.

Although not as fast as some liquid scintillators, Nuclear Enterprise's PILOT U plastic scintillator has a rise time of 0.5 nS combined with a large light output. Unlike liquid scintillators however, it has the advantage of being easily produced in any shape, such as the thin slabs needed for the focal plane detector. The photomultpliers used were small 18 mm diameter tubes. Hakuto's R1450's were selected, as they provide both good gain and have a 1.8 nS rise time. To reduce

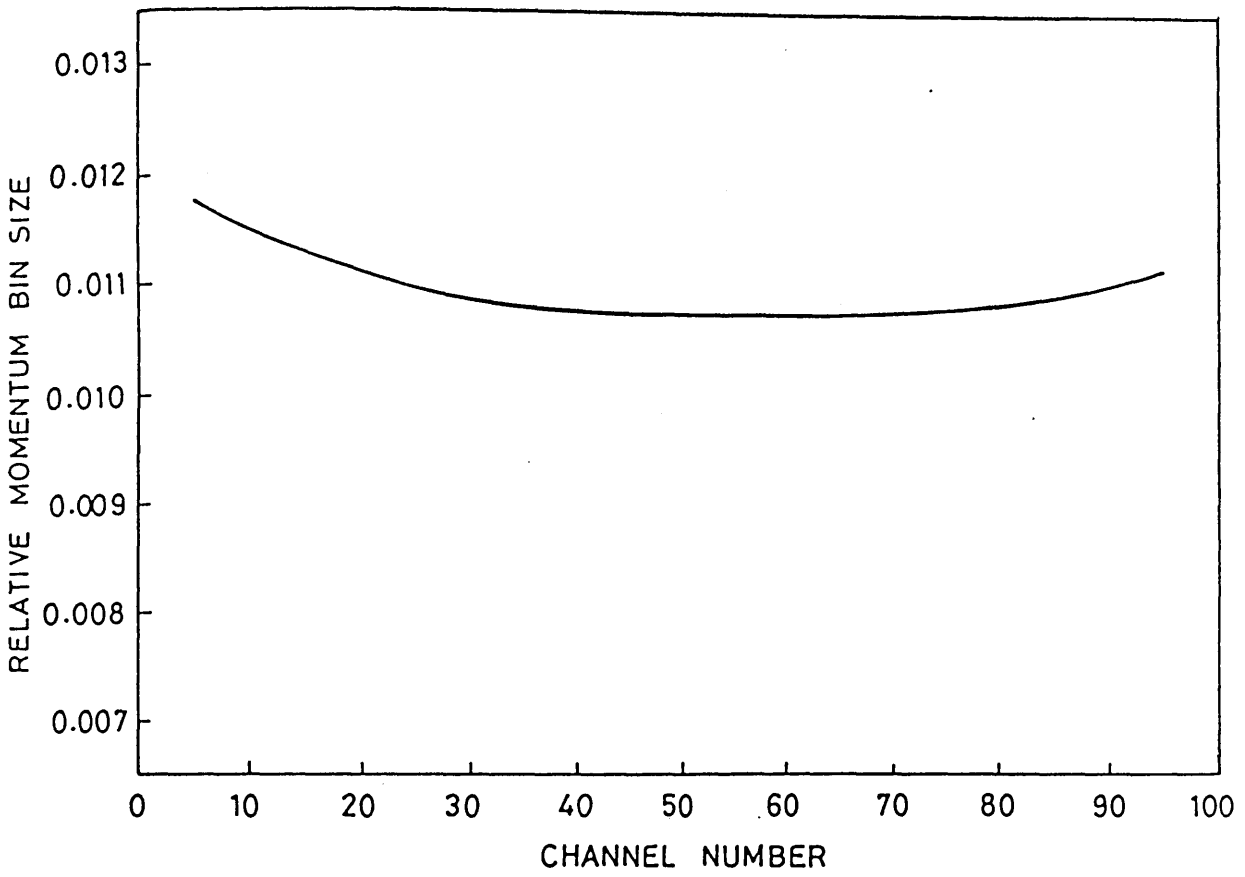

Figure 2.15 Ratio of the momentum bite of each coincidence channel to the total momentum bite of the focal plane against the channel number along the focal plane.

any channel to channel variations in time resolution, the photomultiplier anode pulses were standardised to give 100 mV peak amplitude in a 50 Ω load.

This was achieved by measuring the response of each scintillator to electrons from a ^{90}Sr source, and varying the supply voltage of the scintillator photomultiplier until a mean 100 mV output pulse was produced. The supply voltage was then noted and set. A typical spectrum produced using the ^{90}Sr source in a single channel is shown in Fig. 2.16. The response of the focal plane array after it has been set up using this procedure is shown in Fig. 2.17. By operating the photomultipliers at these predetermined voltages, differences in the photomultipliers gains and variations in channel light collection are minimised. To provide this facility the array has ten power lines of varying voltage; this allows each photomultiplier to be within 25 V of its optimum (100 mV anode output) supply voltage setting.

To reduce the dispersive effects of the connecting cabling on the rise time of the anode pulses, the electronics are mounted directly below the photomultipliers. With this arrangement, the anode pulse has a rise time of $\approx$ 4 nS when it reaches the electronics. Emitter coupled logic (ECL) circuitry, which can cope with the high count rates expected, while not significantly degrading the time resolution, is used.

The detector electronics are comprised of 6 ECL printed circuit boards, each board dealing with a group of 16 scintillators from the focal plane array. A circuit diagram for one coincidence channel, is shown in Fig. 2.18. This diagram also indicates the number of repeats of each section per board. Each photomultiplier anode pulse is fed to a fast leading edge discriminator, each discriminator having

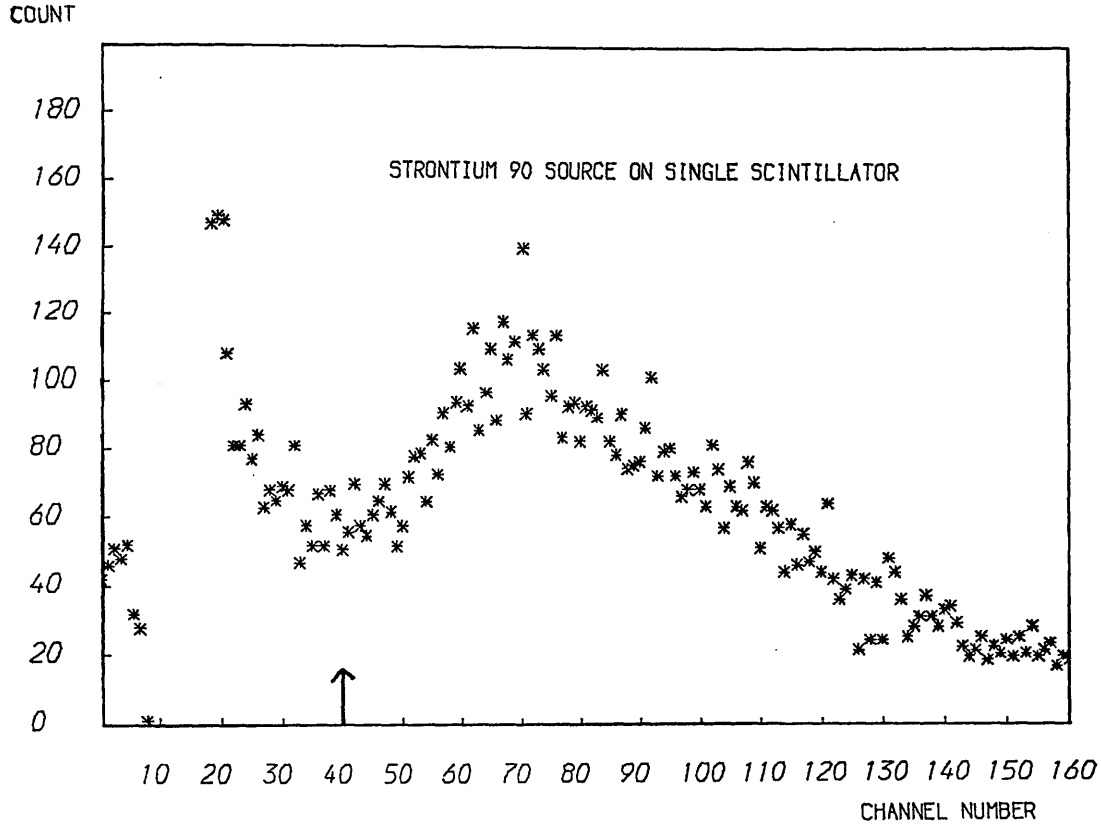

Figure 2.16 A typical spectrum, using the ^{90}Sr test source, from a single scintillator / photomultiplier channel, and showing the discriminator level (indicated by an arrow) to be set, in the valley between the thermal noise and the detected electrons.

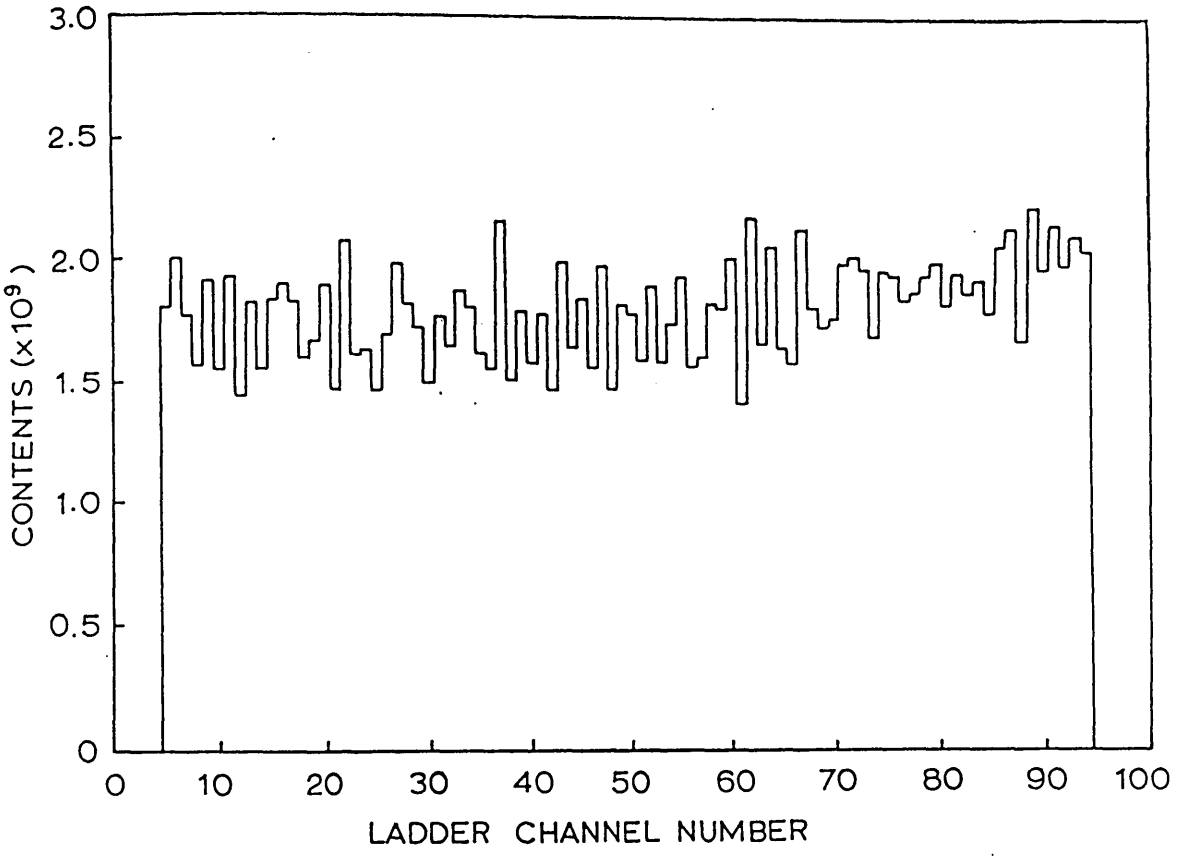

Figure 2.17 Count rate per coincidence channel measured with a ^{90}Sr β test source moving at a constant rate along the focal plane.

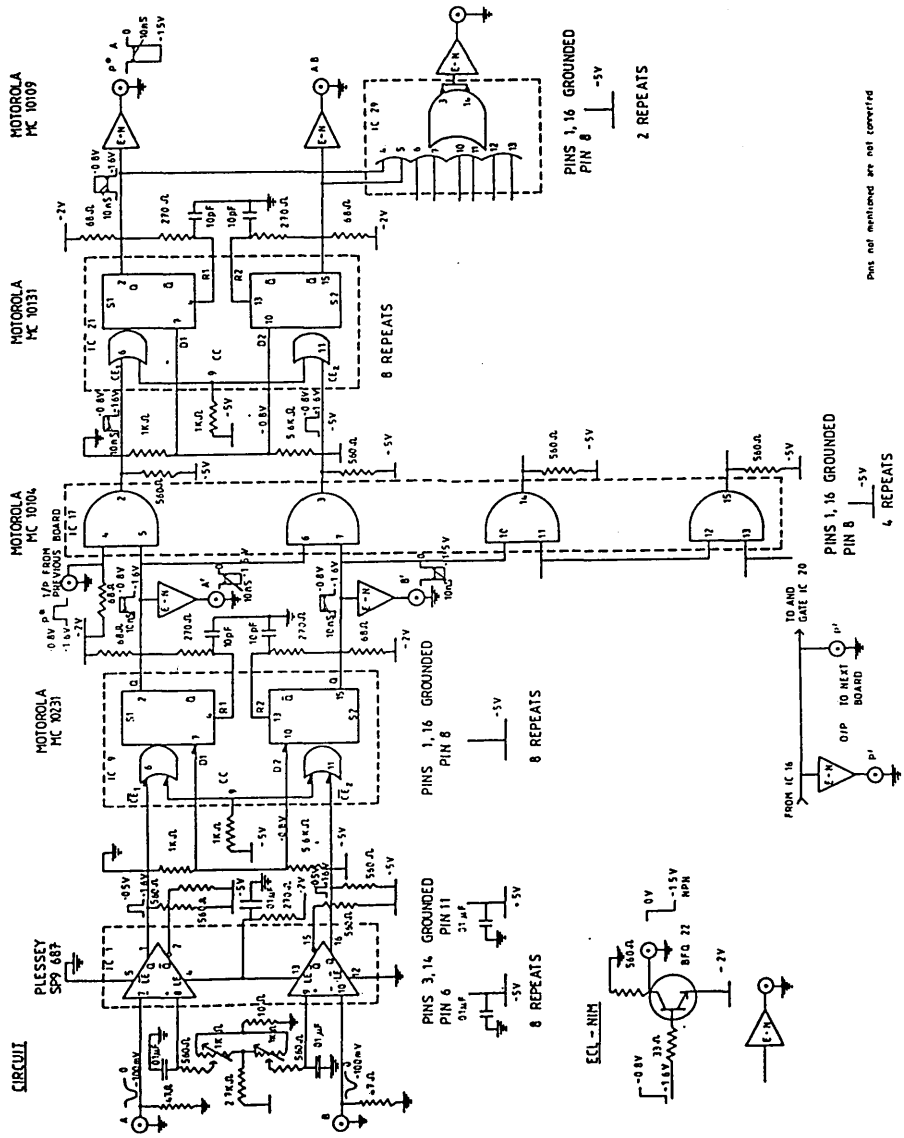

Figure 2.18 Circuit diagram of one channel of the focal plane, showing the number of repeats per board.

its own threshold control. The timing diagram for one scintillator channel is shown in Fig. 2.19. To minimise variations in time resolution from channel to channel, all thresholds were set to 30 mV, a value just above the photomultiplier dark current, as shown in Fig. 2.16. By adopting this approach to the design of the electronics each channel presents a standard shape of pulse to a timing discriminator which has a common threshold. The discriminator outputs are pulse shaped by a bistable, to produce a 10 nS ECL standard signal. Adjacent pairs of pulse shaped discriminator outputs are connected to AND gates, to provide a coincidence signal. Each bistable signal is also used to produce the single scintillator output, which is used extensively in setting up the detector.

The AND gate signals are again pulse shaped by a bistable before producing the coincidence outputs. Groups of 8 coincidence channel signals are fed to an OR gate, the output of which gives in effect the count rate of that section of the scintillator array. Although the anode pulses are processed using ECL circuitry, all the outputs are converted to double NIM standard pulses, to ensure compatibility with the external data collection system. The ECL to NIM converters are located on the printed circuit board, and the circuit diagram for the converters is shown in Fig. 2.18.

The resultant time resolution is found to vary from channel to channel, despite the measures taken. However, most have a resolution between 0.9 and 1.2 nS which is well within the design requirement. The time resolution distribution is shown in Fig. 2.20.

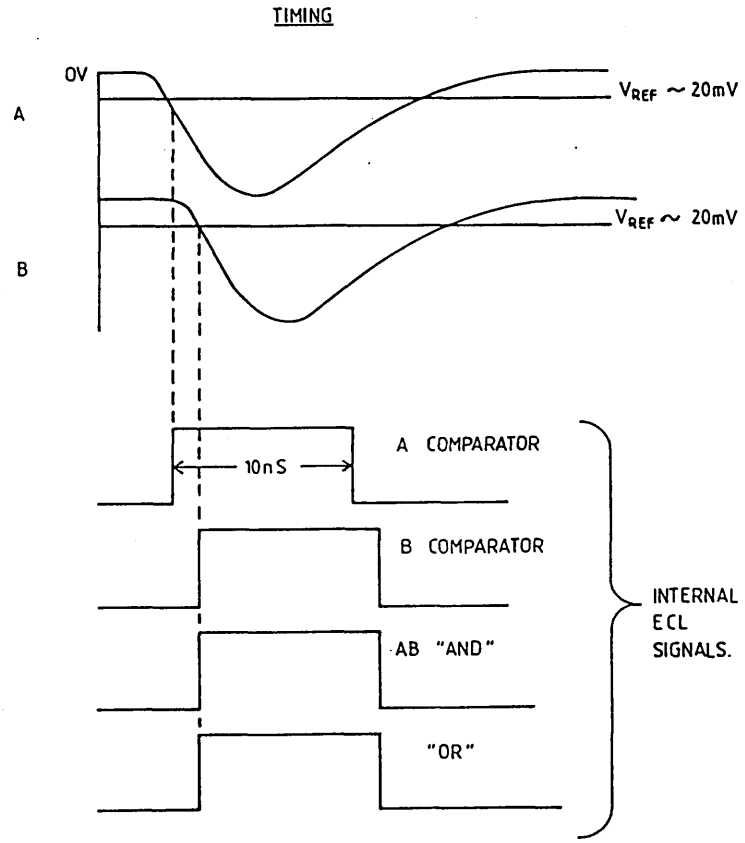

Figure 2.19 Timing diagram of one channel of the focal plane detector.

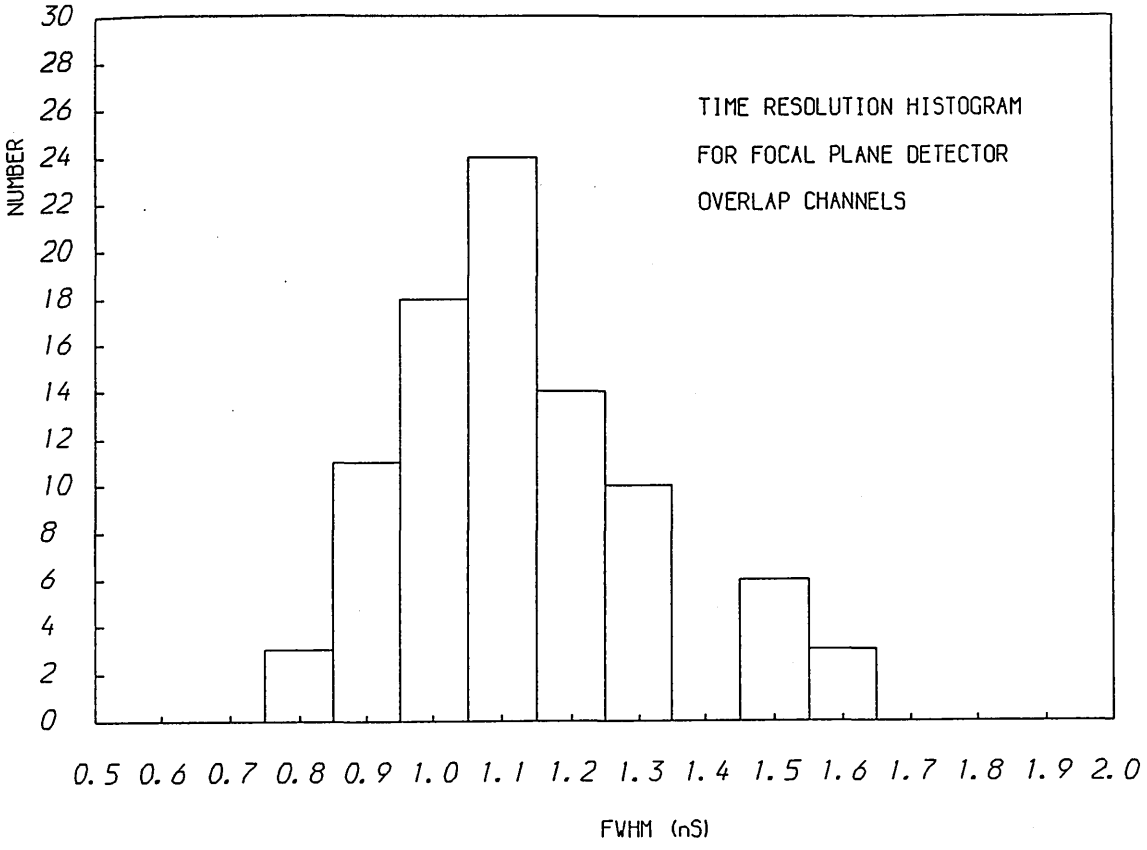

Figure 2.20 Time resolution distribution for the focal plane detector coincidence channels.

2.4.6 Rate Effects

A design requirement of a rate of 10^8 detected electrons per second was quoted. For this rate it is found that each each of the photomultipliers in the focal plane detector, has a counting rate of around 1 MHz. However, with anode pulses in the region of 100 mV into 50 Ω, and of 20 nS in duration, the normal carbon resistor base chains were observed to lose gain significantly at 0.5 MHz, as is shown by the solid line in Fig. 2.21. To allow the photomultipliers to function at a higher mean current, a new base chain was designed, with zener diodes across the last three dynode sections. The last dynodes effectively control the gain of the photomultplier. This gives a steady voltage drop of 100 V across each of the last three dynode sections, while allowing enough current to produce the required output pulses at up to 10 MHz without affecting the gain of the photomultplier, as is shown by the dot dash line in Fig. 2.21.

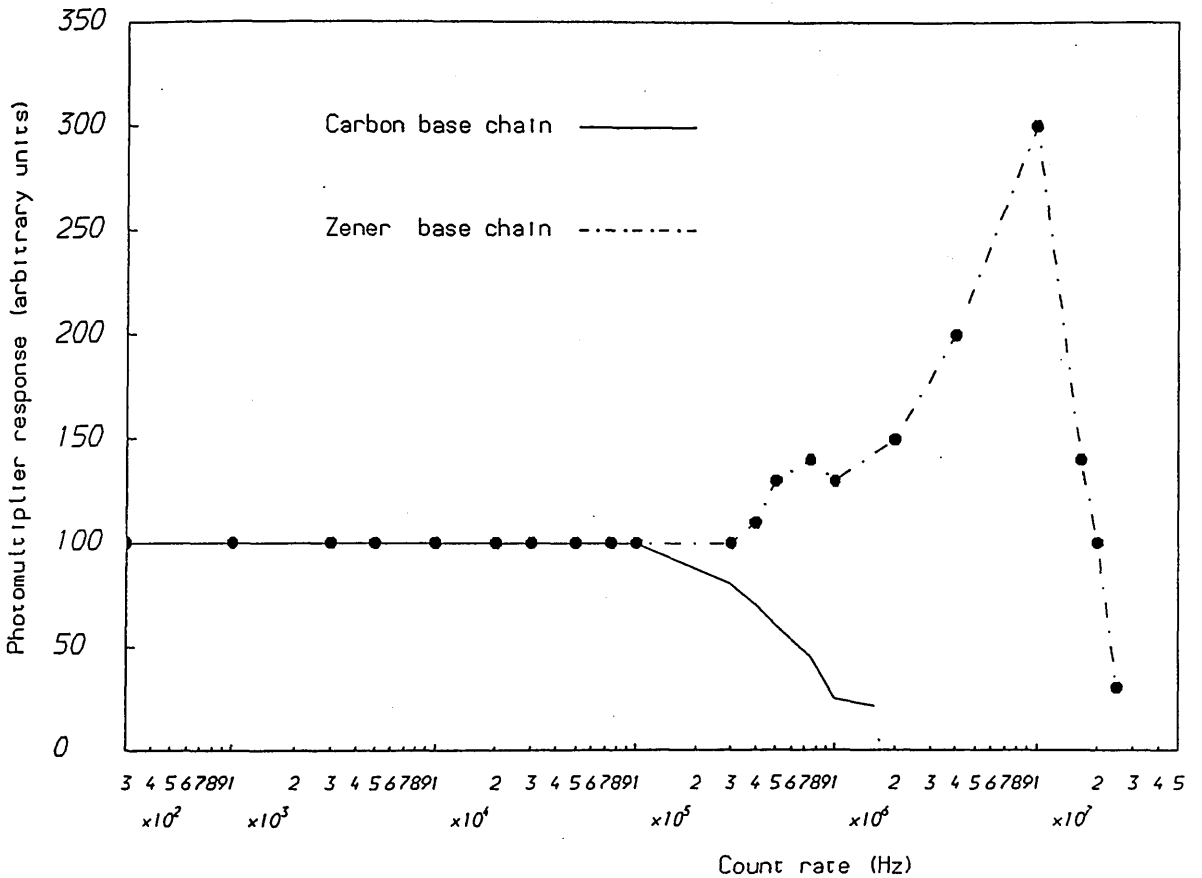

Figure 2.21 A plot showing the variation in response between a carbon resistor only photomultiplier base chain and a carbon resistor and zener diode base chain.

2.4.7 Performance

The important performance features of the focal plane detector ladder may be summarised as follows;

- Energy resolution of 1.1 % of the energy range employed.
- Time resolution of $\approx$ 1 nS.
- Count rates of 1 MHz per single scintillator channel can be accommodated i.e.$10^8 s^{-1}$ across the focal plane.
- Background, electronic noise produces 10 coincidences per minute. However when in coincidence with the particle detectors, this and other beam related noise are found to be of minimal importance at focal plane detector rates of $10^6 s^{-1}$.

Clearly these performance characteristics compare favourably with the design requirements.

2.5 The Photon Beam

The photon beam is produced by a thin bremsstrahlung radiator in the electron beam, at a point some 0.2 m upstream from the first spectrometer magnet, QS1. To allow the system to run with radiaitors made of varying materials, and varying thicknesses, the beamline contains a bremsstrahlung radiator target changer[25]. The radiator changer consists of a large wheel, containing 16 circular ports on its perimeter, into which targets may be placed. Eight of the 16 ports are used for bremsstrahlung radiators, the rest containing phosphor screens used to check the alignment of the electron beam on the radiator. The bremsstrahlung target wheel is driven by a stepping motor, and incorporates a reduction gearbox to allow 8000 different wheel positions. Backlash is eliminated in the system by ensuring that the wheel always rotates in the same direction.

The characteristics of the photon beam, are determined by the radiator material used and the thickness of the target. Fig. 2.22 shows the calculated variations in the photon angular distribution found from two aluminium radiators of thickness 25 μ m and 250 μ m. It is clear that the thickness of the radiator will influence the *tagging* efficiency of the system when the beam is collimated. The photonuclear target is positioned 4 m from the radiator with the beam diameter and profile being determined by a collimator positioned just outside the vacuum chamber of the dipole magnet DS3. The collimator is shown in Fig. 2.23. The first part is made of solid Hevimet and contains a central aperture. The opening angle of the aperture being equal to two bremsstrahlung characteristic angles. This provides a *tagging* efficiency of approximately 65 % from a 25 μ m alumini-

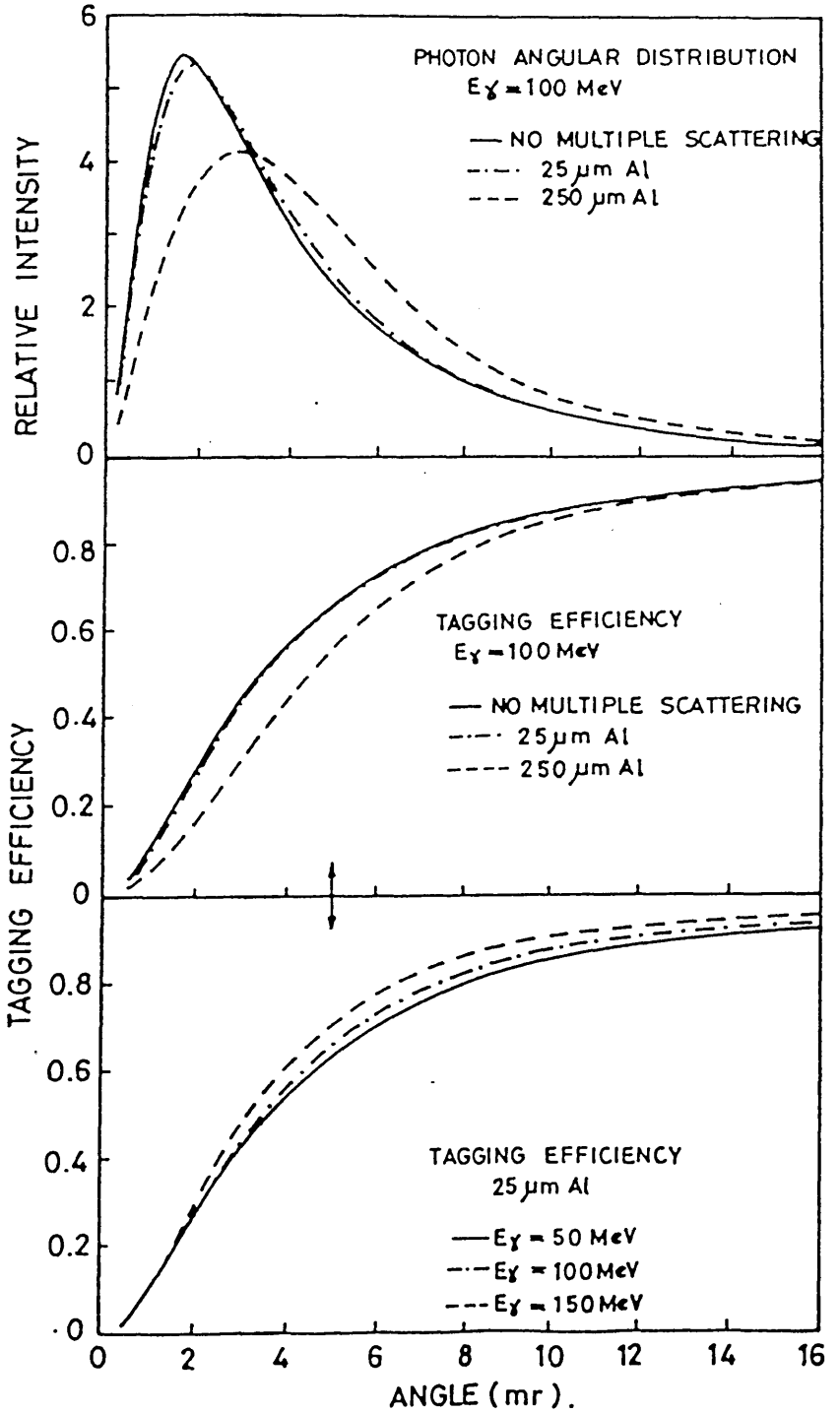

Figure 2.22 Photon angular distribution and *tagging* efficiency calculations[26]. The arrow shown indicates the opening angle of the collimation system.

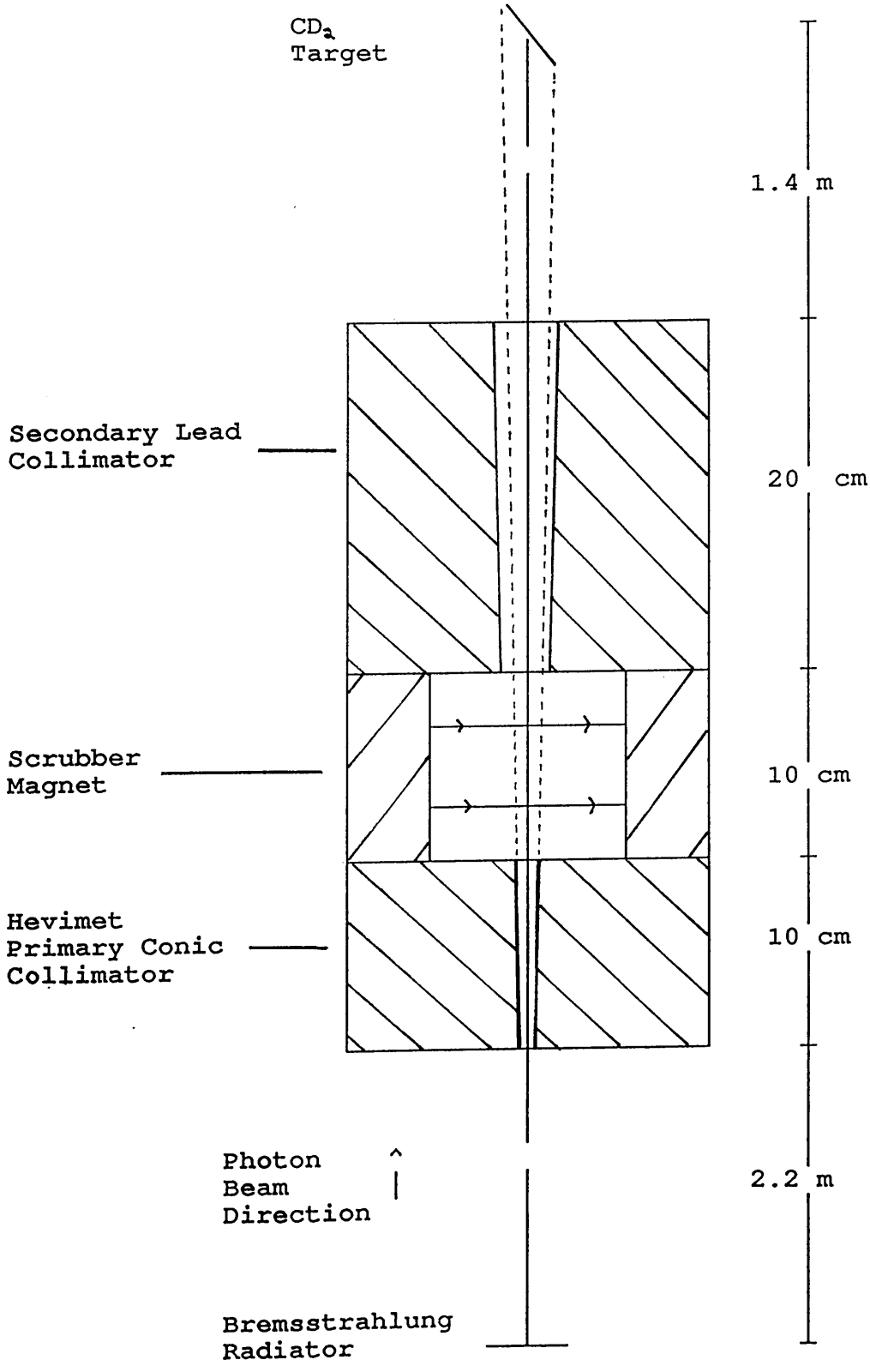

Figure 2.23 Photon Collimator System.

um radiator.

After emerging from this collimator the beam is contaminated with electrons from the primary collimator. To remove the electrons a *scrubber* magnet is employed, which effectively removes all but the highest energy electrons from the photon beam line. Finally, a second collimator, which is just bigger than the collimated beam, is found after the *scrubber* magnet. This is made of lead and is used to eliminate stray electrons scattered by the preceding magnet and does not collimate the photon beam. Using this collimation system a beam spot of 4 cm in diameter is produced at a photonuclear target situated 4 m from the bremsstrahlung radiator.

Chapter 3

The Present Experimental Technique

3.1 Introduction

This chapter describes the experimental set-up and the techniques used to measure the differential cross section for the photodisintegration of the deuteron using the *tagged* photon spectrometer described in the previous chapter. Quasi-monoenergetic photons from the *tagged* photon spectrometer, are incident on a deuterated polyethlyene target, which is set at an angle of 30° to the photon beam. Protons from reactions in the target are subsequently detected by a segmented scintillator detector. The arrangement of the detector is shown in Fig. 3.1. Due to the simplicity of the kinematics of the deuteron, detection of the photoproton is sufficient to define the reaction. Information on the protons incident on the proton detector, in the form of ADC and TDC signals from the output photomultipliers, is collected using a HP1000 controlled CAMAC system. The data is stored on magnetic tape for later analysis, and also provides useful online information.

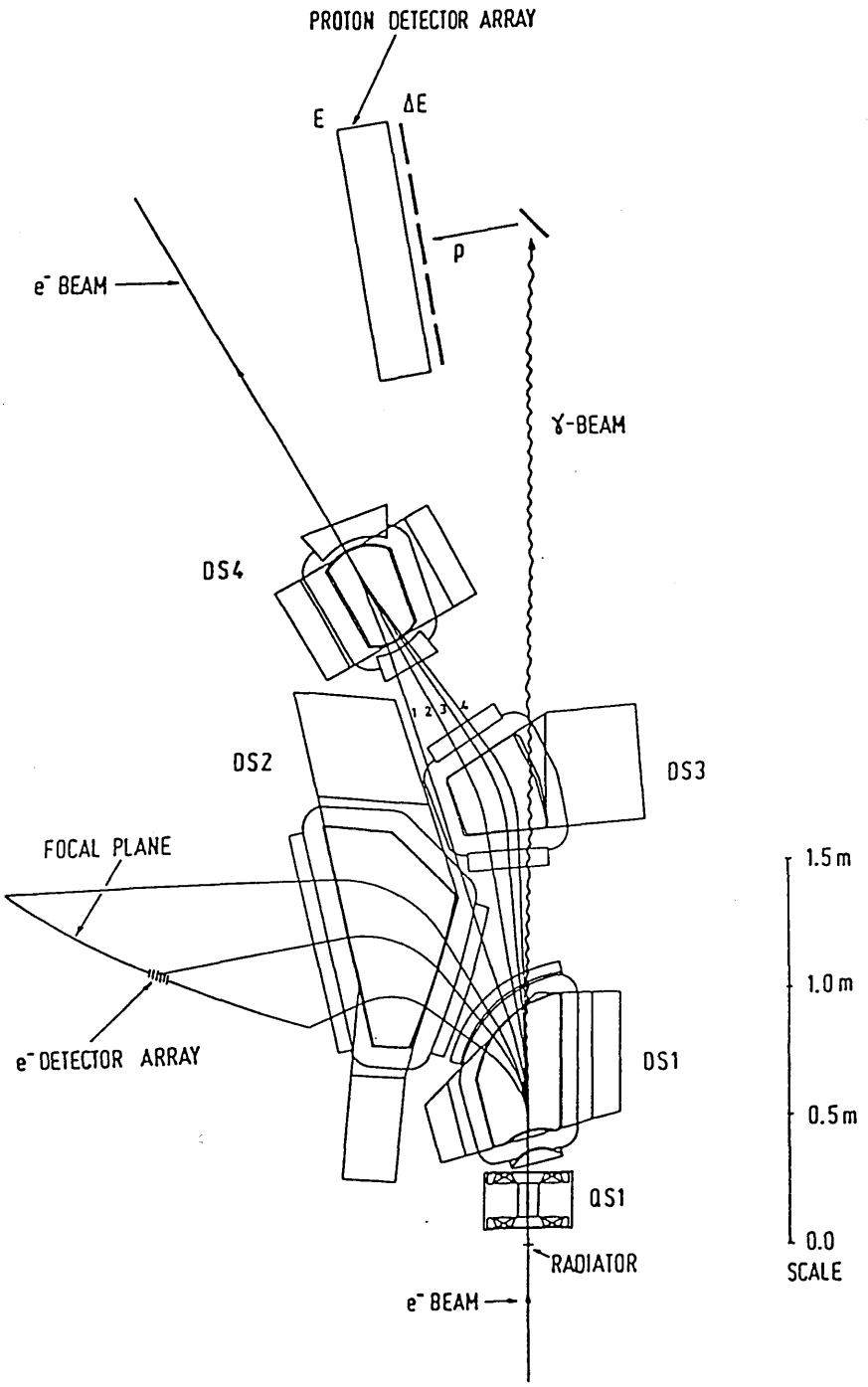

Figure 3.1 A plan view of the Mainz microtron *tagged* photon spectrometer, showing the focal plane position, the four main beam trajectories through the system and the positioning of the photoproduct detectors.

3.2 The $D(\gamma, p)n$ Measurement

The target used in this experiment comprised of two $15 \times 10 \times 0.1$ cm sheets of deuterated polyethylene plastic, manufactured by E. Merck Ltd. of Darmstadt, West Germany. The targets were quoted as having a 1 % tolerance in thickness and having a purity of 99 % . Sheets of deuterated plastic were chosen in preference to powdered deuterated plastic[4] or heavy water, D_2O, to facilitate setting up the target and simplifying the manufacture of the target holder. The target holder is made up of a rectangular metal frame, connected to a motorised drive which is used to determine the vertical position of the target. Clamped to the frame using two thin aluminium plates, the target is set at an angle of 30° to the photon beam. The clamping mechanism also serves to hold the target sections together, but does not intercept the photon beam, nor intrude between the photoproducts from the target and the particle detectors. A target angle of 30° was chosen, as this provides the best compromise between two competing factors;

- maximisation of target material in the photon beam to give good count rates.
- minimisation of the path length in the target of a photoproduct before it is detected.

An second photonuclear target was used, a 1 mm thick carbon target. This was chosen to have approximately the same amount of carbon as the carbon in the CD_2 target, and was also set at 30° to the photon beam.

3.2.1 Proton Detector

The proton detector, as shown in the general scheme Fig. 3.1, stands in air some 50 cm from the photonuclear target, and subtends a solid angle of some 1000 msr. A detailed description of the detector is given by MacGregor[27]

A schematic diagram of the detector is shown in Fig. 3.2. The detector consists of two sections. The first is an array of three NE 102A plastic scintillator blocks, of dimensions $100 \times 11 \times 13.5$ cm, positioned parallel to the photon beam, with a 12.5 cm diameter photomultiplier tube coupled to each end of each block. This section of the detector provides the proton energy and horizontal position of the proton, and is called the E detector. Particle identification is enabled by the preceeding section, which is comprised of 5 thin plastic NE 102A scintillators, of dimensions $41.5 \times 20 \times 0.3$ cm. These are mounted vertically in front of the E detectors perpendicular to the photon beam. Each end of these scintillators is optically coupled to a 5 cm diameter photomultiplier tube by means of a twisted perspex light guide. This section is called the ΔE detector. The relative positions of the E and ΔE detectors are shown in Fig. 3.3, and their relationship to the target and the beam, is shown in Fig. 3.1.

3.2.2 Proton Detector Electronics

The proton detector logic electronics shown in Fig. 3.4, provide the signal indicating the detection of a photoproton. This signal is called the X-Trigger, and is produced from the logical examination of the outputs of the 16 photomultipliers of the proton detector array.

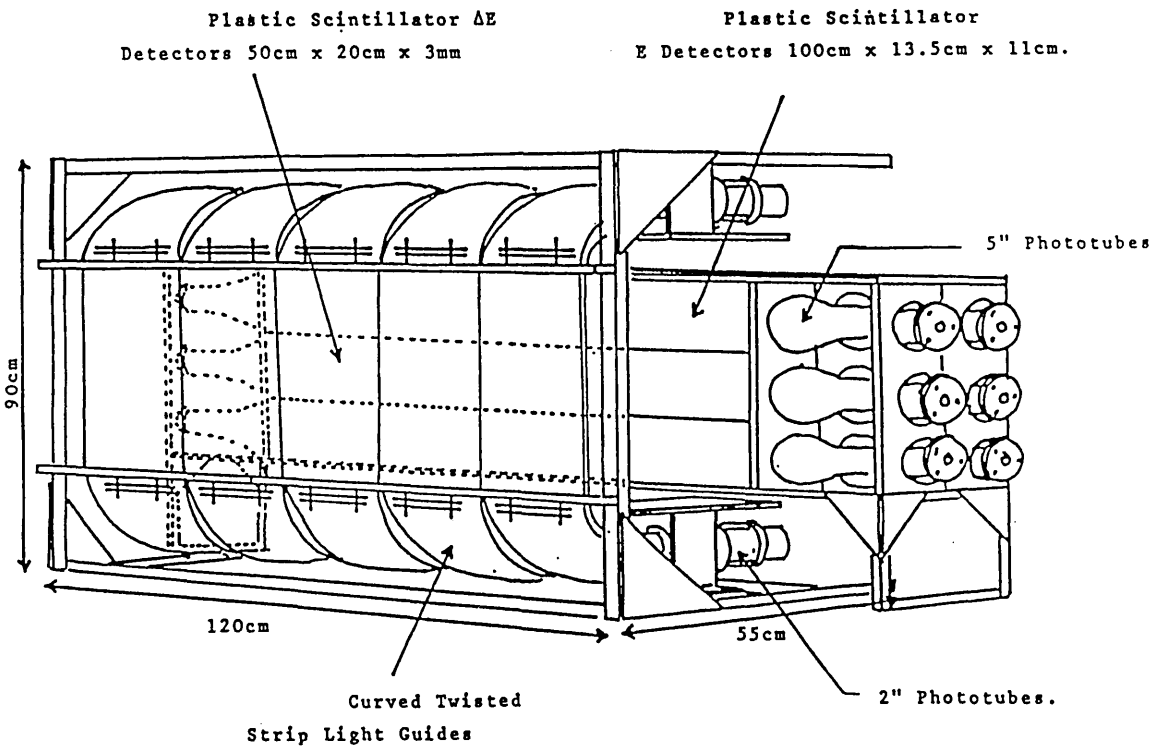

Figure 3.2 The proton detector showing the E and Δ E arms.

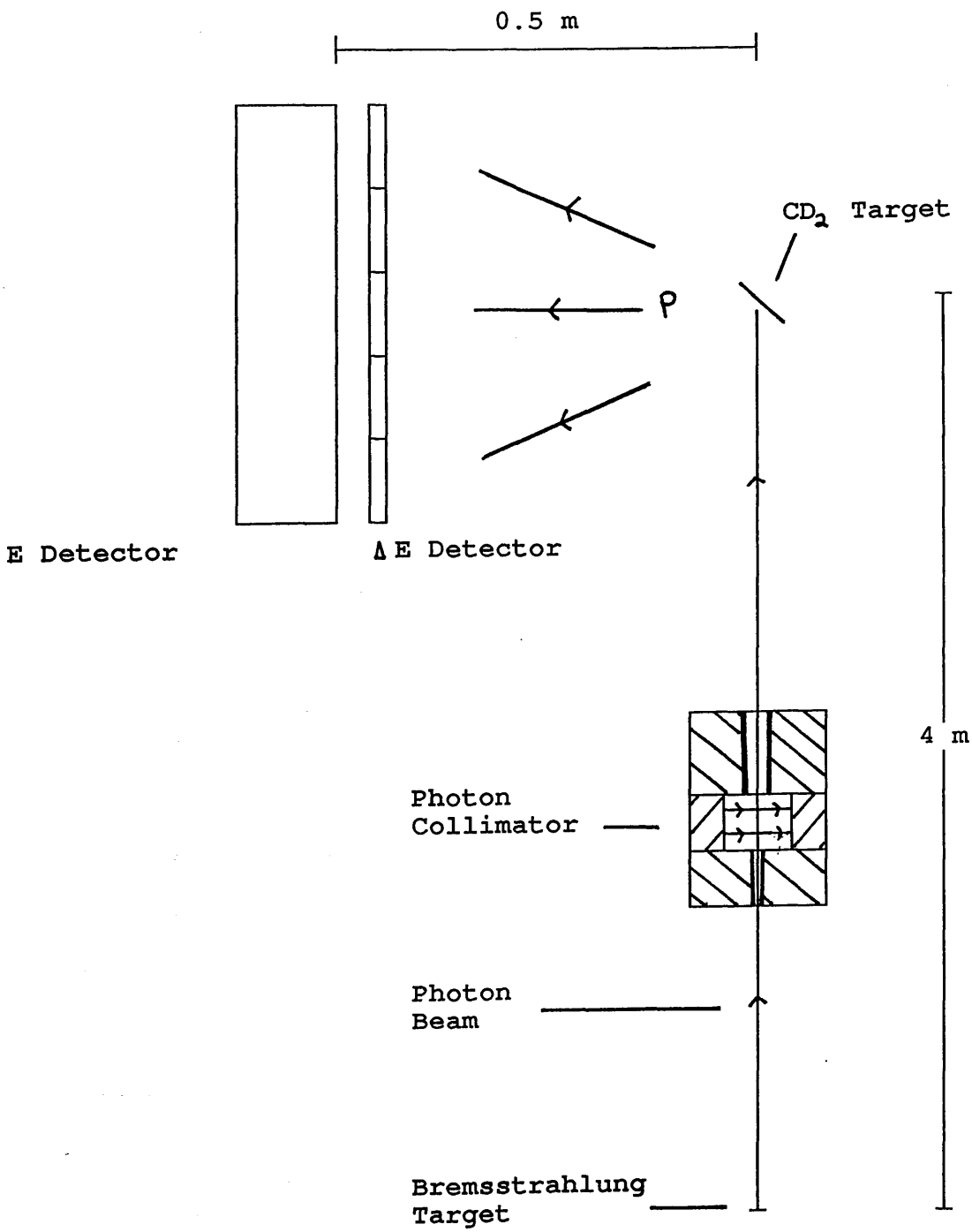

Figure 3.3 Schematic diagram showing location of proton detector.

Initially each photomultiplier signal is sent to a discriminator, the level of the discriminator being set above the thermal noise of the photomultipliers. Output pulses from each end of the same element of an E or ΔE detector, are fed into a mean timer. The mean timer gives a single output pulse, which is emitted at a time related to the mean arrival time of the two input pulses. This allows a measure of when a particle was detected, which is independent of the position in the detector where the interaction occured, and is unaffected by the different light collection times to the phototubes at opposite ends of the scintillator block. The mean timer output signals are gathered together in two fan-in units one for the E detectors and one for the ΔE detectors. These units provide a single pulse to indicate if an E or a ΔE detector was activated above the pulse threshold level. Since all valid events will produce signals in both the E and ΔE detectors, this condition is tested by using the fan-in outputs as inputs to a coincidence unit. An output signal from this unit indicates that an event produced signals from both ends of at least one E and one ΔE detector element.

However some of these events can be rejected as being invalid. One such event is the detection of particle in both E1 and E3 blocks. To detect and eliminate such events, the mean timer outputs of E1 and E3 are fed to a conicidence unit. Since the logical NOT output is used this only provides a signal if events were not detected in E1 and E3 at the same time. The rejection of further events is possible, if the event detected can be shown to be an electron. This is accomplished using the electron reject circuit. Electron events can be distinguished from proton events, by examination of the relative amount of energy deposited in the ΔE and E detectors. Since protons deposit more energy in both ΔE and E

scintillators, a discrimination level can be set on the summed ΔE and E signals

An X-Trigger signal is the coincidence signal of these three elements. Indicating that, a particle was detected in both an E and a ΔE detector, scintillator elements E1 and E3 were not activated simultaneously, and the particle was not identified as an electron.

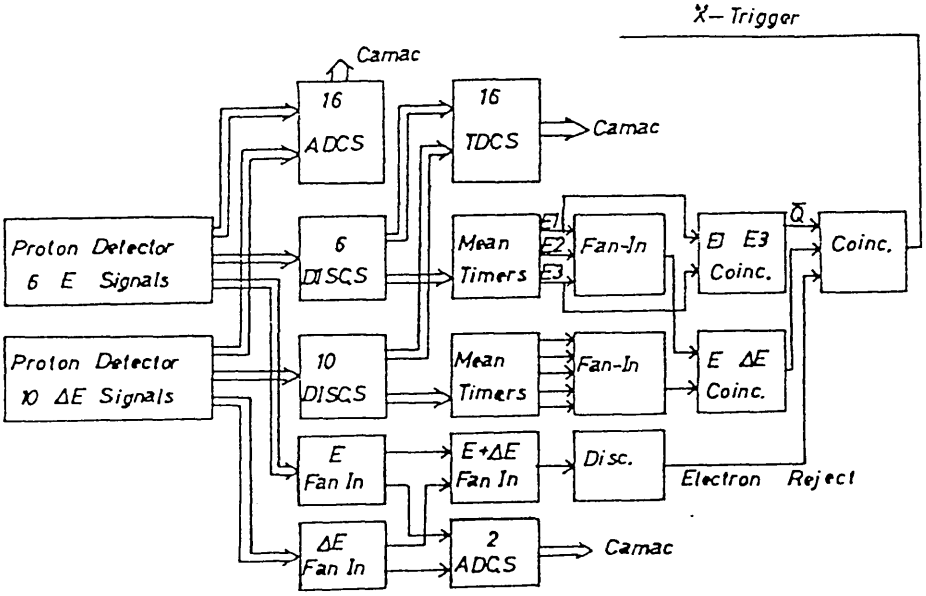

Figure 3.4 Proton detector electronics.

3.3 Data Acquisition

3.3.1 Signal Processing Electronics

Before any data are recorded, a decision must be made as to the validity of each event. That is, there must have been a coincidence between an element of the focal plane detector and an X-Trigger from the proton detector. In setting up the coincidence circuitry, the flight times of the photons, scattered electrons and the subsequent products of the photodisintegrations, the processing time of the electronics of the ladder and particle detectors and finally, the cable distances to the signal processing electronics, must be taken into account.

Because the bremsstrahlung scattered electrons in the bremsstrahlung interaction are travelling close to the speed of light, the signals from the focal plane detector are early in comparison to the signals produced by the particle detectors. There is also a 5 nS variation in the time of arrival of electrons at opposite ends of the focal plane, due to the different path lengths through the magnetic field of the spectrometer. However, since the protons detected are less numerous than the fast electrons, it is the proton detector which controls the initiation of event examination. Consequently, the ladder detector signals, are delayed to arrive at the processing electronics after the proton signals. The delays employed vary across the focal plane, therefore eliminating the effect of the different path lengths of the electrons to the focal plane. In the following sections the processing electronics are described, a block diagram of which is shown in Fig. 3.5.

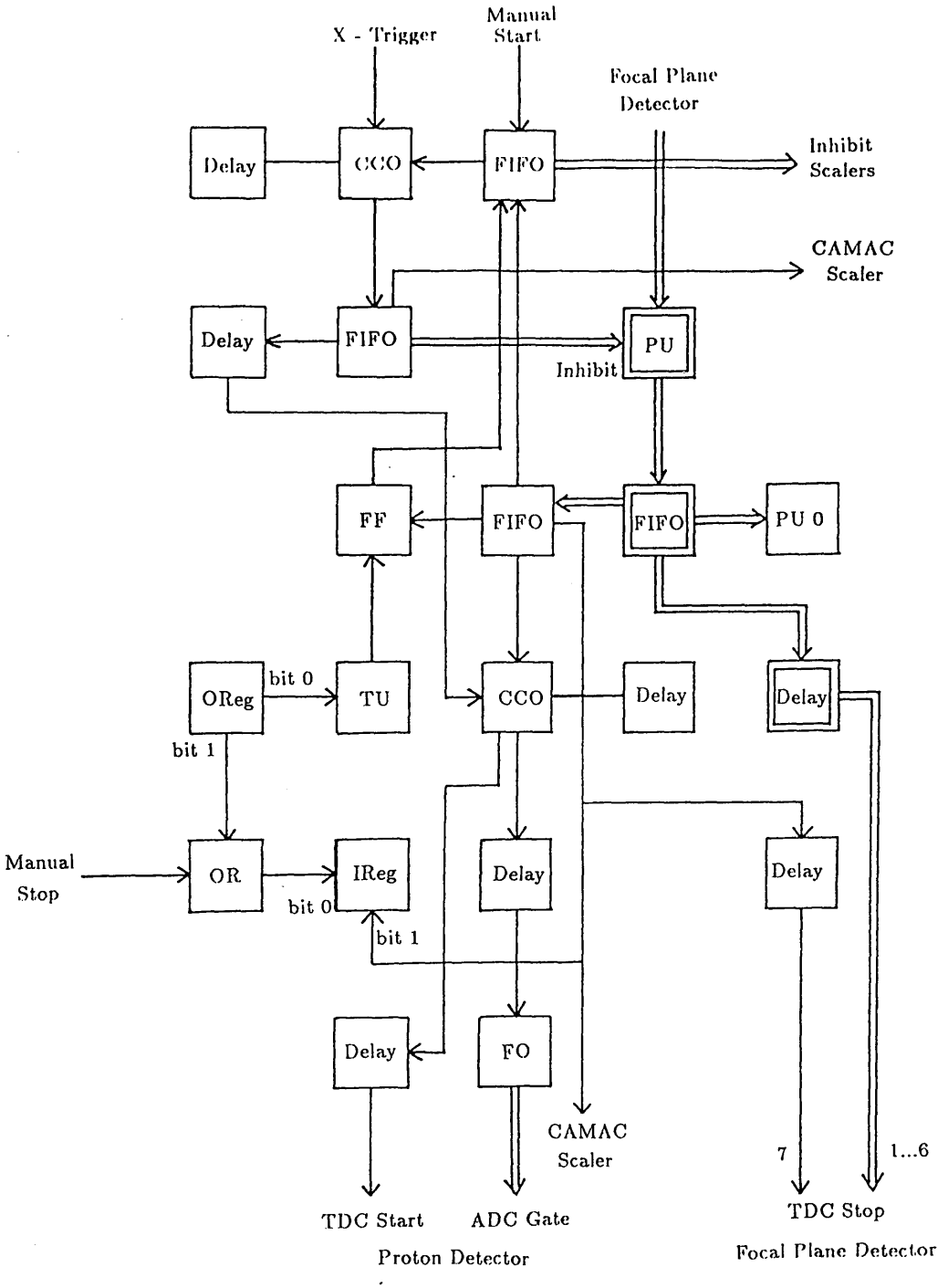

Figure 3.5 Block diagram of the signal processing electronics. Double boxes indicate 6 identical units. CCO - cable coincidence unit; FF - Flip Flop; FO - Fan Out unit; FIFO - Fan In Fan Out unit; PU - bit pattern unit; TU - Timing unit used as a variable delay. IReg and OReg are Input and output data registers.

Signals from the proton detector (X-Trigger) enter a cable coincidence (CCO) unit. This is a coincidence unit in which the length of a delay cable is used to set the output pulse width. The pulse width produced is the resolving time of the system, that is the length of time for which the pattern units are de-inhibited and will accept information from the ladder detector. In this experiment the gate width was set at 30 nS. The CCO unit is gated by a Fan-In Fan-Out (FIFO) unit, which disables the CCO if an event is already being examined i.e. if a coincidence has been found between an X-Trigger and an element of the focal plane.

The information from the focal plane detector is received by pattern units, which are a series of gated registers providing a bit pattern of the 91 channels of the focal plane detector. There are 6 pattern units used in this experiment to accommodate the 91 channels. The pattern units are enabled by the pulse shaped X-Trigger and will accept information for the period of the pulse. Six FIFO units are used to provide a single signal from each of the 6 pattern units. The signal is then fed to the stop input of a TDC associated with the pattern unit. The outputs of these FIFO's are fed to a further FIFO which produces a single signal indicating if a channel was activated on the entire focal plane detector. This signal is also used as a stop input of a TDC used to cover the entire focal plane. In addition, each of the OR signals from the focal plane detector is fed to CAMAC scalers, to provide count rates for each section of the focal plane, information which is required for normalisation purposes.

A coincidence is then produced between the focal plane signal and the X-Trigger. If a channel on the focal plane has been activated then the Input Register of the CAMAC crate is set, an interrupt signal is sent to the HP1000 computer and the FIFO which disables incomming X-Triggers is set. The coincidence signal is also used to start all TDC's and gate all ADC's.

3.3.2 The Data Collection Code MESS4

The data acquisition program, MESS4[28], was written to be a flexible way of transferring data from the electronics to the HP1000 using CAMAC. It is flexible since it can accept data from one or more CAMAC crates, with each crate containing different units with varying memory requirements. Before an experiment commences, details of the types of modules and the related memory space must be transferred to the HP1000 computer, from which the program is run. A *parameter* file is accessed, which contains information on the order, number and memory requirements of ADC's, TDC's and SCALERS. The only restriction imposed by the program is in the order in which the modules being used are located in the CAMAC crates.

When running, the program waits for a look - at - me (LAM) from the CAMAC crate controller, this signal prompts the HP1000 to perform a blanket read of the CAMAC crate(s). The LAM occurs if there has been a coincidence between an X-Trigger and one of the pattern unit registers. Information is passed serially from the CAMAC to the HP1000, along some 150 m of cable. Once read,

the computer reduces the retrieved data, by discarding all zero entries in the information, such as empty slots and units which were not activated during the event. This compressed information is deposited on magnetic tape and then sent to an HP3000 computer.

The HP3000 contains an online graphical display program PAUS[29] which gives immediate visual evidence of the progress of the experiment, i.e. the spectra produced by the ADC's and TDC's, or any combination of them, may be examined online. This enables individual detectors to be monitored at will, and detector failures to be identified.

Chapter 4

Data Analysis

4.1 The BEAUTY Code

The stored event by event data accumulated by the data collection system MESS4 consists of information coming from the following;

- 91 Pattern Unit registers.
- 16 ADC outputs from the proton detector.
- 7 TDC outputs from the focal plane detector.
- 16 TDC outputs from the proton detector.
- 12 Scalers for the focal plane detector.
- Scalers for Interrupts, X-Triggers, Clock Time and Live Time.

Decoding of this data into useful information, is performed using the computer code BEAUTY[30].

Data reduction is an important feature of the code, since many events which are recorded may not originate from protons or may be random proton events.

The BEAUTY program enables such events to be discarded, reducing the data set and decreasing the processing time. Decisions upon which events are to be discarded, can be made by the examination of the spectra compiled by the program, from the ADC, TDC and pattern unit information. As well as these spectra accumulated directly from the experimental detectors, the program allows new user defined spectra to be constructed. Such new spectra can be any manipulated combination of the ADC's, TDC's, pattern units and scalers employed in the experiment.

The examination of the spectra is by the graphical display subroutines of the Beauty code, employing as its basis callable GHOST-80 graphics subroutines. Spectra produced by the program can take the form of one or two dimensional graphical displays. This includes x-y plots, histograms, scatter plots and contour plots. To exclude invalid data, conditions or constraints defined by the user can be imposed upon the spectra. The conditions can be logically combined to provide a tight constraint upon the validity of recorded events.

4.2 Position Calibration

Emission angle information on the proton i.e. where it enters the E and ΔE detectors, is obtained by finding the time difference between the photomultiplier signals from each end of an E or ΔE segment. To achieve a reference point against which the pulses from either end of a piece of scintillator can be measured, a *mean timer* is employed. The output pulse of the *mean timer*, is then used as the start pulse for the TDC's examining the outputs of the same scintillator segment. The time difference is obtained by subtracting the TDC values from either end of a detector segment. This can be expressed as follows,

$$Position = \frac{(TDC_a - TDC_b - C)}{m} \tag{4.1}$$

where TDC_a and TDC_b are the TDC outputs (channel number) produced from either end of the same scintillator segment, m , is the gradient in units of channels per cm and C is an offset channel constant.

Fixed points on the detector were defined by placing a 1.0 cm thick metal plate in front of the proton detector, the plate having 30 holes of 2.0 cm in diameter, positioned at regular horizontal and vertical intervals. The detector segments could be examined individually by masking any series of these holes, with metal strips of the same thickness as the plate. With the normal thin photonuclear target, such a calibration would have taken an unacceptably long time to produce reasonable statistics, so a thick target consisting of 5 mm of aluminium was used. A typical time difference plot for protons incident on an

E block is shown in Fig. 4.1, the peaks in the spectra relating to the holes in the metal plate. From this data, calibrations for each of the E and ΔE segments were evaluated. The calibrations produced for each proton detector scintillator segment are shown in Fig. 4.2 for the E block sections and Fig. 4.3 for the ΔE sections, and in tabular form in Table 4.1.

Detector	Gradient Channel Number/mm	Constant Channel Number
Δ E1	0.290	442
Δ E2	0.263	441
Δ E3	0.250	463
Δ E4	0.305	450
Δ E5	0.283	442
E1	0.303	369
E2	0.288	381
E3	0.295	342

Table 4.1 Postition calibration of the scintillator segments.

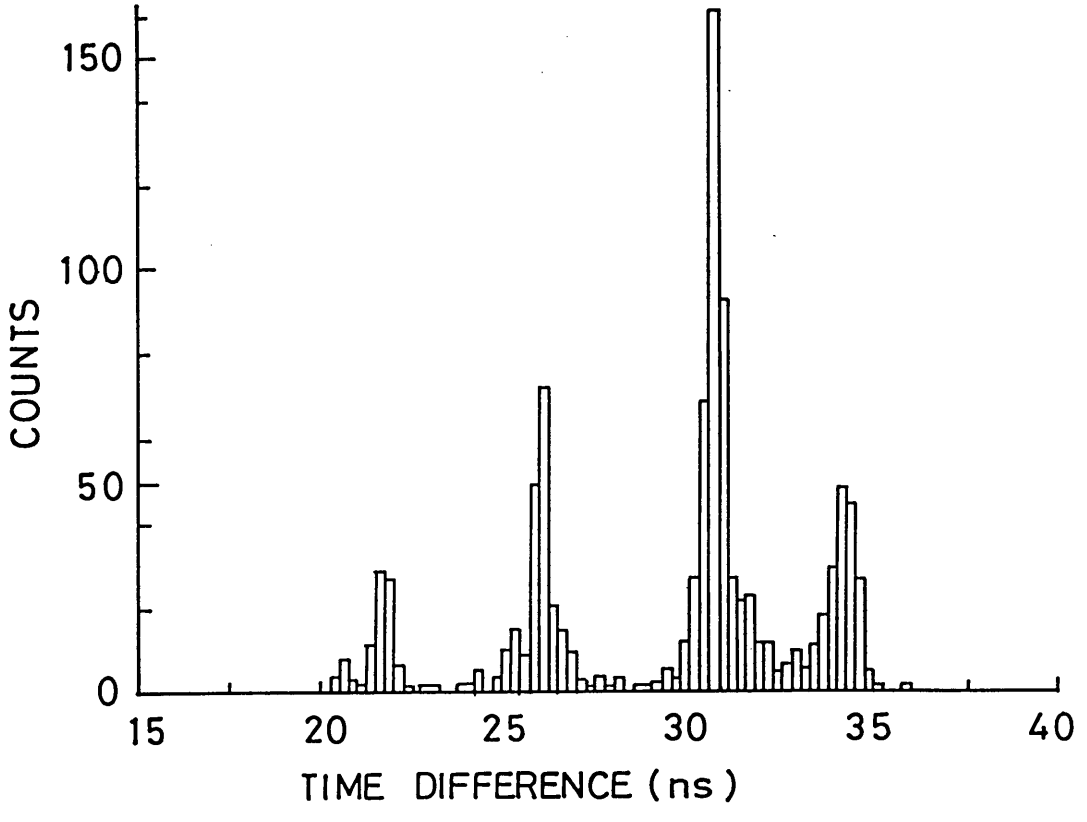

Figure 4.1 TDC difference plot for position calibration, peaks relate to sections of the E block not shielded by metal plate.

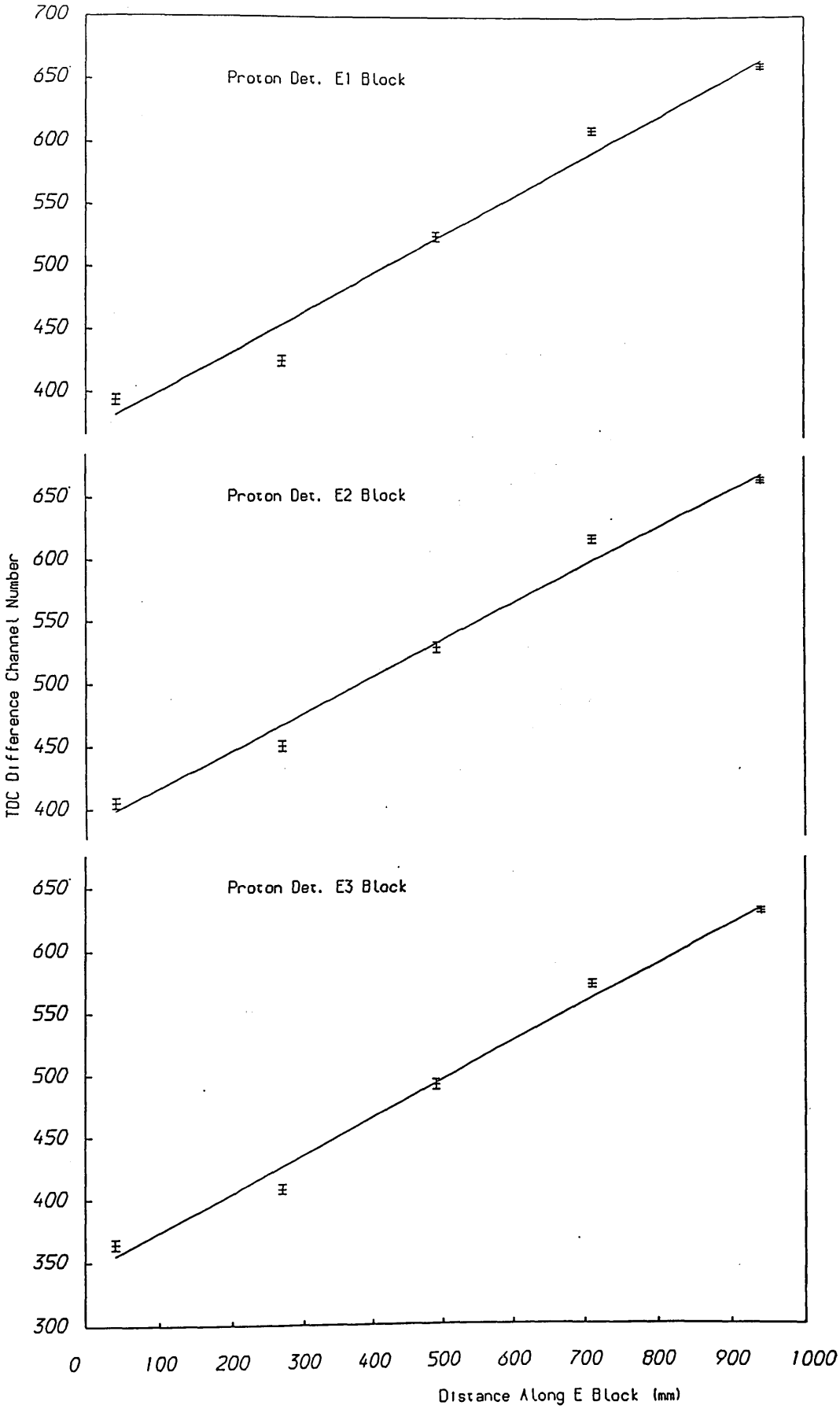

Figure 4.2 Position calibration for E block segments of the proton detector.

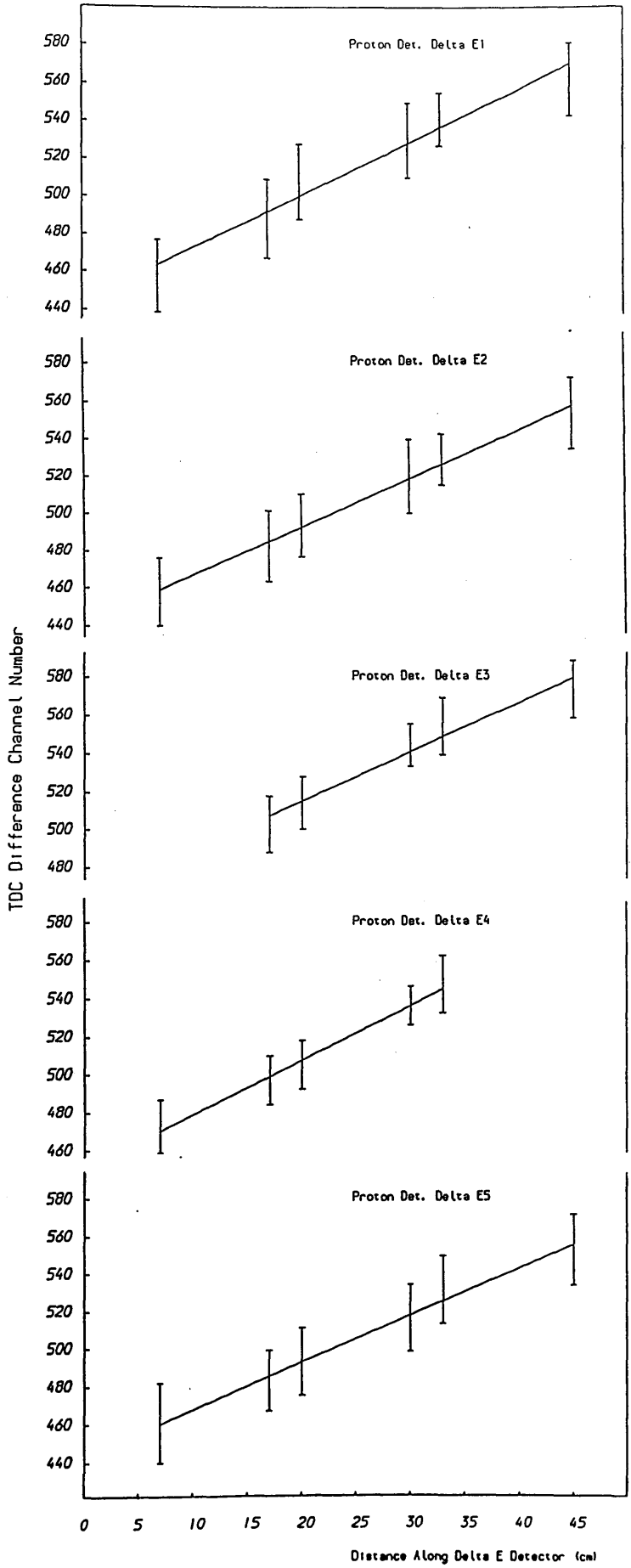

Figure 4.3 Position calibration for ΔE segments of the proton detector.

4.3 Energy Calibration

Proton energy information is derived from the ADC's which examine the E block detectors. However, the output response of the photomultpliers is position dependent, due to the variations of light collection with distance from the photomultiplier. So at the analysis stage, the proton energy is obtained using a function comprised of the ADC outputs of the two photomultpliers on an E block. It was found that the light reaching the photomultipliers of the E detector, varied exponentially with respect to the distance of the interaction from the photomultiplier. Hence the ADC reading of the photomultiplier output varies as,

$$ADC = A_{adc}e^{CZ} \tag{4.2}$$

where Z is the distance of the interaction from the photomultiplier, A_{adc} is the gain of the photomultiplier and C is a constant of the scintillator block. To construct an energy response function for each E block which is independent of the position in the block where an interaction takes place, it is necessary to use an algorithm which uses the ADC signal from both photomultipliers and which is itself position independent. The function which has these properties is:

$$f_{adc}(E) = (ADC_a \times ADC_b)^{1/2} = (A_a e^{C_a Z} \times A_b e^{C_b(L-Z)})^{1/2} \tag{4.3}$$

where the subscripts a and b indicate either end of an E block and L is the

length of that block. Clearly , the function provides a position independent evaluation of the proton energy, if we assume that the constants C_a and C_b are equal. This is a realistic assumption for similar photomultipliers at either end of the same E block. The energy of a proton interacting in an E block can now be written as:

$$Energy = \frac{(ADC_a \times ADC_b)^{1/2} - C}{m} \tag{4.4}$$

where ADC_a and ADC_b are either end of the same scintllator segment, and m is the gradient in units of channel per MeV, and C is an offset channel constant.

Due to the kinematic simplicity of the deuteron photodisintegration, it is straight forward to calculate the proton energy for any position on the E detector if the photon energy is known in either the lab or center of mass frames (See Appendix A). Since the data acquisition system provides an event by event record of an experiment, it is possible by determining the position of the proton in the detector and the energy of the photon which initiated the event, to calculate the proton energy. Hence, the deuterium data itself can be used to provide the energy response functions for each E block.

Overlap areas of the E and ΔE sections are used, as their position in the laboratory frame is already defined. Thus we have a detector comprised of 15 pixels, a pixel being the name given to an overlap area, upon which we can gate to produce the ADC reponse of that area using the ADC function. This response however, must be that produced from protons from the deuteron break-up within

a defined photon energy interval.

The resulting plots of the ADC functions for each pixel, show the spread in proton energy introduced by the target, air, ΔE detector and variations due to the location of the interaction in the target. Since the mean value of the energy losses can be calculated, the mean proton energy associated with the value of the ADC function can be found. This process was performed for each of the 15 pixels on the detector, and for the photon energies of 87, 95, 104, 113, 122 and 128 MeV, with each energy being the mean of a 8.5 MeV photon energy bite. This provided 30 calibration points for each E block. The resulting calibrations for each of the E blocks can be seen in Fig. 4.4, for E1, E2 and E3 scintillator blocks respectively, and in tabular form in Table 4.2.

Detector	Gradient Channel Number/MeV	Constant Channel Number
E1	7.27	-23
E2	7.60	-38
E3	8.07	-36

Table 4.2 Energy calibration of the E detector scintillator segments.

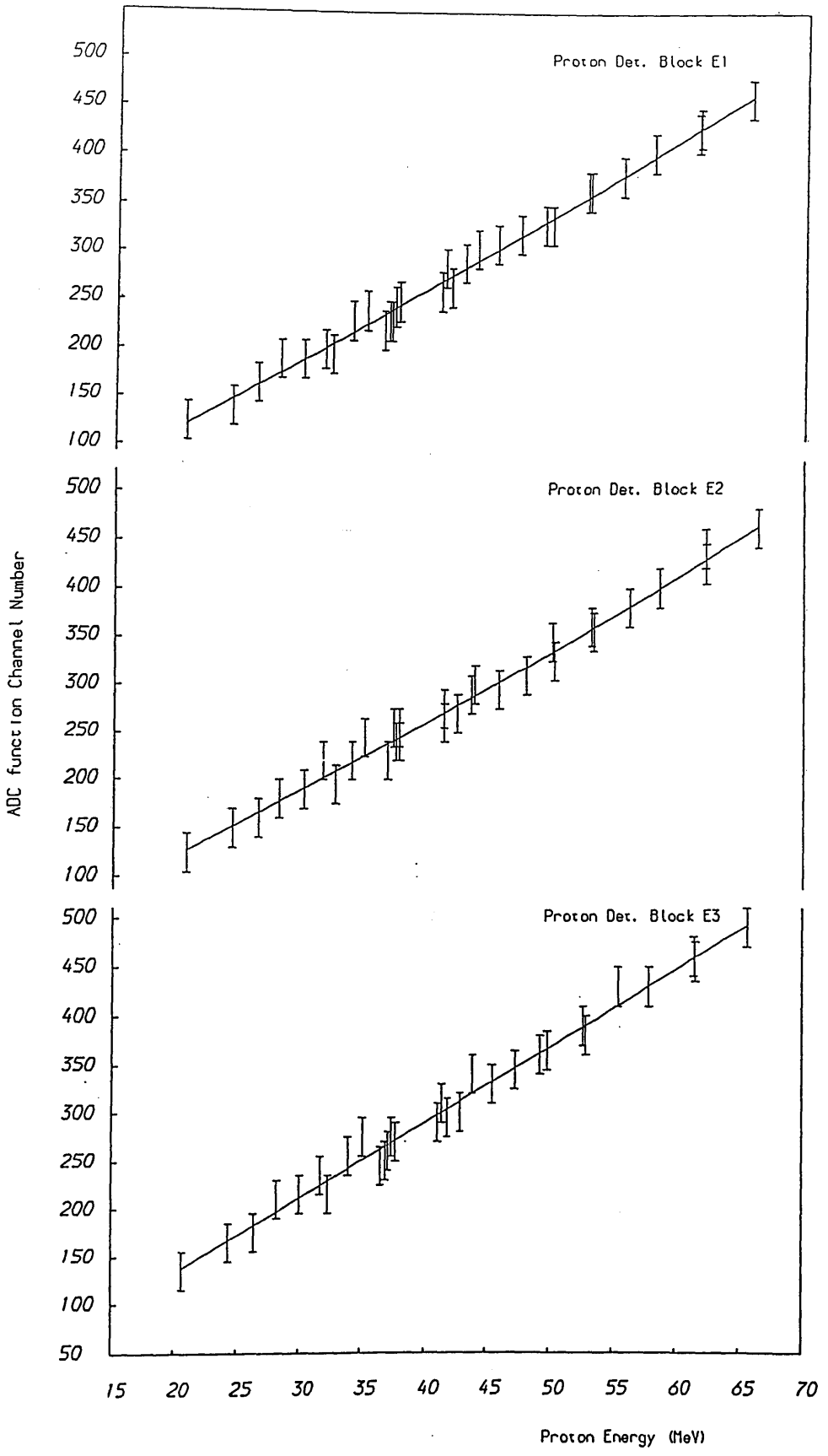

Figure 4.4 Energy Calibration for E block segments of the proton detector.

4.4 Data Reduction

For the photodisintegration of the deuteron, the analysis proceeds through a sequence of five steps. Each step imposes a condition upon the recorded data, and eliminates events which are not related to deuteron photodisintegration.

4.4.1 Identification of Protons Events

Using the well established technique, particle identification in the proton detector relies on the scatter plots E v ΔE. Plots of this kind show the ratio of energy deposited by a particle in two detectors of substantially different thickness, the first a thin medium (ΔE detector) which measures the rate of energy loss , and the second a stopping medium (E detector) which measures the particles energy. Since protons have a greater energy loss in the ΔE detector for a given particle energy, this allows them to be easily identified. Fig. 4.5 shows a scatter plot of the energy deposited in each detector for one of the 15 pixels (an overlap area of the E and ΔE detectors) of the proton detector, allowing the proton ridge to be clearly seen. The second feature to be noted on Fig. 4.5 is the operation of the hardware electron reject circuit, which has a significant effect on the electron background. It should also be noted that the energy deposited in each detector, is not represented by the ADC function described in earlier, but by the sum of the ADC readings from either end of the same E block.

Events lying within the proton ridge are retained by entering the appropriate *gating* conditions in the BEAUTY code. The curves labelled A and B in Fig. 4.5

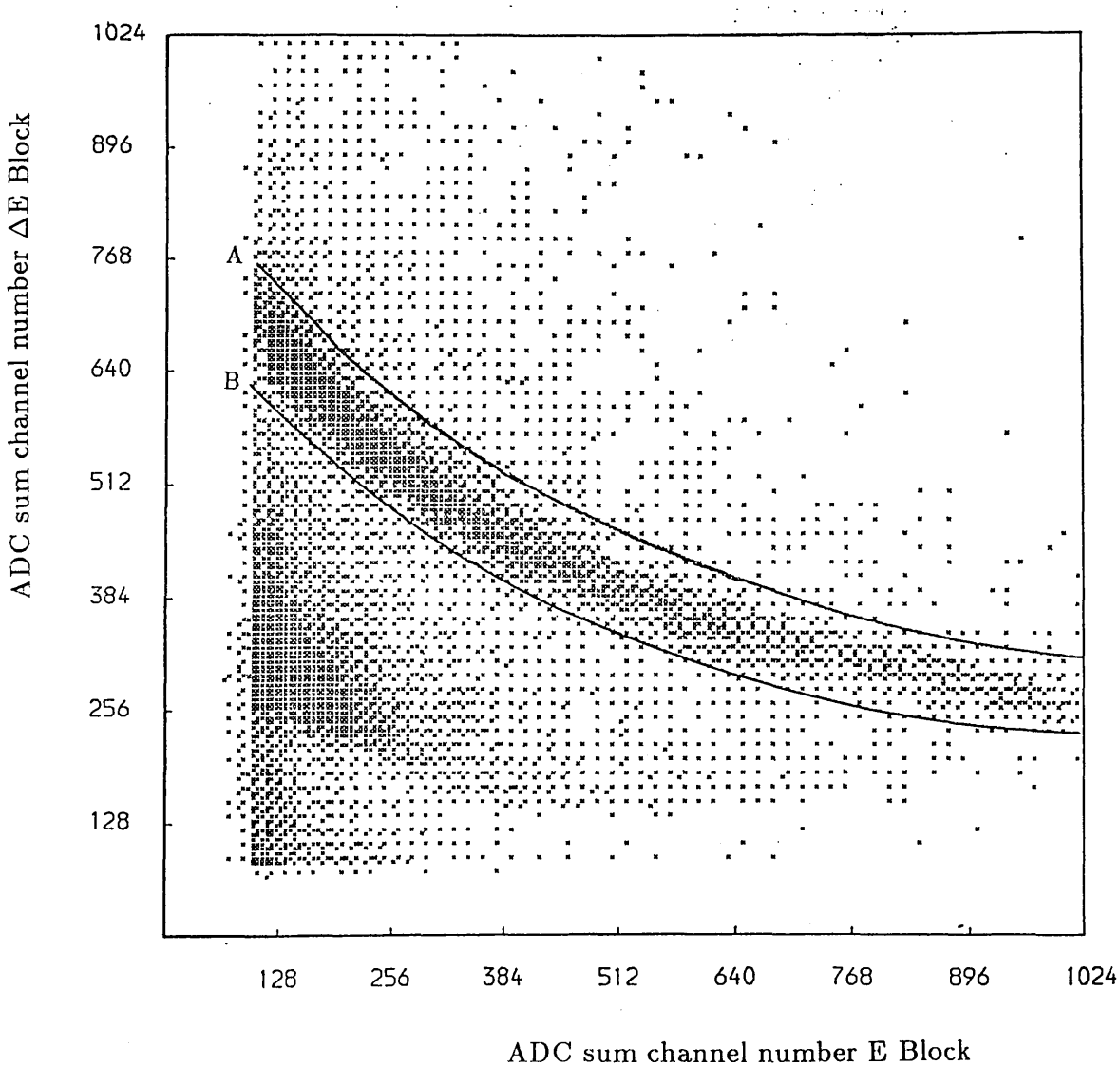

Figure 4.5 Scatter Plot of energy deposited, as represented by the sum of the ADC readings from either end of an E block v energy deposited in a ΔE, for one pixel of the proton detector.

show how the proton ridge is defined in a typical E v ΔE scatter plot. Scatter plots of this kind were produced for all 15 pixel segments of the proton detector, and the region of valid proton events identified for each. The gating condition employed to reduce the data set, was that at least one proton must have been detected for the data event to be considered valid at this stage.

4.4.2 Identification of the Prompt Protons

Since not all the photons incident on the target are *tagged*, some of the protons recorded lack the instantaneous time coincidence with the focal plane detector. In Fig. 4.6, a TDC spectrum is shown, which records the time relationship between the proton detector (start pulse) and the focal plane detector (stop pulse). This plot shows the summed TDC spectra from 16 channels of the focal plane detector, all the channels originating from the same printed circuit board. Note that this plot does not show the entire 30 nS gate, to reduce computer processing time, the data set was reduced by removing some of the non-prompt background data. The *tagged* events lie within the central peak of the spectrum, the peak width of $\approx$ 1.5 nS represents the effective coincidence resolution of the correlation, and is well within the 30 nS gate imposed by the processing electronics. The spread in this TDC spectrum is caused by the finite size of the target and detector, as a proton from any part of the target may be detected in any part of the proton detector. The remainder of the spectrum, the time continuum, identifies events which are to be rejected, as having only a random correlation in time. Again a *gating* condition is imposed which can select events present in the prompt proton

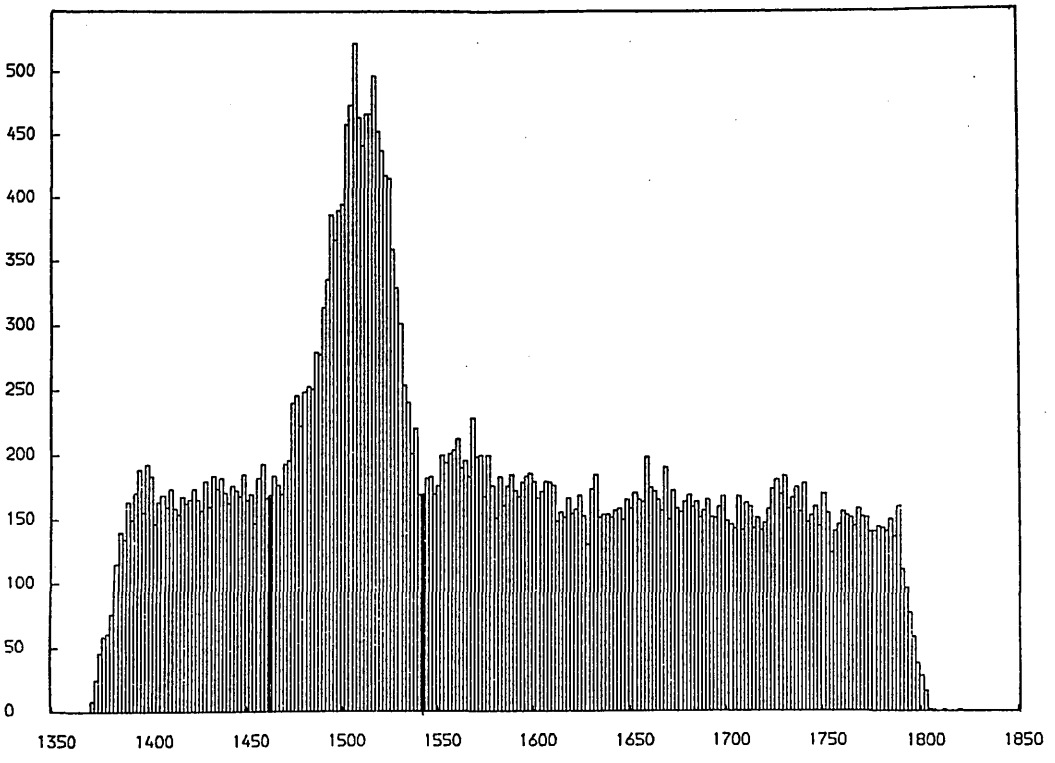

Figure 4.6 TDC spectra showing the prompt proton peak.

peak of the TDC spectra.

TDC spectra of this sort were produced for each of the 16 channel sections of the focal plane detector, i.e. 6 in total. To qualify as a valid event either only one ladder channel was activated or, two adjacent ladder channels were activated. This corresponds to an electron passing through 2 and 3 focal plane scintillators respectively. Ambiguous events, i.e. events where two non-adjacent ladder channels are activated, were rejected. In doing this however, there is a proportion of valid deuteron photodisintegration events which are discarded from the analysis. These are events where a valid deuteron event and a random event occur within the same TDC gate. However, the magnitude of this effect which is dependent on the rate at which the focal plane detector is operating can be calculated. Details of the calculations are given in section 4.6 . The appropriate correction is then applied to the analysis when the absolute differential cross section is being evaluated.

4.4.3 Background Subtraction

This section describes the procedure adopted to subtract the random continuum which lies underneath the central prompt peaks such as the one shown in Fig. 4.6. The number of events under the prompt peak can be estimated by interpolation from the shape of the time spectrum which lies outwith the peak. However, to determine the effect of the random background on the shape of the deuterium angular distribution it is necessary to analyse a subset of the data which only relates to the background. This is done by selecting a section of the continuum

which has the same area as the background beneath the prompt peak, but which of course lies outwith the prompt peak. Both data sets are analysed simultaneously in such a way that for any spectrum being generated, counts are added if they came from the prompt region, but subtracted if they came from the random continuum region.

4.4.4 Identification of Photoprotons from the Deuteron

On examination of the deuteron kinematics, we can see that the energy of the proton is defined (See Appendix A) by the incident photon energy and the emission angle of one of the photonucleons, in this case the proton. Therefore, in a scatter plot showing proton position on the proton detector versus proton energy, as represented by the ADC function, we can expect to observe a noticeable correlation if the photon energies are limited to a narrow range of values. Indeed, Fig. 4.7 shows this correlation, the deuteron ridge. If such a plot is produced from a carbon only target we observe no correlation. Fig. 4.8 shows data from a carbon only target which is at the same stage of analysis as the CD_2 data shown in Fig. 4.7, and as expected it can be seen there is no ridge. By gating on the deuteron ridge we can therefore isolate deuteron type events from the deuterated polyethylene target. Scatter plots of the kind shown in Fig. 4.7, were produced for each E block of the proton detector and for 6 incident photon ranges. Since each 16 channel section of the focal plane detector measures a different range of photon energies, this was a convenient division of the incident photon spectrum.

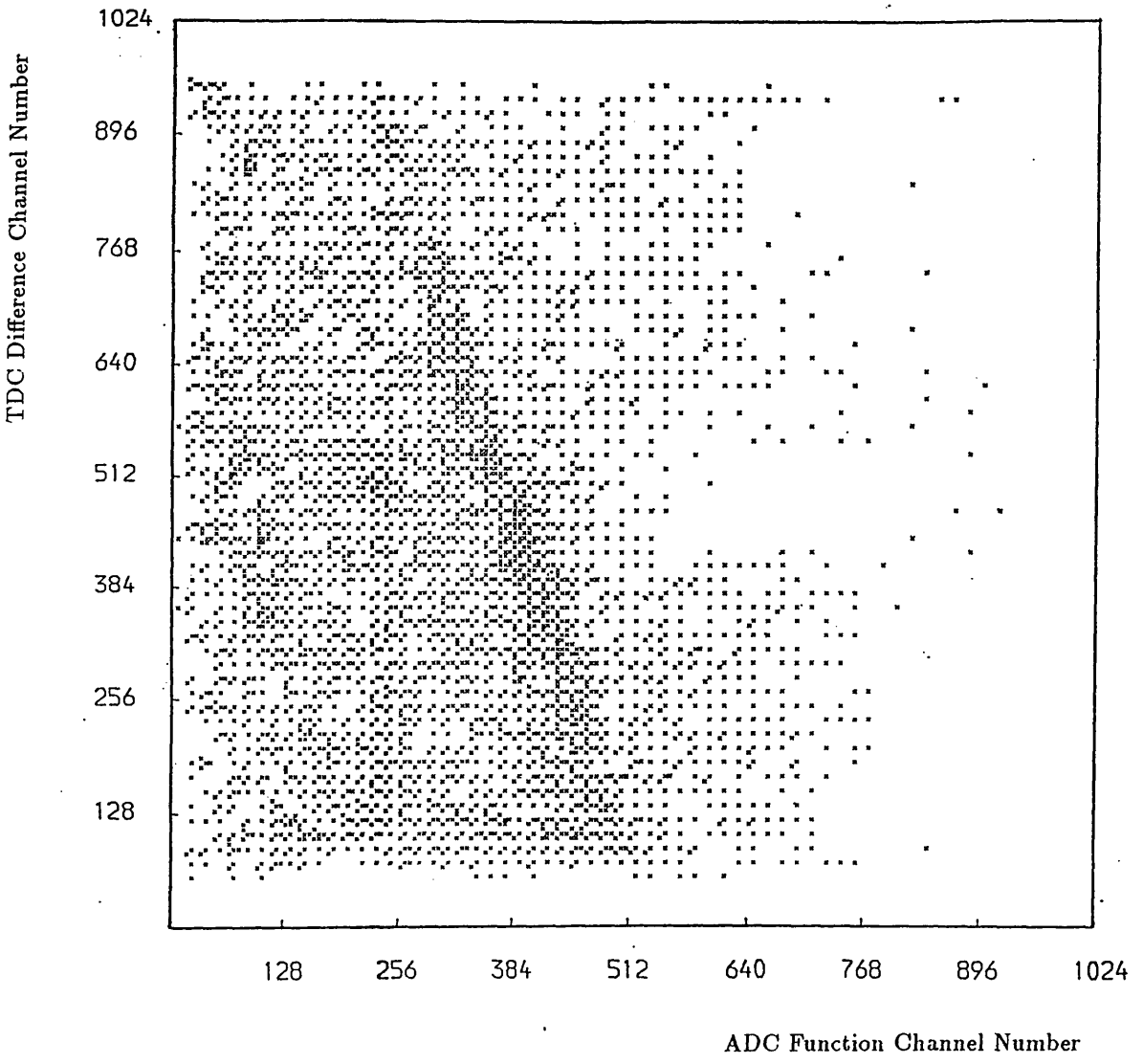

Figure 4.7 Energy (ADC function) v position on the E block (TDC difference) for prompt protons from CD_2 , showing the deuteron ridge.

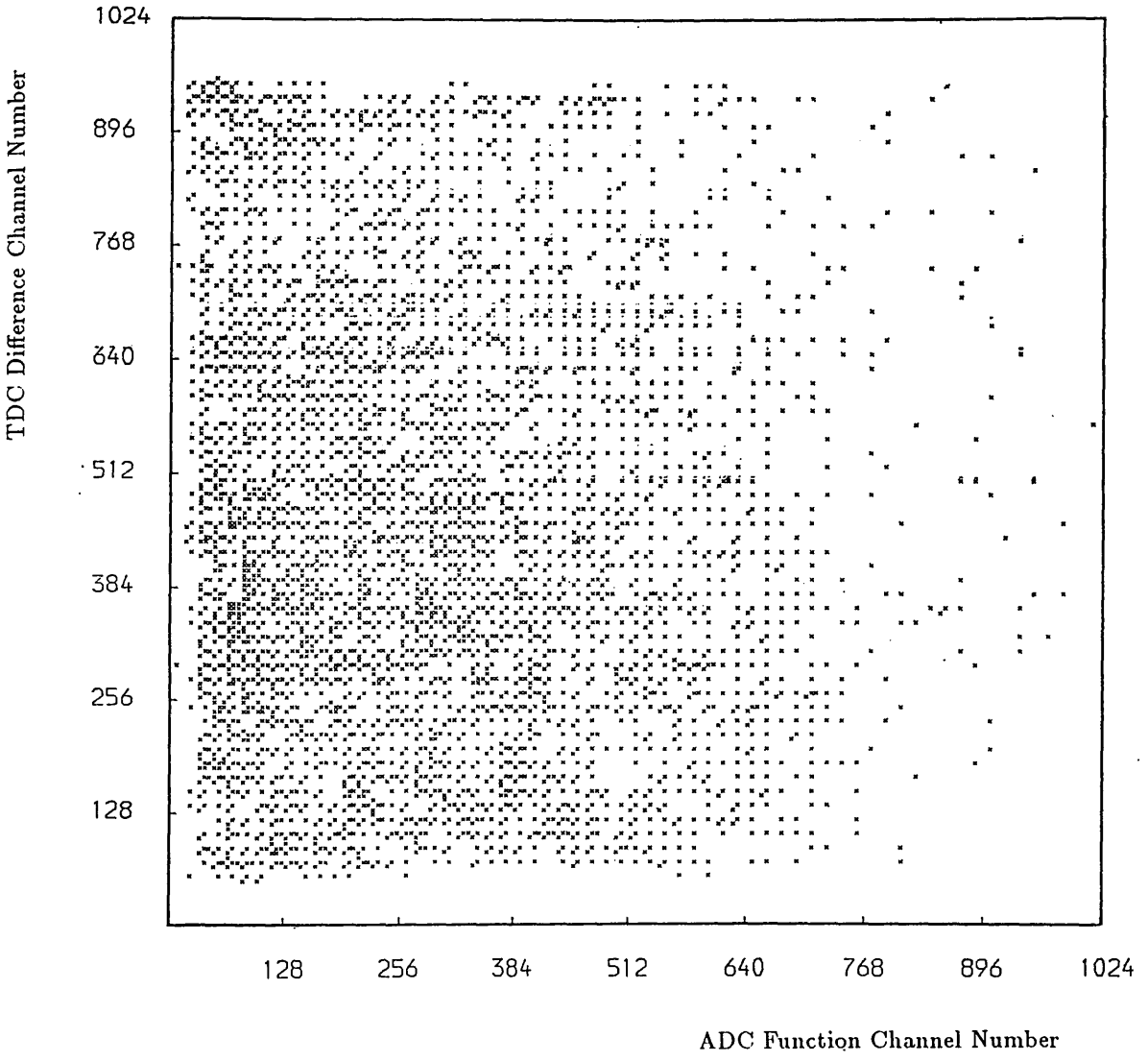

Figure 4.8 Energy (ADC function) v position on the E block (TDC difference) for prompt protons from a carbon only target, no deuteron ridge is apparent.

The mean photon energies defined by each focal plane detector section are 87, 95, 104, 113, 122, and 128 MeV, each energy being the mean of an 8.5 MeV energy bite.

At this stage of the analysis, the initial data set has been reduced to those events in which prompt protons satisfying the kinematical conditions of deuteron photodisintegration were detected. In addition to this, random events from the time continuum have been subtracted. The data now consists only of deuteron and carbon events which meet these criteria.

4.5 Carbon Subtraction

The presence of a carbon background, beneath the deuteron ridge, dictated that a carbon only target had to be used to simulate the carbon in the deuterated polyethylene target. This would enable the number of carbon events present in the deuteron ridge to be ascertained and subtracted from the angular distribution.

To this end, data were taken using the carbon target described previously. The data were then treated in an identical fashion to the deuterated target as described in the preceding sections. In this way the carbon background present under the deuteron ridge was measured. Before this data could be subtracted from the spectra accumulated from the deuterated polyethylene target data, a correction had to be made due to the differing target densities and thicknesses, as well as the different experimental live times. The correction factor can be quantified as

$$C_F = \frac{N_{\gamma CD_2}}{N_{\gamma C}} \times \frac{N_{N_{CD_2}}}{N_{N_C}} \times \frac{t_{CD_2}}{t_C} \times \frac{\epsilon_{CD_2}}{\epsilon_C} \tag{4.5}$$

were $N_{\gamma CD_2}$ and $N_{\gamma C}$ are the number of photons incident on the deuterated polyethylene target and carbon targets respectively, $\frac{N_{N_{CD_2}}}{N_{N_C}}$ is the ratio of the number of carbon atoms in the deuterated polyethylene target and the carbon target per unit cross sectional area, t_{CD_2} and t_C are the live times for the two measurements and, ϵ_{CD_2} and ϵ_C are the *tagging* efficiencies for the two measurements. For the present experiment , the average correction factor for the focal plane is 4.56, with a variation across the focal plane of 4.51 to 4.61.

4.6 Statistical Correction

The *gating* conditions imposed upon the data by the computer code Beauty, perform the task of eliminating random events. However, data events which recorded 2 or more non-adjacent focal plane detector channels as having fired were also eliminated as ambiguous events, since E_γ could not be defined. It is clear that a proportion of such events are a real and a random event detected in coincidence and that these events must be accounted for. The proportion of such events is dependent upon the rate of random events detected on the focal plane detector, since the number of real events is small and is determined by the cross section of the reaction. Examination of the random events occuring on the focal plane has indicated that they can be successfully described by a Poisson distribution.

$$P(n,\alpha) = \frac{e^{-\alpha}\alpha^n}{n!} \tag{4.6}$$

where $\alpha = N\Delta t$ is the statistical parameter, N is the rate of the focal plane detector and Δt is the coincidence gate width, and n can take the values 1,2,3 ...,k, ..., this being the number of random events detected. So the probability of a single random event being detected in a time Δt is

$$P(1,\alpha) = e^{-\alpha}\alpha$$

and for two random events within the gate the probability is

$$P(2,\alpha) = \frac{e^{-\alpha}\alpha^2}{2}$$

and so on. To find the probability of a real event being detected when no random events where detected we use;

$$P(0,\alpha) = e^{-\alpha}$$

For this experiment the coincidence gate width was set at 30 nS, but the focal plane detector rate varied throughout the experiment. At a focal plane detector rate of 1×10^6 the probability of single real events is 0.97, while at 1×10^7 the probability drops to 0.80. To adjust the data for the loss of real events due to coincidences with random events, a factor of e^{α} must be applied to the data. For the deuterated polyethylene data the probability of detecting a single real event was 0.75, while for the carbon target the factor was 0.70.

4.7 Normalisation

After the application of the corrections due to the random events on the focal plane detector, the angular distributions from the deuterated polyethylene and carbon targets under the deuteron ridge may be subtracted, leaving an angular distribution of the photodisintegration of the deuteron. This is performed for each of the six photon energy bites. The distributions are converted into the center of mass frame (See Appendix A). Differential cross sections are obtained by normalising, for solid angle, number of target atoms and number of incident photons with the dead time effects accounted for. i.e. the differential cross-section is;

$$\frac{d\sigma}{d\Omega_\Theta} = N_\Theta \times \frac{1}{d\Omega_\Theta N_\gamma N_N t \epsilon_F} \tag{4.7}$$

where $d\Omega_\Theta$ is the solid angle between Θ and $\Theta + d\Theta$ on the proton detector, N_γ is the number of incident photons, N_Θ is the number of counts between Θ and $\Theta + d\Theta$ on the proton detector, N_N is the number of target nucleons per unit volume, t is the thickness of the target in the beam direction, and ϵ_F is the efficiency of the tagging process. The final units for the differential cross section are μbarns/steradians per nucleon, per incident photon.

4.8 Summary of Data Analysis

The preceding sections describe how a differential cross section may be derived from the recorded data. This may be summarised as follows;

- The identification of proton events and the rejection of electron events, on a pixel by pixel basis using E v ΔE scatter plots.
- The identification of prompt protons and the rejection of random events, for each of the six focal plane detector TDC's.
- The subtraction of random events within the prompt proton regions, by using a similar region from the random continuum.
- The identification of deuteron type events for each of six photon energies and for each E block, by employing the correlation between emission angle (time difference spectra) and energy (adc function) of protons from the deuteron break-up.
- The subtraction of the carbon background beneath the deuteron ridge, by analysing carbon only data as above, for each of the six photon energies and three E blocks.
- The inclusion of a statistical correction to account for real and random events detected within the same TDC gate.

- The summation of the angular information from the three E blocks, and the conversion from lab frame to center of mass frame, for each of the six photon energies.

- The normalisation of the six angular distributions and the conversion into differential cross sections.

4.9 Presentation of Results

The differential cross section for the photodisintegration of the deuteron are presented in Fig. 4.9, at photon energies of 87, 95, 104, 113, 122 and 128 MeV each energy being the mean of an 8.5 MeV energy bin.

The sources of error in this experiment come from several areas, statistical counting errors, tolerances of the targets and uncertainty in the experimental determination of the efficiency of the *tagging* process. Statistical errors for N_γ are small, while the counting errors for N_Θ are not insignificant. The major systematic error found is in the determination of the *tagging* efficiency. While the assigned error in the solid angle normalisation is at the 1 % level, this being the accuracy of the mathematical computing package used. Tolerances of the photonuclear targets are quoted as 1 % by the manufacturers. The assigned error bars are calculated from the statistical counting errors of each energy bin, and the systematic errors mentioned.

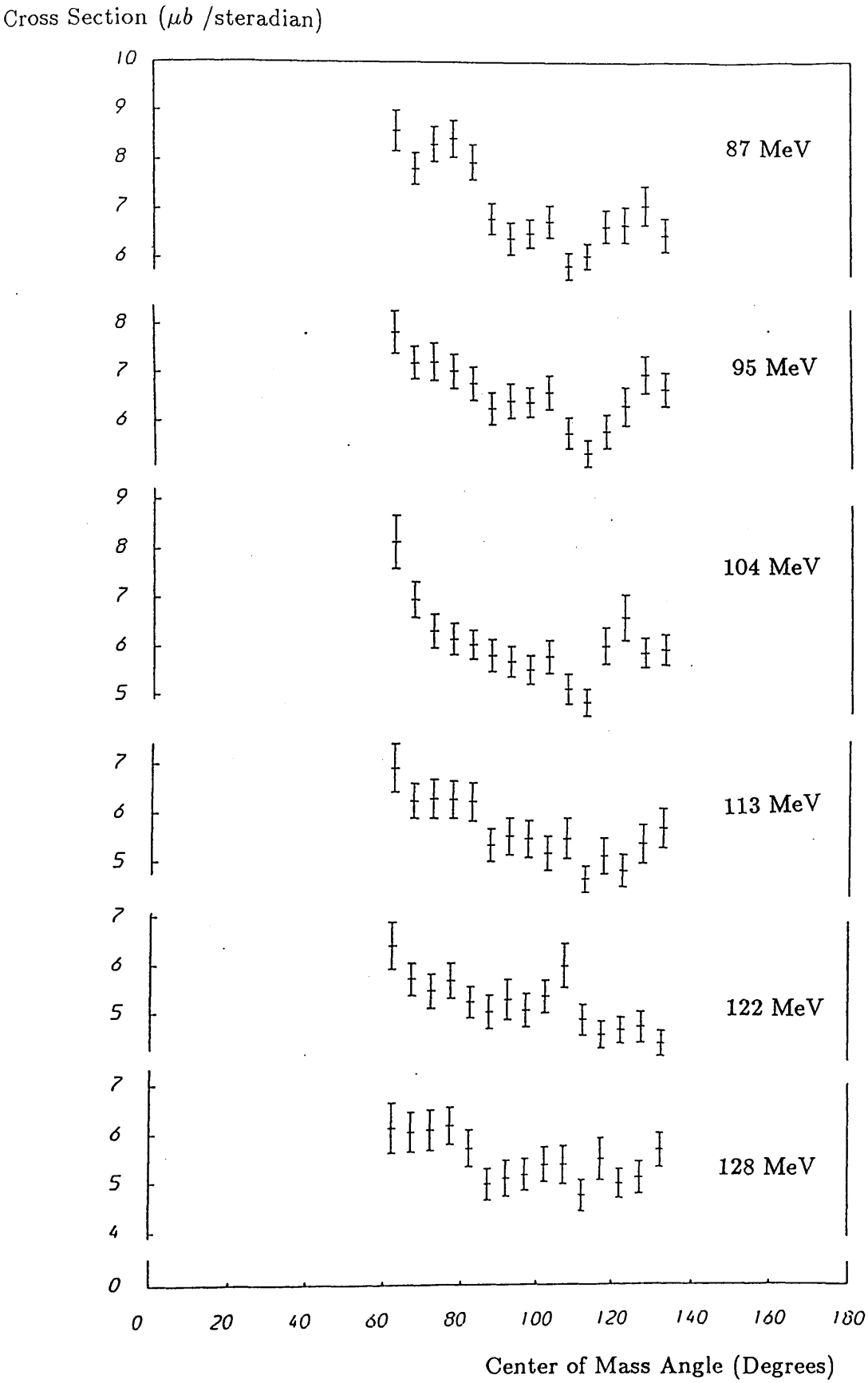

Figure 4.9 The measured differential cross section for the photodisintegration of the deuteron, for a photon energies of 87, 95, 104, 113, 122 and 128 MeV.

Chapter 5

Interpretation of Results

5.1 Deuteron Photodisintegration Theory

5.1.1 Classical Calculation

In the mid sixties, one of the first comprehensive investigations into the photodisintegration of the deuteron was performed by Partovi[31].

The treatment by Partovi was performed using the non-relativistic Shrödinger theory, to calculate the deuteron and continuum wave functions. Nucleons in this case were assumed to interact through the semi-phenomenological nuclear potential developed by Hamada[32]. The Hamada potential, which assumes a 7 % D state contribution to the deuteron ground state wave function, was selected as it provided the best fit to the contemporary electron scattering data below 315 MeV. The calculation of the differential cross section for unpolarised incident photons, took final state interactions into account but neglected transitions with multipole terms higher than those due to dipole - octupole interference. This was a reasonable approximation as these higher contributions were shown to be negligible and could not be resolved using contemporary experimental techniques.

One other important development introduced by Partovi was an attempt to include the effect of meson exchange currents into his calculations. At the time meson related effects were thought by some authors to provide a negligible contribution to the cross section. Partovi did not attempt to deal with meson exchange effects explicitly, but instead was able to incorporate meson related effects impilcitly, by using Seigert's[33] theorem.

Since a full description of electromagnetic interactions with nuclei, requires not only one-body charge and current density operators but also the two body operators, the need for which arises specifically from meson exchange effects[42], any theory attempting a comprehensive treatment of the interaction should in principal refer explicitly to two body charge and current distributions. Seigert's theorem, however states that below the meson threshold the electric transition amplitude in the interaction can be represented by a function of the one body charge density operator only. It can be shown[34] that, if conservation of current is applied, two-body currents arising from terms involving the two-body nucleon - nucleon potential and the one body charge distribution are generated. Consequently, Seigert's theorem is a conveinent way of incorporating first order meson exchange effects, in electric transitions in an implicit rather than an explicit way.

The Hamitonian H describing the interaction of an electromagnetic wave with a charge distribution is

$$H = -\int J(x).A(x)dx \tag{5.1}$$

where in the case of deuteron photodisintegration, $A(x)$ is the vector potential operator of the radiation field, and $J(x)$ is the current density operator associated

with the n - p system. Since the uniform motion of the center of mass of the system does not contribute to the current density operator, only currents arising from the internal motion of the n - p system need be considered i.e. from orbital currents and spin currents. This leads to the equation;

$$J^{Internal} = J^{Orbital} + J^{Spin} \tag{5.2}$$

The vector potential A(x) can be expanded in terms of plane waves

$$A(x) = \Omega_N^{-1/2} \sum_{\omega} \sum_{\mu} (2\pi/\omega)^{1/2} (a_{\omega\mu}\epsilon_{\mu} e^{i\omega\cdot\mathbf{x}} - a^*_{\omega\mu}\epsilon_{-\mu} e^{-i\omega\cdot\mathbf{x}}) \tag{5.3}$$

where Ω_N is the normalisation volume,ϵ_μ represents the spherical unit vectors, $a_{\omega\mu}$ the annihilation operator, μ is the photon polarisation, ω the photon momentum and $\epsilon_\mu e^{i\omega\cdot\mathbf{x}}$ can be expanded in terms of electric and magnetic multipoles[31].

The differential cross section of the photodisinegration can be shown to be given by

$$\frac{d\sigma}{d\Omega} = tr(T\rho T^+) \tag{5.4}$$

where T is the transition matrix, a function of the interaction Hamiltonian, and T^+ is its conjugate, and tr is the trace or diagonalised matrix of the inner product. The initial density matrix of the nucleon system is represented by ρ.

The angular distribution derived by Partovi's detailed calculation, for photons of random polarisation and for an unpolarised deuteron target, was of the form

$$\frac{d\sigma}{d\Omega} = a + bsin^2(\theta) + ccos(\theta) + dsin^2(\theta)cos(\theta) + esin^4(\theta) \tag{5.5}$$

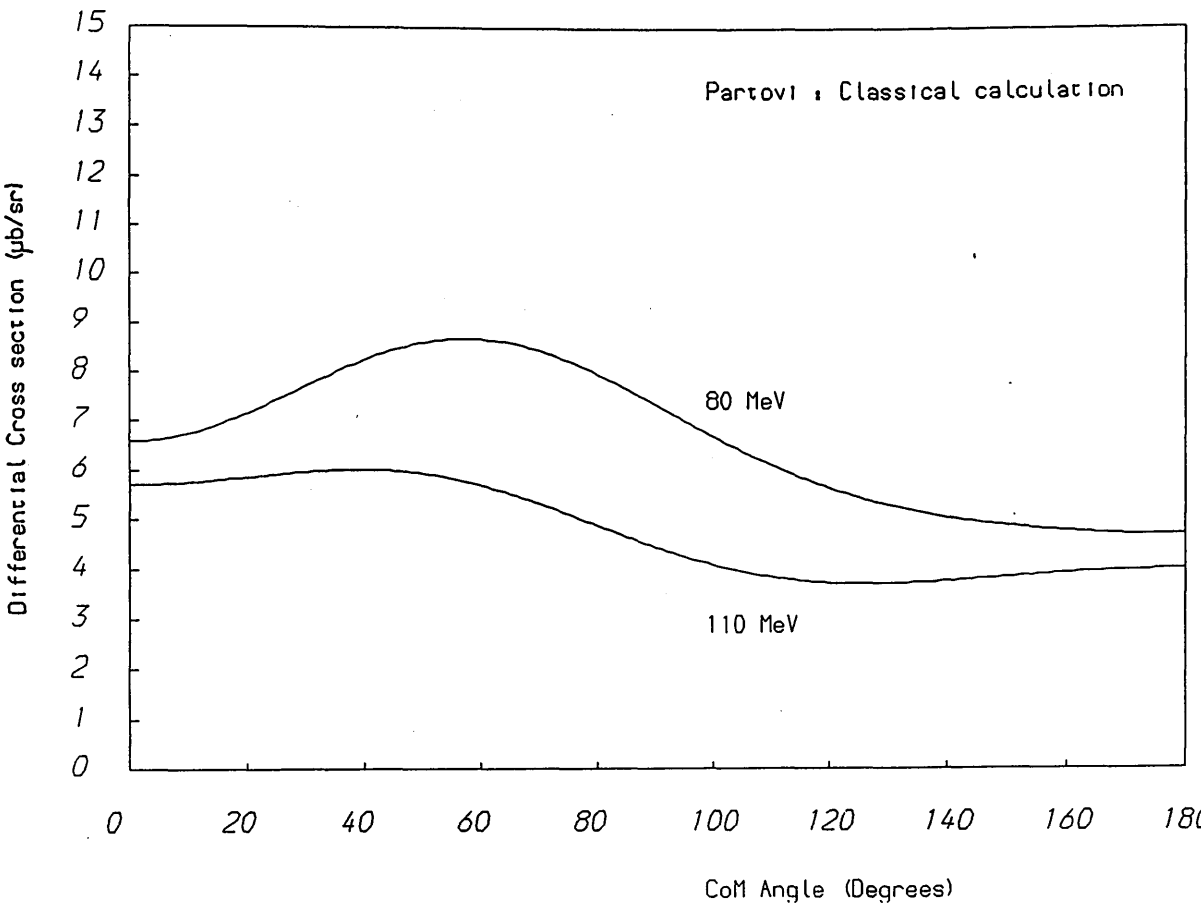

Figure 5.1 The classical calculation by Partovi at photon energies of 80 and 110 MeV.

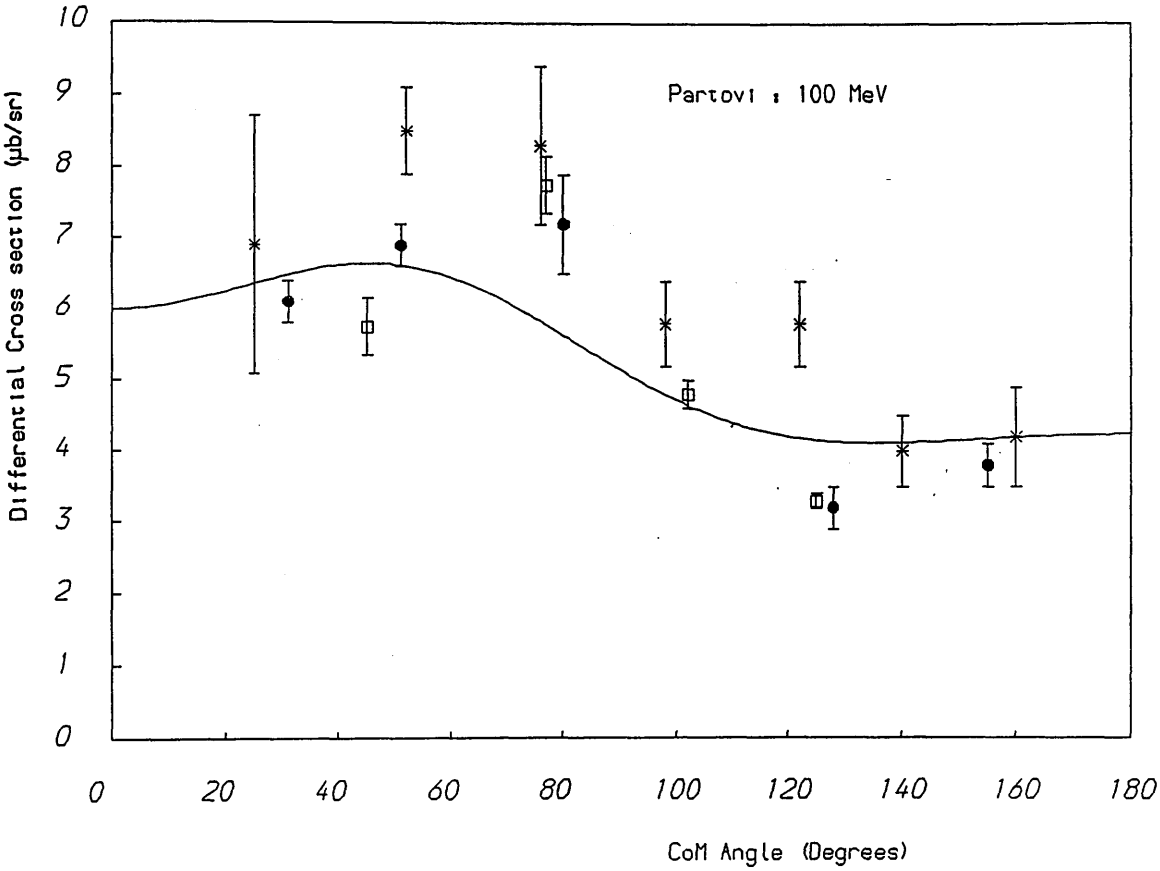

Figure 5.2 Comparision of Partovi's calculation at 100 MeV, with the experimental data of Keck[35] (square), Whalin[36] (dot) and Aleksandrov[37] (star).

In this calculation the vector potential, $A(x)$, is expanded in terms of electric and magnetic multipoles, using rotational matrices.

The differential cross section calculated by Partovi at 80 and 110 MeV is shown in Fig. 5.1 . When compared to the experimental results of Keck[35], Whalin[36], Aleksandrov[37] (as shown in Fig. 5.2) and others[38][39] the calculation of Partovi gives only rough agreement over a wide range of photon energies, the majority of the data being within 10 - 30 % of the calculation. Indeed, the lack of consistency among the different data sets, which is as large as 50 % at certain energies and angles, is clearly indicative of significant systematic errors being present. Some of the many shortcomings of these experiments have been detailed in the recent review paper by Sanzone[40].

When better quality data were obtained, it was found that there were still significant discrepancies with the calculations of Partovi. In particular the measurement at $\theta = 0°$ by Hughes[4] using the Mainz linac which, as will be discussed later, represents a significant improvement in experimental accuracy, should be mentioned.

At forward angles the photodisintegration cross section is particularly sensitive to the magnitude of the D state probability of the deuteron ground state wave function. Using the Hamada potential, which as mentioned previously has a 7% D state probability, Partovi's calculation is 10 % lower at 100 MeV and 45 % lower at 120 MeV than the experimental results of Hughes. However, the necessary modification to the D state probability in the Hamada potential, which brings the theoretical cross section into agreement with the experimental values, produces a D state probability inconsistent with the measured magnetic dipole

and electric quadrupole moments.

In summary therefore, Partovi's calculation can only provide rough agreement with experiment in the angular range $\theta = 20° - 160°$, and is unable to reproduce experimental data outwith this region.

5.1.2 Meson Exchange and Isobar Effects

The importance of meson exchange currents in the deuteron was first appreciated in the mid 1960's[41] in the course of analysing deuteron radiative capture data. It was found that discrepancies could only be explained by assuming the existence of large meson exchange effects for the deuteron.

As we have seen from the treatment of Partovi, first order meson exchange effects, arising from electric transitions are implicitly taken into account by use of Seigert's theorem. However a more thorough investigation of these effects by Arenhövel[42] highlights the areas where Seigert's theorem alone is insufficient.

Using the Reid soft core as the nuclear potential, Arenhövel performed calculations,to show the effects meson exchange currents (MEC) have on both electric and magnetic multipole transition strengths. The results of these calculations, which are presented in Fig. 5.3 from reference[42], show that the meson exchange effects are quite substantial, especially at higher energies near the meson threshold. The current density operator adopted by Arenhövel can be written in terms of one-body and two-body contributions

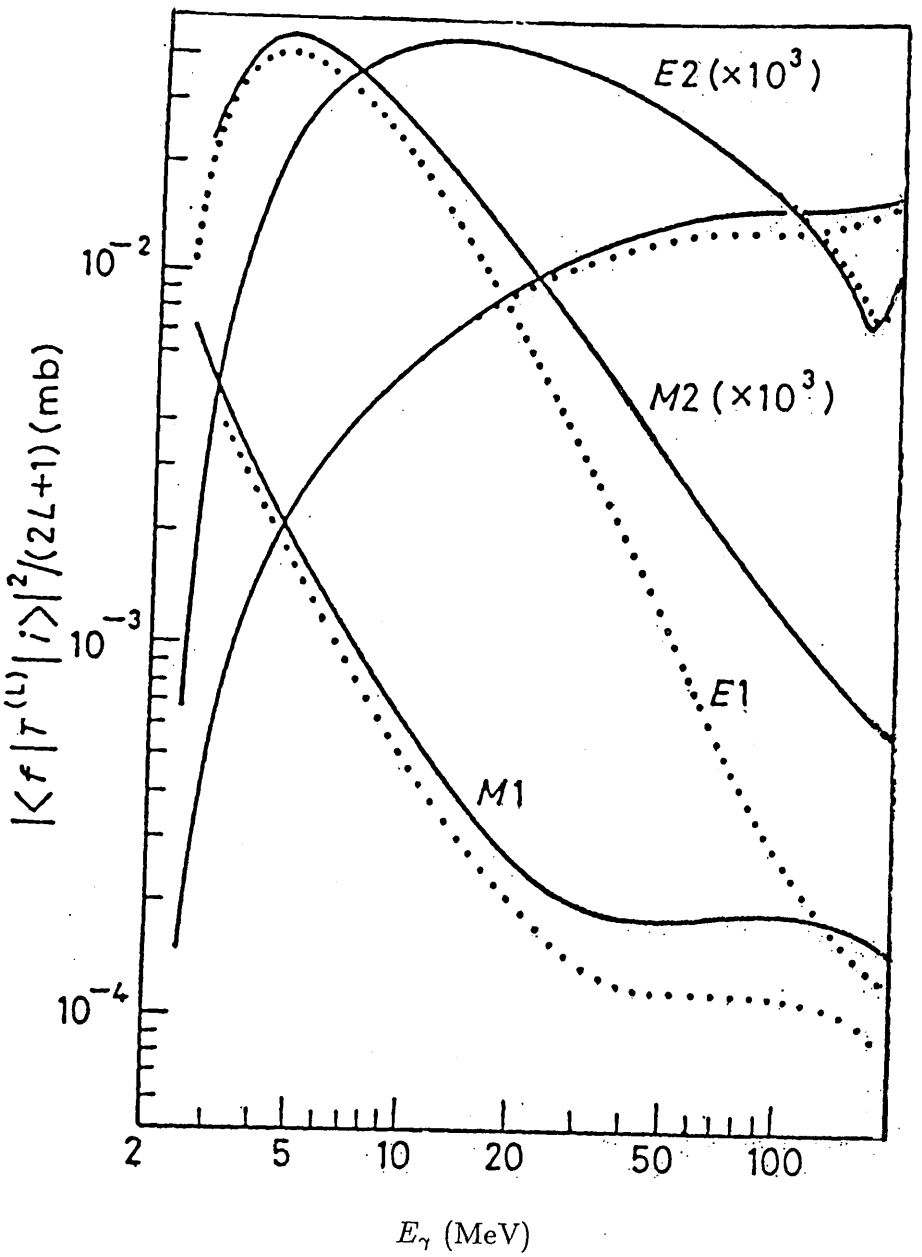

Figure 5.3 Computation by Arenhövel showing multipole transition strengths for deuteron photodisintegration with one-body effects only (dotted line) and with one and two-body effects (full line).

$$J = J_{[1]} + J_{[2]}^{MEC} \tag{5.6}$$

As we have already seen, some two-body contributions are generated by the use of the Seigert theorem, and Fig. 5.4 again from reference[42], shows the effect on the total cross section of the inclusion of meson effects using the Seigert theorem and also using explicit exchange terms. Arenhövel found that additional explicit corrections beyond the Seigert operator, only became significant near the pion threshold. In fact it was found that with the exception of M1 transitions, which need only small corrections, higher multipole transitions are little affected. The MEC calculation by Arenhövel is shown in Fig. 5.5 for photon energies of 80 and 110 MeV.

When all of the two-body meson effects are taken into account, an increase in the differential cross section is observed. This is illustrated in Fig. 5.6, where the theoretical calculations of Partovi and Arenhövel[43] are compared with the experimental data of Hughes[4], Kose[44], Dougan[45] and Whalin[36] at 100 MeV photon energy. Since, the data sets shown in Fig. 5.6 are in such poor agreement, it is impossible to say anything definite about the relative merits of the theoretical calculations. However, it is noticeable that the Arenhövel cross section is in poorer agreement with the zero degree result of Hughes *et al* than the Partovi calculation.

Particle physics has shown that nucleons have a complicated internal structure, which is exhibited in the form of excited nucleon states. These states are called resonances or isobars[46], the excitation energies of these states being in the region of several hundred MeV. Because of the large excitation energies of these

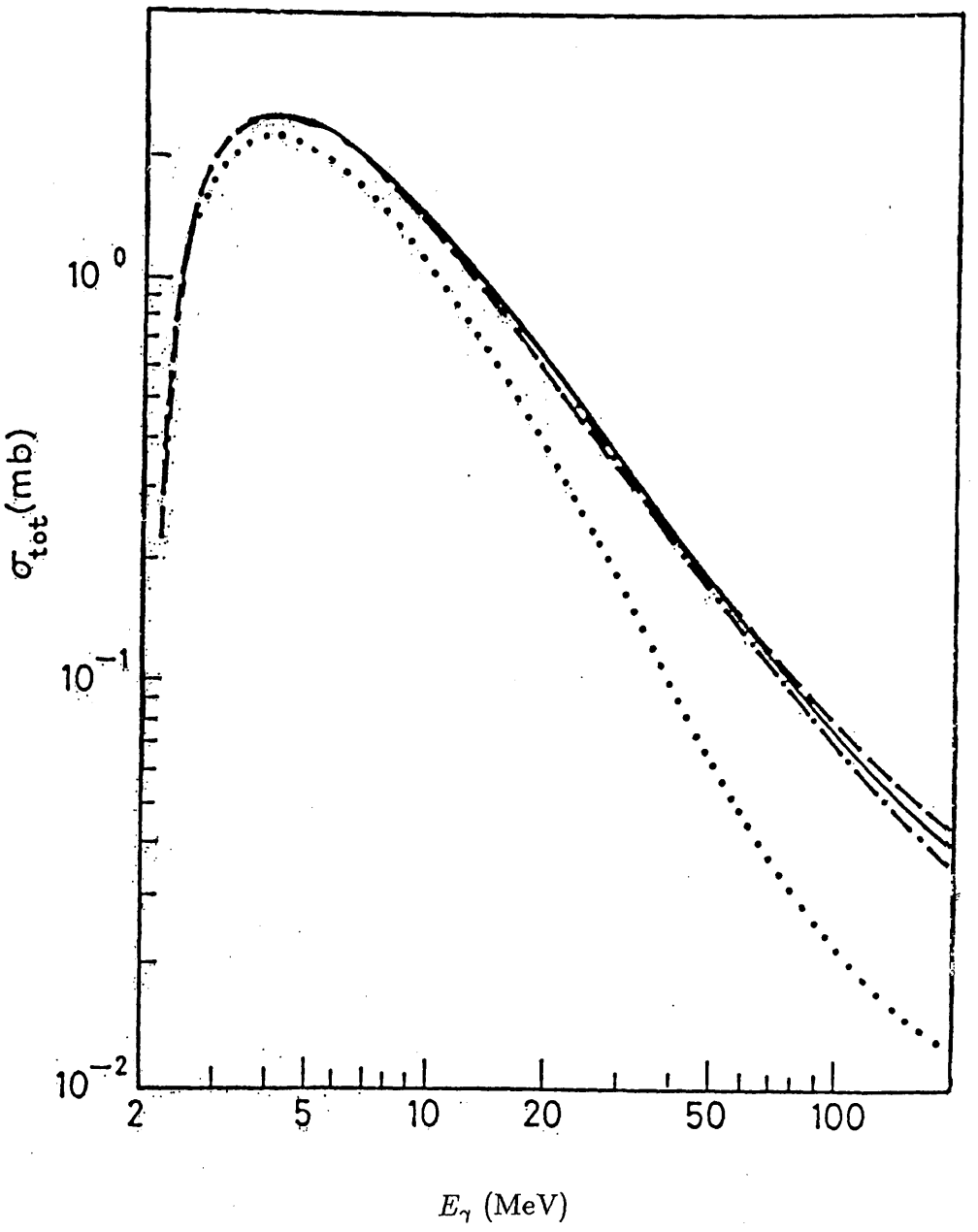

Figure 5.4 Computation by Arenhövel showing the deuteron photodisintegration total cross section, calculated using one and two-body effects (full line), Seigert approximation with (dash dot line) and without (dash line) second order corrections. Again the dotted line shows a calculation with one-body effects only.

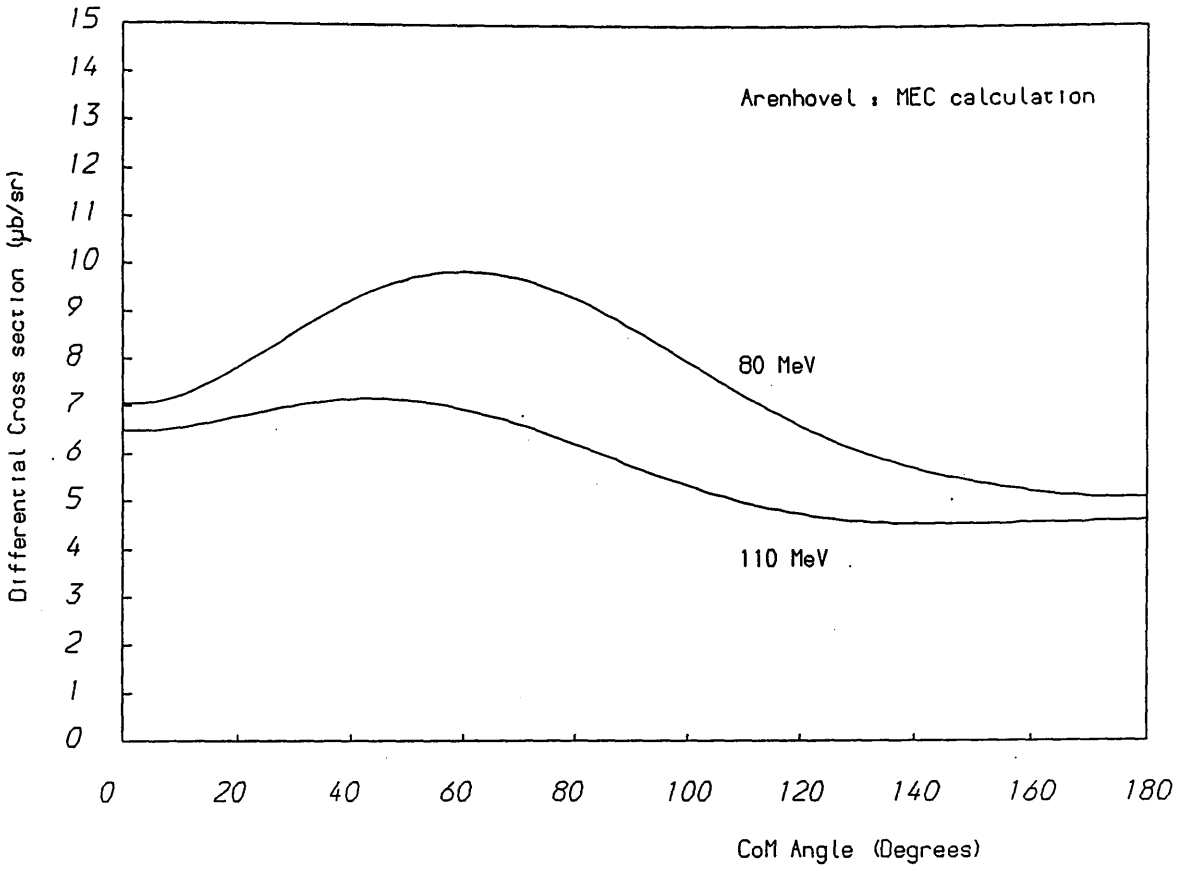

Figure 5.5 A calculation by Arenhövel which includes explicit MEC effects not included by using the Seigert theorem, at photon energies of 80 and 110 MeV.

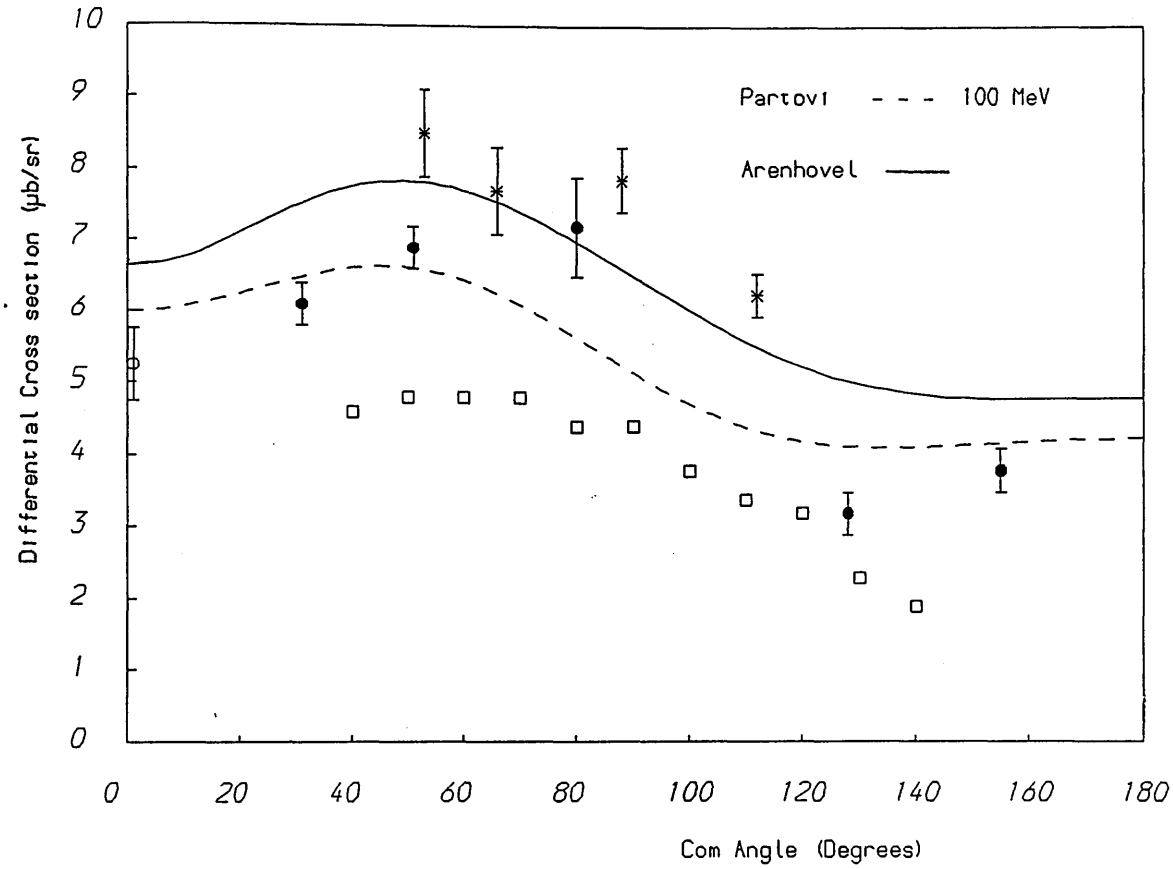

Figure 5.6 Comparison of the classical calculation (Partovi - dashed line) and a calculation which explicitly includes meson effects (Arenhövel - solid line) , for the differential cross section at 100 MeV. The experimental data of Hughes[4] (open circle), Dougan[45] (star), Kose[44] (square) and Whalin[36] (dot) are also shown.

states, in comparison with the rather weakly bound nucleons in the deuteron, they are usually neglected.

To investigate the validity of neglecting isobar effects, Arenhövel has performed calculations which show the effects of these isobar configurations (IC) on the deuteron photodisintegration differential cross section. Fig. 5.7 shows a comparison of the calculation in which meson effects are explicitly dealt with, and a calculation which additionally includes the isobar effects: again the photon energies are 80 and 110 MeV. We can see from Fig. 5.7 that there is a rise in the differential cross section due to the inclusion of the isobar configurations, and that although small the effect is not negligible. Furthermore, the 0° cross section now differs from the value obtained by Hughes by aproximately 30 % .

5.1.3 Relativistic Effects

The preceding sections, have discussed the most important terms in the transition amplitude for the photodisintegration of the deuteron. The large discrepancies of 30 % or more between the calculated and experimental cross section at 0° indicate that further refinements are required. Attempts have been made by Greben[47] to resolve the differences by modification of the nuclear potentials used. However, minimal changes to the calculated cross sections were found in the intermediate energy range.

All calculations discussed so far have been carried out within a non-relativistic framework and only local contributions of the two-body current and charge densi-

ties have been included. These shortcomings were circumvented in the treatment by Pandey and Rustigi[48] which includes relativistic corrections to the one-body charge density and the two-body current and charge density, with local and non-local contributions. The calculation also takes into account the final state interaction between neutron and proton. However the only transitions considered were those induced by the multipoles E1, E2 and M2. In essence this was the calculation of Rustigi[49] some 20 years earlier, with the relativistic correction to the interaction Hamiltonian being taken into account. In addition to this, calculations were performed for several well known nuclear potentials, to observe variations between the various potentials. Interestingly, Pandey found that of the nucleon - nucleon potentials considered, those of Hamada, Yale and Reid soft core, provided little differences to the differential cross section, confirming the findings of Greben[47].

The calculation of Pandey and Rustigi at the photon energies of 80 and 110 MeV, is shown in Fig. 5.8 . There are several distinct differences with the previous theories considered, and a comparision of Fig. 5.7 and 5.8 shows that a relativistic treatment affects not only the magnitude of the cross section but also the shape of the angular distribution.

Calculations in a relativistic framework are also being performed by Cambi[50][51] which as yet are unpublished in complete detail, but show some differences from the Pandey and Rustigi calculation, especially at forward and backward angles. When both of these theories are compared to the 0° results of Hughes, the values from Pandey and Rustigi are too low, but the results of Cambi provide better agreement. Fig. 5.9 shows a comparison of the Pandey and Cambi calcula-

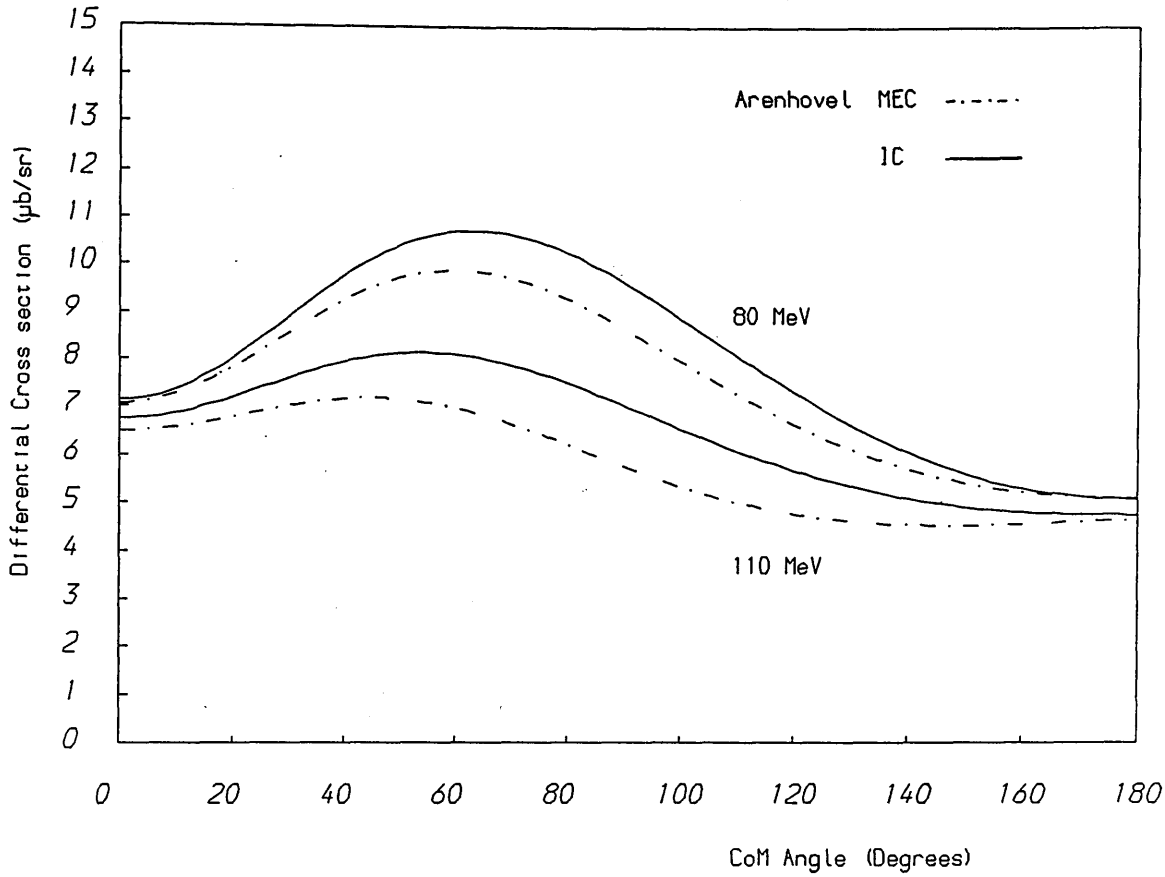

Figure 5.7 Shows the effect of the addition of isobar configurations to the differential cross section at 80 and 110 MeV. The dot dash line is calculated using explicit MEC effects, the solid line shows the addition of IC effects to this.

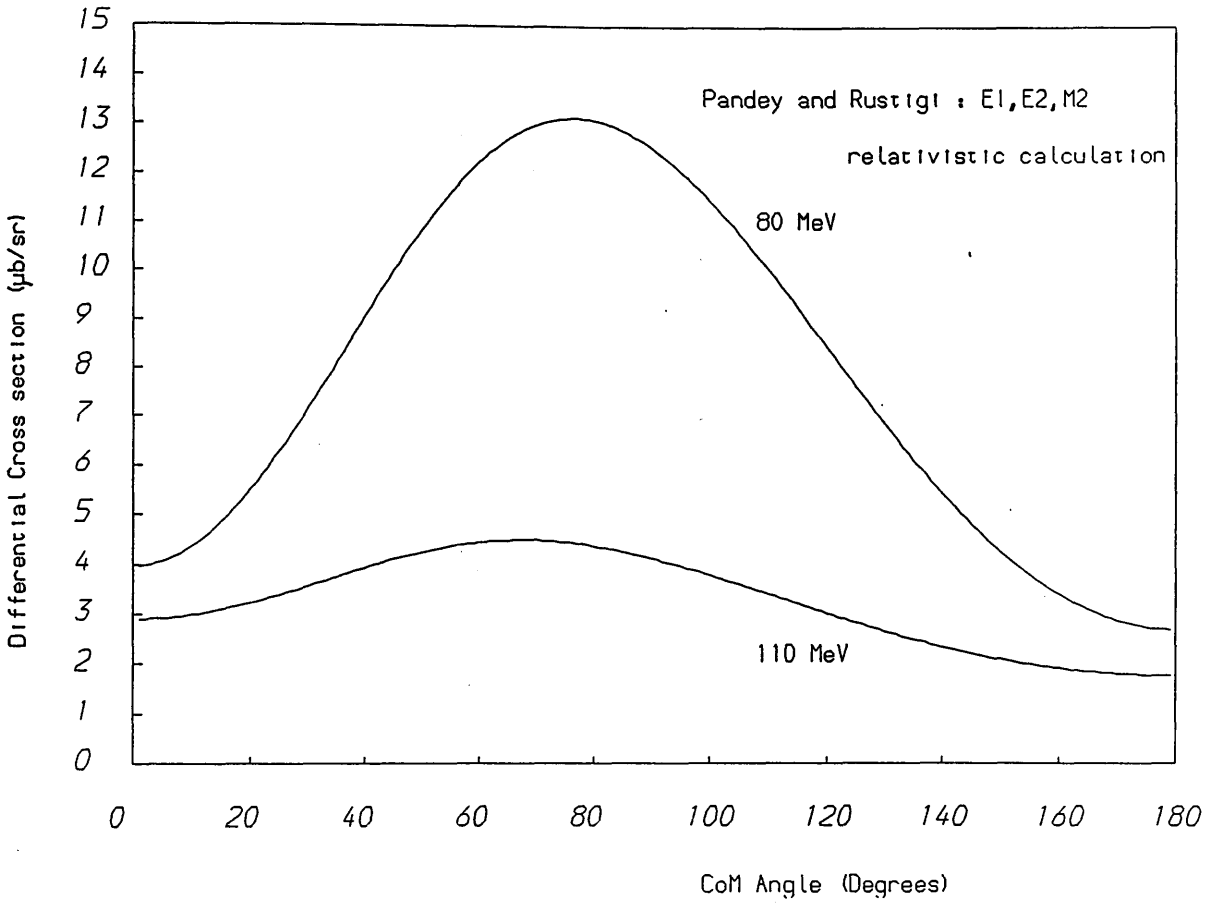

Figure 5.8 The calculation by Pandey and Rustigi which includes relativistic corrections to the differential cross section, at photon energies of 80 and 110 MeV.

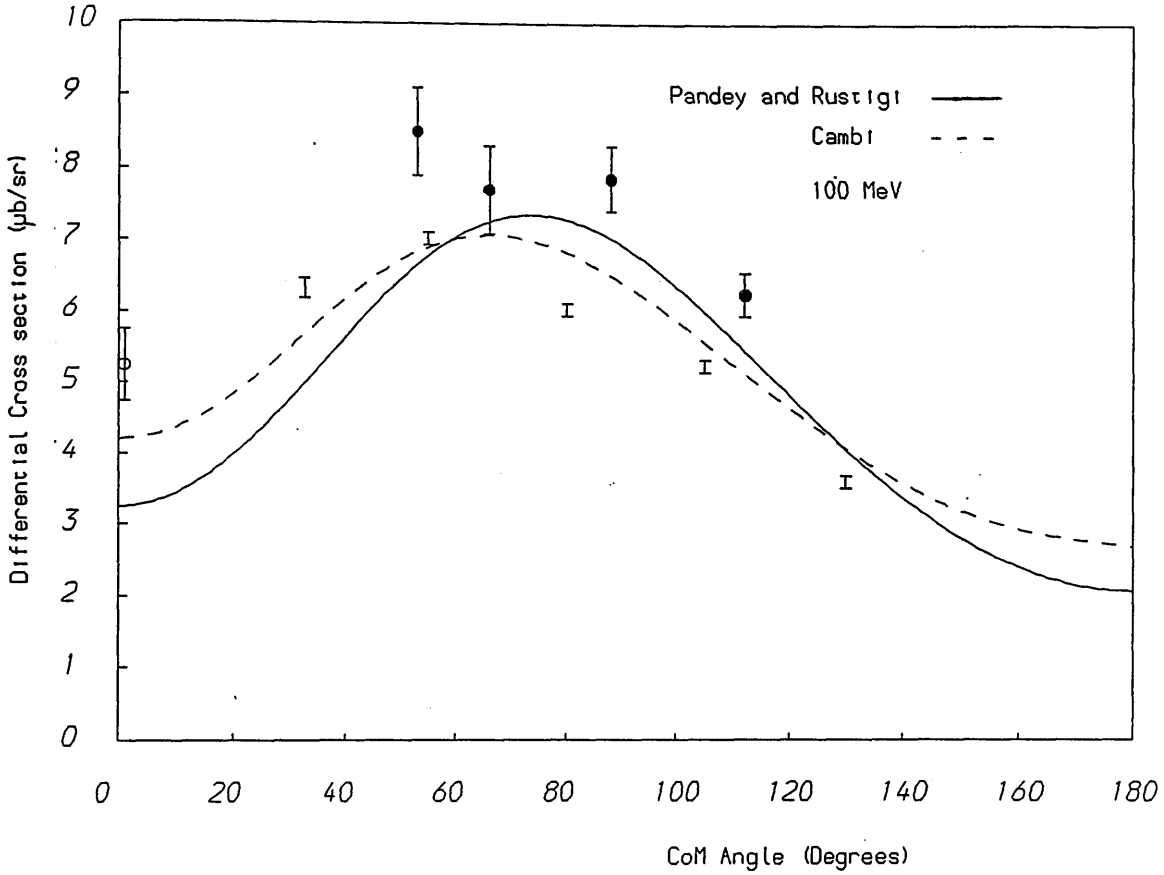

Figure 5.9 The comparison of the calculations by Pandey and Rustigi, and Cambi at 100 MeV, with the experimental data of Hughes[4] (open circle), Dougan[45] (dot) and De Sanctis[52] (no symbol).

tions at 100 MeV with the experimental data of Hughes[4], Dougan[45] and De Sanctis[52].

The preceding sections have briefly described some of the major theoretical treatments of deuteron photodisintegration. Fig. 5.10 shows the calculations of Pandey and Rustigi, Arenhövel and Partovi at 100 MeV photon energy. There are differences in the shape and in the magnitude of the cross section between these theories. However, the general poor quality of the available experimental data has made it impossible to identify which theory provides the best explanation of deuteron photodisintegration in the intermediate energy range.

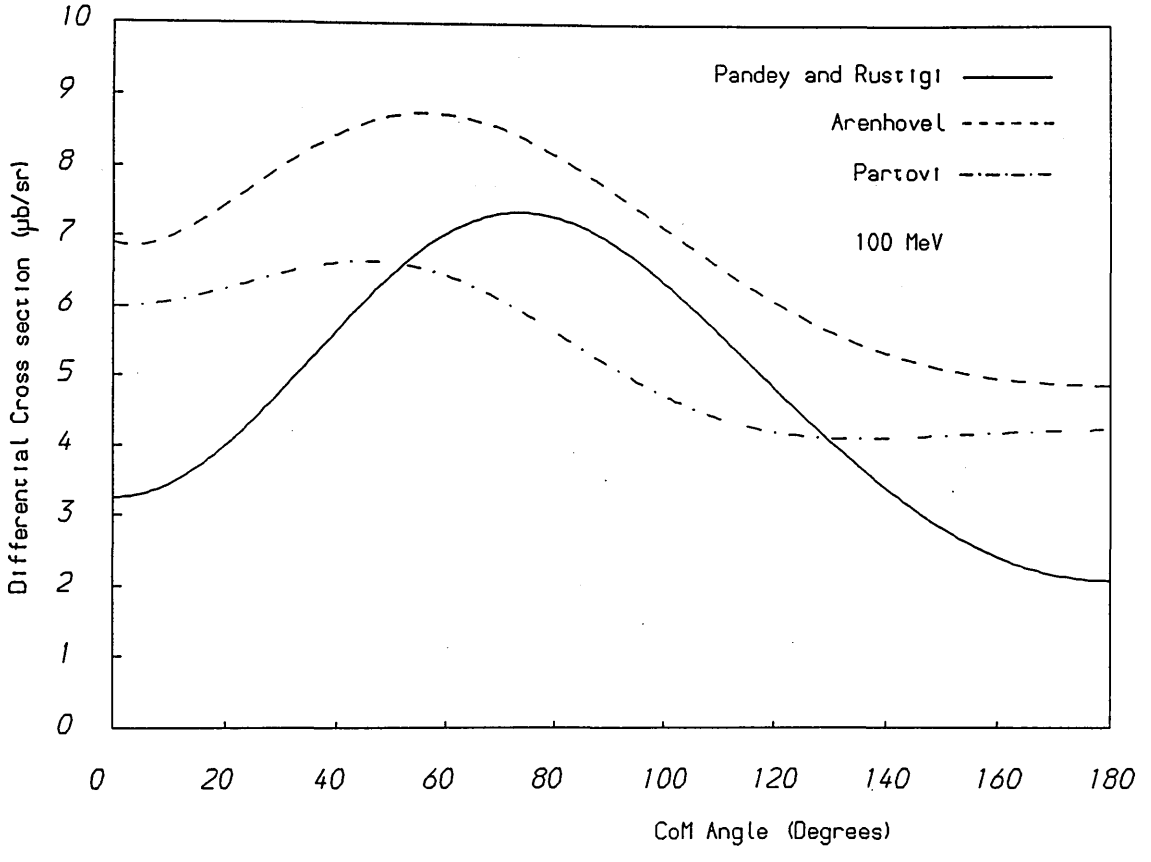

Figure 5.10 Comparison of the calculations considered in this section at 100 MeV; Pandey and Rustigi[48] calculation with relativistic corrections (solid line), Arenhövel[42] MEC + IC calculation (dashed line) and the classical calculation of Partovi[31] (dot dash line).

5.2 Comparison of the present measurement with previous experimental data

As has been previously indicated many experiments have been performed on the photodisintegration of the deuteron, since the first observation of the process in 1934[53]. Most of these experiments have been conducted with incident photon energies of 80 MeV or less. However in the intermediate energy range of 80 MeV to the pion threshold, large discrepancies of upto 40 % exist among the data. The discrepancies arise from difficulties incurred using deuteron targets, and the problems associated with obtaining absolute values of detector efficiencies and knowing the absolute value of the incident photon flux. Probably the most important of these factors is the determination of the photon flux, as it is unlikely the other factors should produce sufficiently large effects to account for the large discrepancies found. Consideration of these factors leads one to divide the available data into two distinct groups; those experiments which rely upon a knowledge of the incident photon flux, as described by theoretical calculations of the bremsstrahlung spectrum, to calculate the cross section, and those experiments which determine the photon flux directly or dispense with the need to know the magnitude of the incident flux.

Experimental data produced in the 1950's and 1960's in the intermediate energy range were accumulated using a wide variety of experimental techniques. Whalin at Illinois[36] employed a 300 MeV betatron to produce high energy photons which were then incident on a liquid deuterium target, detection of the resultant photoprotons being performed using nuclear emulsions. Aleksandrov

from the Lebdev institute[37], used a 265 MeV synchrotron to enable the production of a bremsstrahlung beam directed at a heavy water target. Detection of the outgoing protons was accomplished using shielded proportional counters.

Figs. 5.11 (a) and (b) show examples of data which rely on bremsstrahlung formulae for evaluation of the cross section, at the incident photon energies of 100 and 120 MeV respectively. Although the angular distribution could be said to show broadly the same shape, the absolute values of the cross section show a considerable spread, which is outwith the experimental errors quoted. The conclusion must be that the reason for such a variation is due to a lack of knowledge of the incident photon flux.

More recently experiments have been performed which do not depend upon any absolute knowledge of the bremsstrahlung cross section. These are experiments which employ quasi monoenergetic photon sources, such as those produced by *tagging* techniques, or avoid requiring a knowledge of the incident photon flux such as in comparison techniques. Figs. 5.12 (a) and (b) show experimental data produced from experiments which employ these methods, as well as results from the present experiment, again at the photon energies of 100 and 120 MeV. Although few experiments of this type have as yet been performed the data agree within the quoted errors.

From these comparisons we can conclude that at present experiments which are not dependent on bremsstrahlung calculations, have a greater level of agreement than those which are dependent upon bremsstrahlung calculations. A recent review of deuteron photodisintegration experiments by Sanzone[40] highlighted the dangers of relying on bremsstrahlung calculations. She concluded

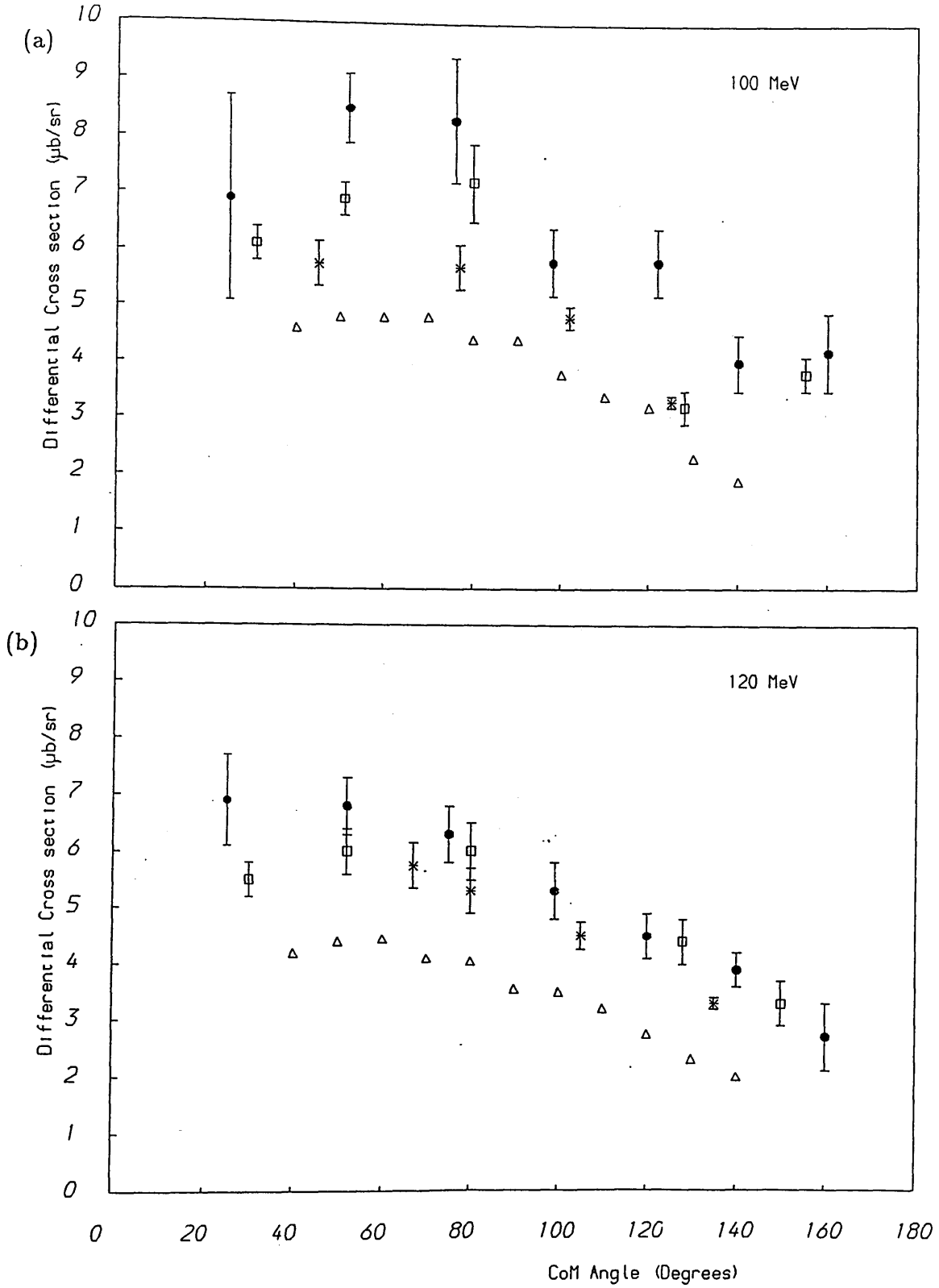

Figure 5.11 Deuteron photodisintegration data produced using bremsstrahlung formulae to determine the photon flux; Keck[35] (square), Whalin[36] (dot), Aleksandrov[37] (star) and Kose[44] (triangle). (a) at 100 MeV (b) at 120 MeV

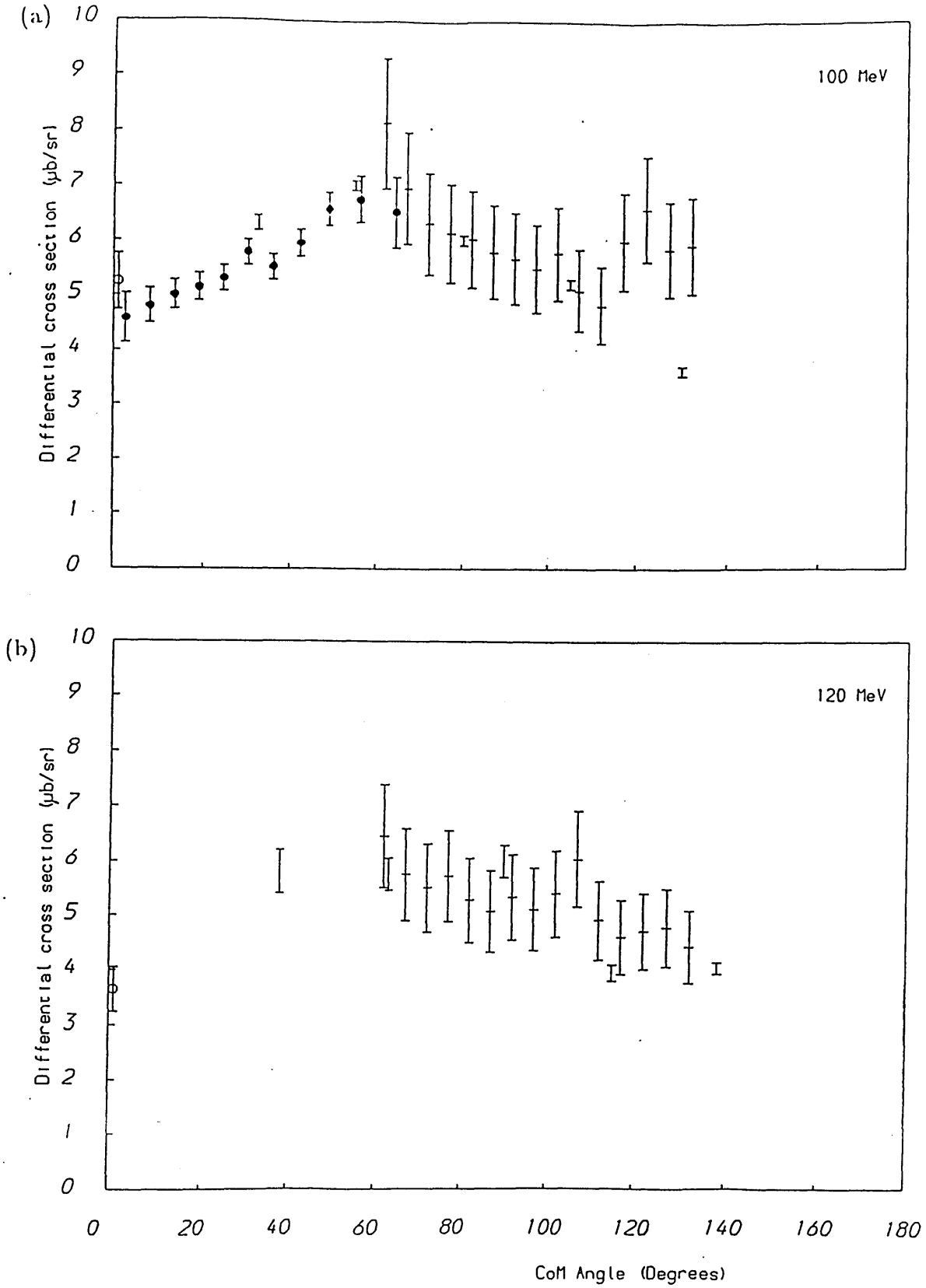

Figure 5.12 Deuteron photodisintegration data produced using methods not dependent of bremsstrahlung calculations; Hughes[4] (open circle), Meyer[54] (dot), De Sanctis[52] (no symbol) and the data from this experiment (cross). (a) at 100 MeV (b) at 120 MeV

that the bremsstrahlung spectrum varies rapidly with the photon emission angle at forward angles, and that calculations using the various formulae[3] produce bremsstrahlung yields which can differ by as much as 10 to 20 % . Consequently at present *tagging* techniques offer the most reliable approach for measuring photo-induced cross sections.

In the present experiment the data were accumulated simultaneously over a large range of incident photon energies and photoproton emission angles, which not only reduced the runtimes, but also meant that angle to angle and energy to energy normalisations were avoided. Since this was the first measurement carried out using the Mainz *tagging* system, the uncertainty in the *tagging* efficiency of the spectrometer was around 10 % . More recent measurements of the efficiency show that it can be determined to approximately 1 % , but even with an uncertainty of 10 % the present measurement represents a significant improvement over previous measurements.

5.3 Comparison of the present measurement with Theory

In this section, several of the theoretical calculations discussed will be compared with the results presented in this thesis. The theoretical calculations cover many aspects of the processes which describe the photodisintegration of the deuteron, namely;

- the effects of purely electromagnetic transitions.
- final state interactions.
- meson exchange effects.
- isobar configurations.
- relativistic effects.

The previous section highlighted the differences in the reported experimental results, and showed that the differences in the older data are outwith the experimental errors quoted. Theoretically, although the general features of the differential cross section can be described, the inclusion of the refinements listed above has lead to a divergence of calculated values similar in extent to those produced by experiment.

The calculation of Partovi[31] is shown in Fig. 5.13 (a) to (f), at the photon energies of the presented data 87, 95, 104, 113, 122 and 128 MeV. Here, there is no consistent agreement between theory and the results of this thesis, with the calculation consistently below the data. The shape of the differential cross section

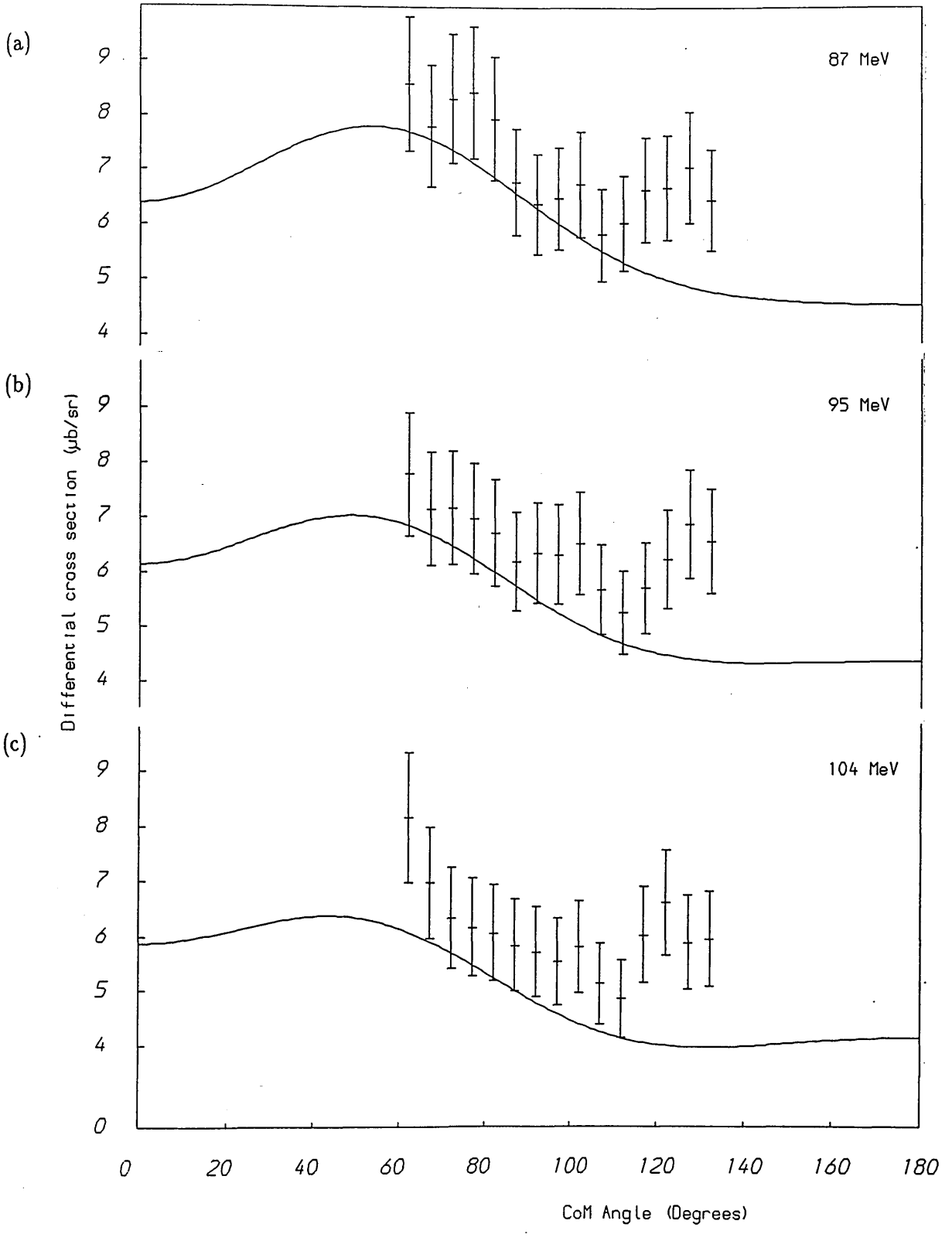

Figure 5.13 A comparison of the presented data at (a) 87 MeV, (b) 95 MeV and (c) 104 MeV with the theoretical calculation by Partovi[31].

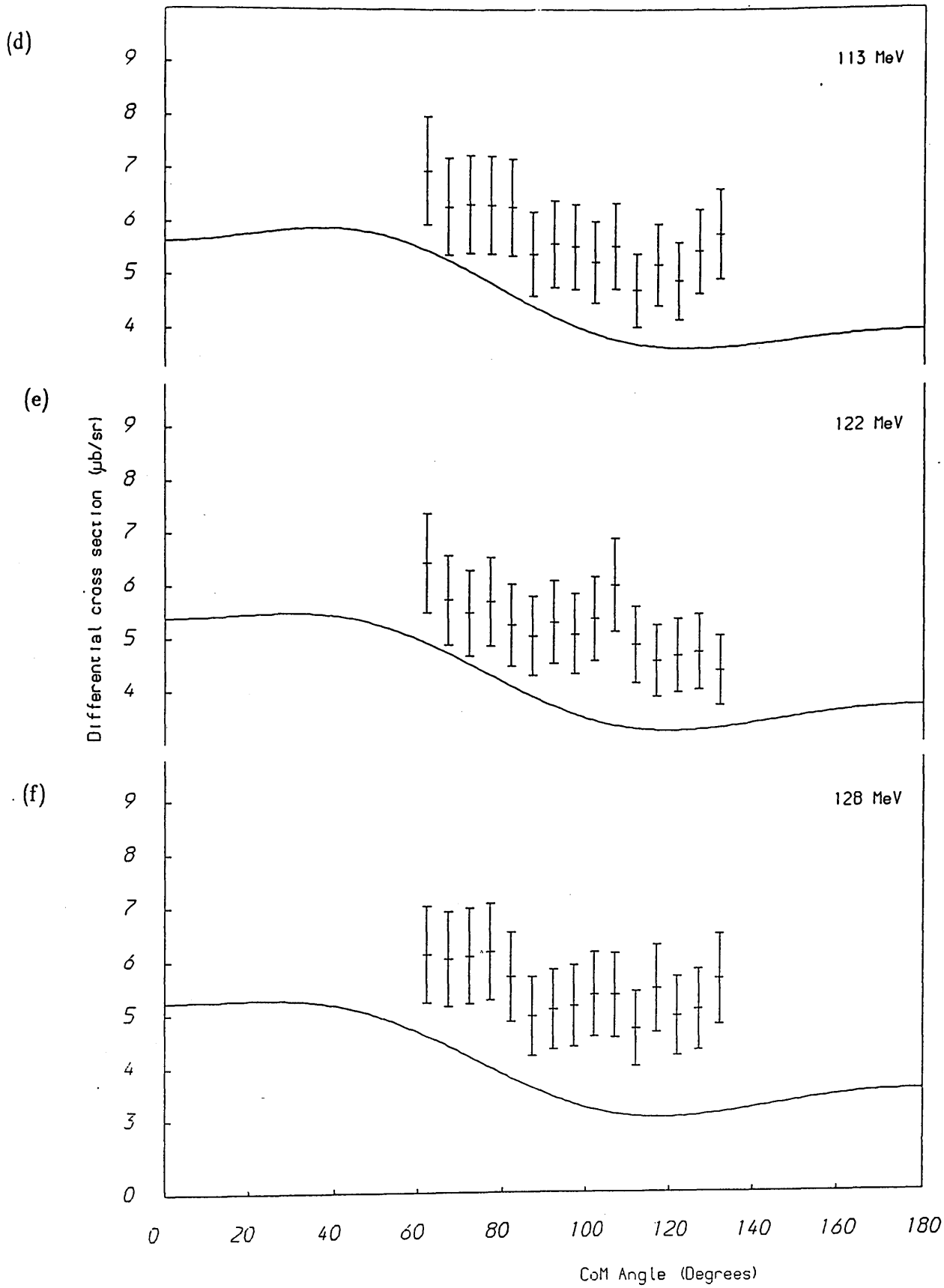

Figure 5.13 A comparison of the presented data at (d) 113 MeV, (e) 122 MeV and (f) 128 MeV with the theoretical calculation by Partovi[31].

is broadly similar, but does not lie within the experimental errors. However the importance of meson exchange effects on the cross section is confirmed as the theory is of the same magnitude as the data.

Figs. 5.14 (a) to (c) show the calculation of Arenhövel which takes all contributions of meson exchange into account, compared with the presented data at photon energies of 90, 100 and 110 MeV. The results of this experiment are in general agreement with the calculation. When contributions due to isobar configurations are included shown in Figs. 5.15 (a) to (c), the magnitude of the differential cross section is again increased, and the shape of the cross section modified. This results in the experimental points lying just below the calculation.

The recent calculation by Pandey and Rustigi produces values substantially different from the experimental results presented. The theoretical calculations are compared with the present data at the energies of 87, 95, 104 and 113 MeV, and are shown in Figs. 5.16 (a) to (d). At energies below 100 MeV, the theory shows a sharp rise in the cross section reaching a maxima at around 75 °, a feature not evident in the data. At higher photon energies the calculation is too low, lying well below the data.

Of the theoretical calculations which are presented, the Arenhövel calculation which includes explicit meson exchange effects but not isobar excitation seems to give the best agreement with the existing data. It should be noted however, that the calculations of Arenhövel do not include relativistic corrections to the interaction Hamiltonian and in that sense are incomplete.

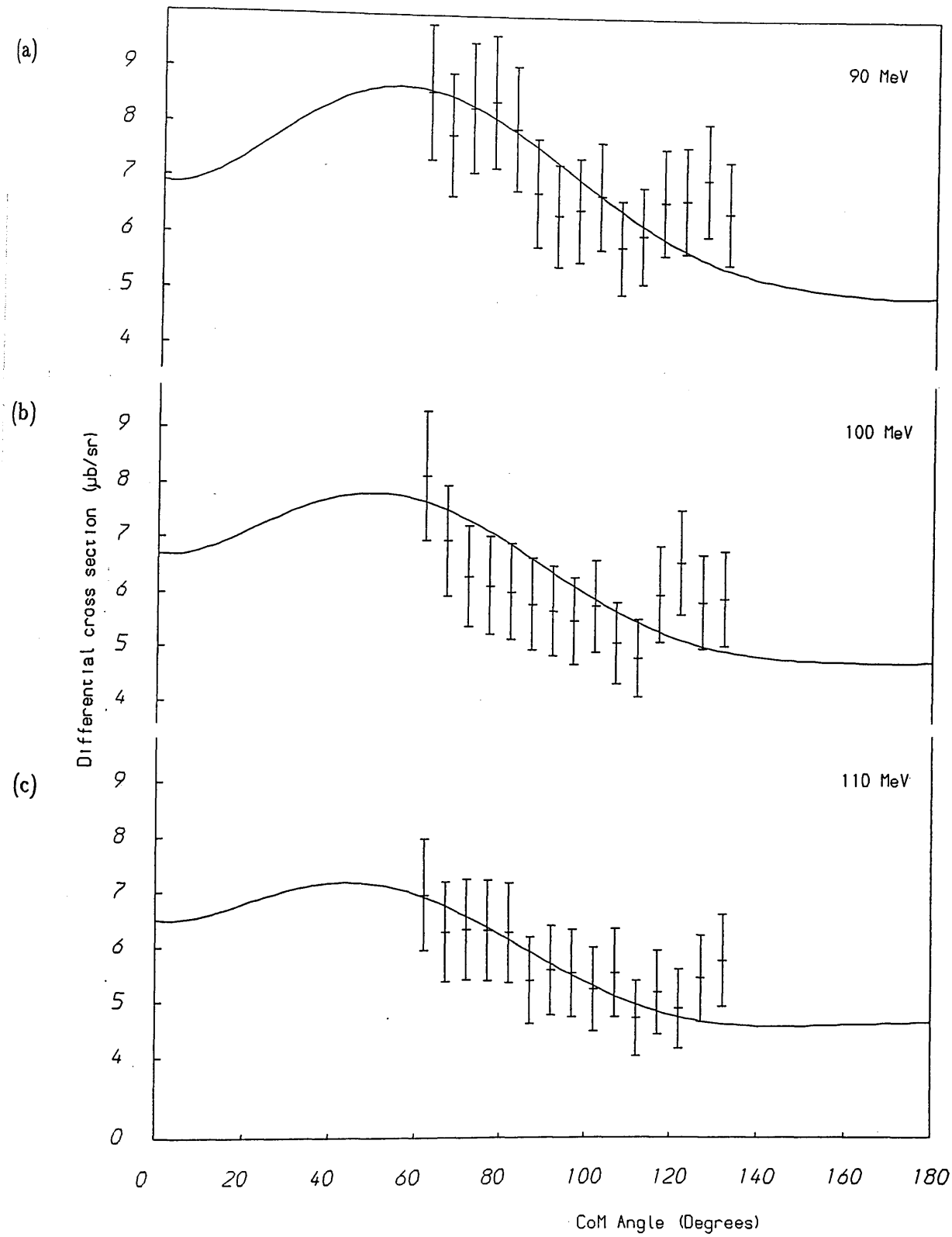

Figure 5.14 A comparison of the presented data at (a) 90 MeV, (b) 100 MeV and (c) 110 MeV with the theoretical calculation by Arenhövel[42], which takes all contributions of meson exchange effects into account.

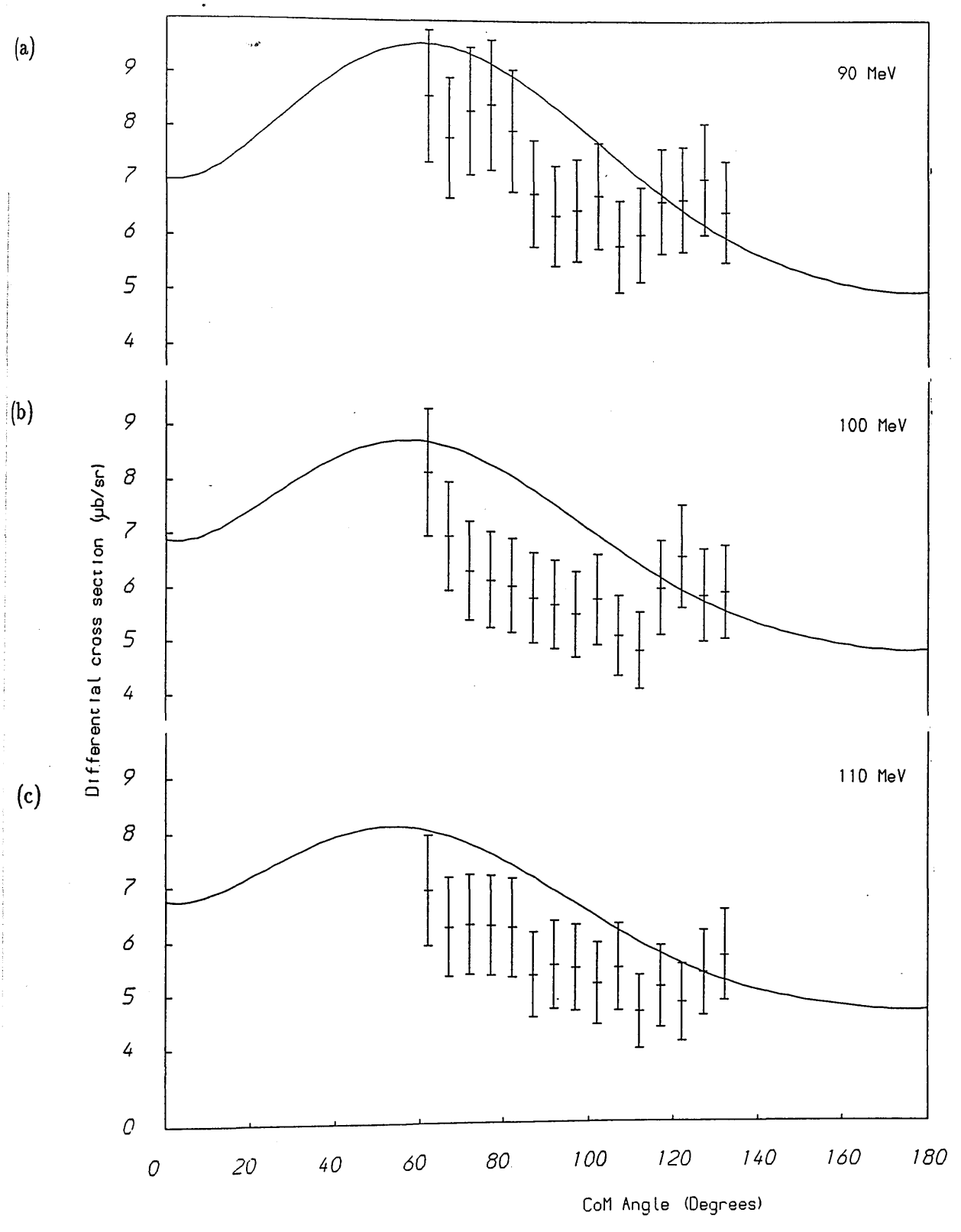

Figure 5.15 A comparison of the presented data at (a) 90 MeV, (b) 100 MeV and (c) 110 MeV with the theoretical calculation by Arenhövel[43], which in addition to including all contributions of meson exchange effects, includes contributions to the cross section attributable to isobar configurations.

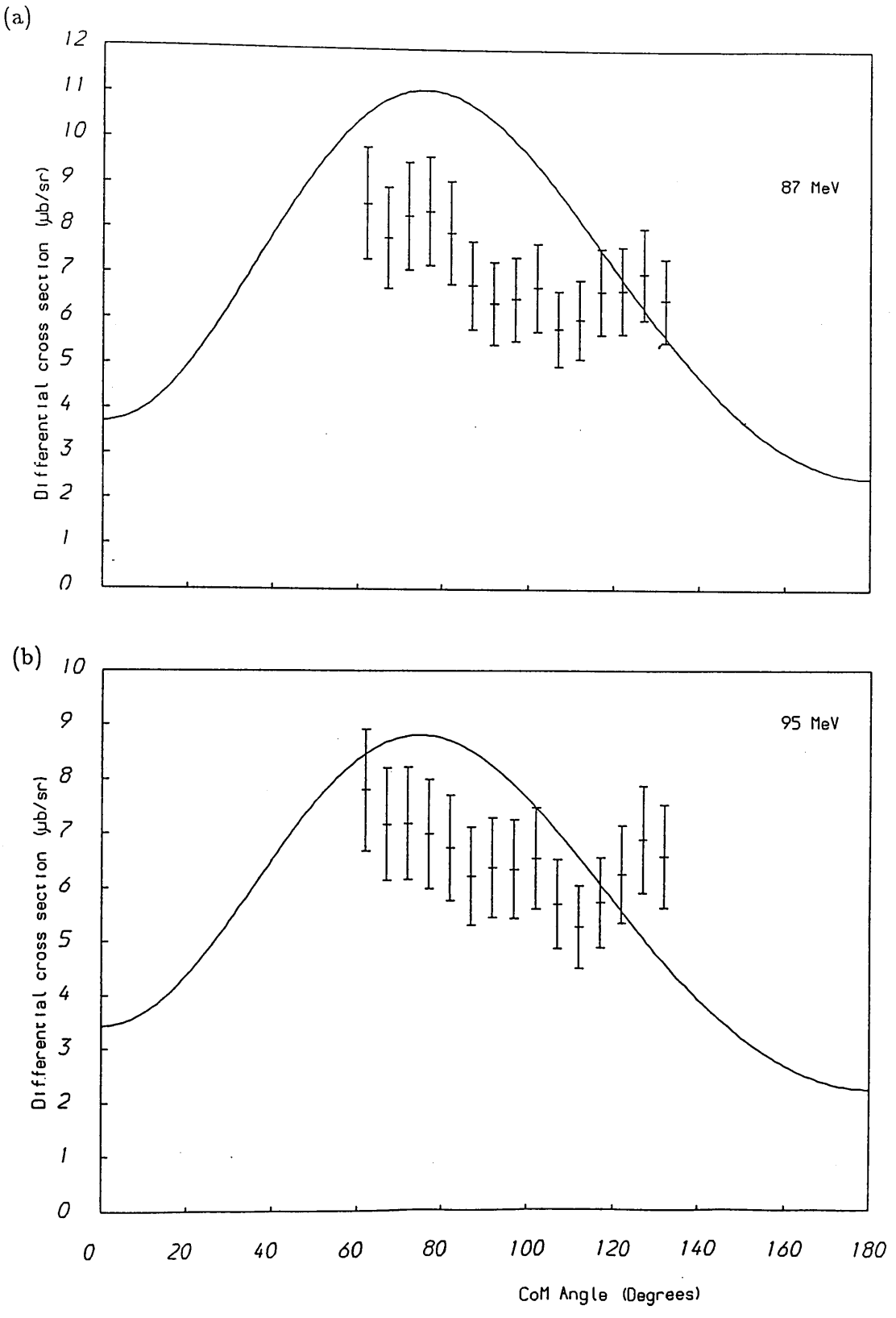

Figure 5.16 A comparison of the presented data at (a) 87 MeV and (b) 95 MeV, with the theoretical calculation by Pandey and Rustigi[48], which includes relativistic corrections to the interaction Hamiltonian.

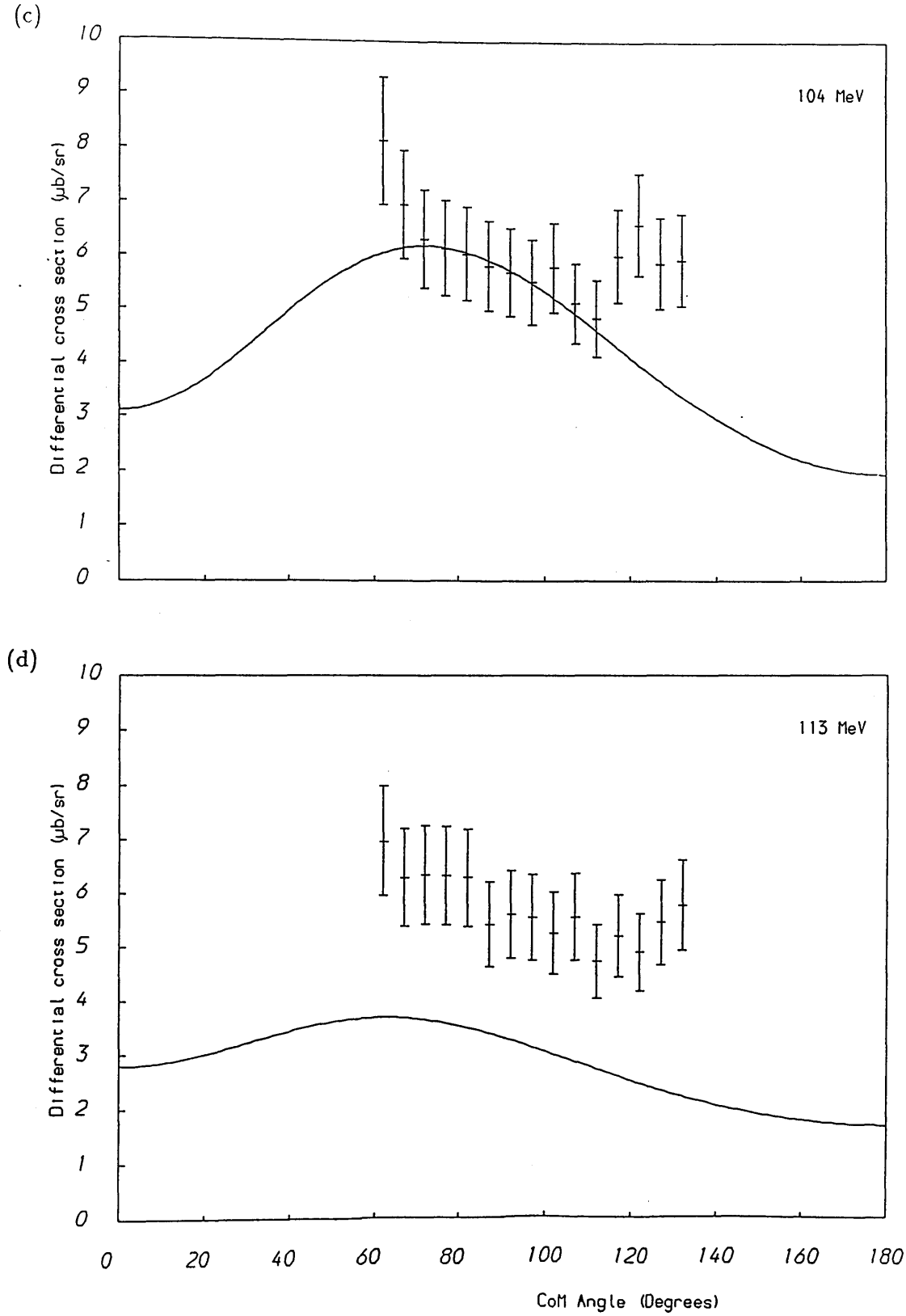

Figure 5.16 A comparison of the presented data at (c) 104 MeV and (d) 113 MeV, with the theoretical calculation by Pandey and Rustigi[48], which includes relativistic corrections to the interaction Hamiltonian.

Chapter 6

Conclusions

6.1 Assessment of the Tagged Photon Spectrometer

The experiment described in this thesis was the first carried out using the Mainz microtron *tagged* photon spectrometer. The experimental results produced are in general agreement with previously produced experimental data, which employ the technique of using *tagged* photons. The new data provide an improvement on these results, since it covers a wider range in photon energies and a greater angular range. The systematic errors produced in the data are largely due to the uncertainty of the *tagging* efficiency during the taking of the data and in the subtraction of the carbon background in the CD_2 target. However, with a refinement of this technique, a considerably more accurate measurement of the photodisintegration angular distribution is possible using the experimental analysis method described in this thesis.

In this regard there are several areas which may be highlighted. The key to the use of the spectrometer is in the stability of the *tagging* efficiency and in the reduction of background activity, to ensure a good real event to random event

ratio. *Tagging* efficiency can be controlled and optimised by accurate alignment of the microtron beam. Recent experimentation at the facility has shown that a *tagging* efficiency with a stability of better that 1 % is now possible. The reduction of the large electron induced background in the proton detector, can be achieved by the inclusion of more extensive shielding, by using a separate Δ E detector close to the target, or by employing the hardware electron reject circuit of the proton detector to greater effect.

6.2 The present $D(\gamma, p)n$ Measurement

In the present experiment some 25 hours of CD_2 data and 4 hours of carbon data were taken. The carbon photodisintegration data had a significant electron background, which resulted in poor statistics for the carbon background events under the deuteron ridge and with hindsight it is clear that the measurement would have benefitted from more carbon data. However, it must be emphasised that the present experiment was not only the first measurement performed using a completely new experimental faclity, but that the analysis of the data also required development of new techniques.

Theoretically one definite conclusion can be made; theories which do not include meson exchange effects are incomplete. The theoretical approach of Arenhövel which includes all explicit meson effect contributions to the cross section, gives the best agreement with the present data in the intermediate energy range within the angular constraints of the experiment. However, this theory is

in itself incomplete. Theories which attempt to provide a more comprehensive description of the deuteron photodisintegration process, such as those produced by Cambi, and Pandey and Rustigi, are not in agreement with the current data or indeed the data produced by other experimentalists. The current status of our theoretical understanding of the photodisintegration of the deuteron is clearly not satisfactory and until it is possible to include all of the major electromagnetic transitions, meson exchange effects, isobar configurations and relativistic effects, in the same calculation the situation is likely to remain confused.

6.3 Future Work

The conclusions of this thesis indicate that at present no one theoretical approach explains the deuteron differential cross section in the intermediate energy range. In the past much of the uncertainty derived from large variations in the experimental measurement of this quantity. The *tagged* photon spectrometer developed by the universities of Glasgow, Edinburgh and Mainz as a facility to be used with the 180 MeV Mainz microtron, has shown that it has the capabilities to produce measurements of the differential cross section of the photodisintegration of the deuteron over a wide range of proton emisson angles and incident photon energies, and to do this to an accuracy of better than 5% . Measurements of this precision and reliability are needed to clarify which theoretical approach provides the best explanation of the reaction. Perhaps however, the most exciting development will be to exploit the ability of the *tagged* photon spectrometer to produce linearly polarised *tagged* photons. Polarisation of the photon probe allows the experimentalist to examine the individual components which together produce the reaction amplitude describing the differential cross section.

In order to make a polarised beam available, since the spectrometer magnet system was designed with this feature in mind, it will only be necessary to modify the focal plane detection system to achieve this mode of operation. To operate in this mode the focal plane detector will have to be able to make out of the median plane position measurements and thereby enable the emission angles of the bremsstrahlung scattered electrons from the target to be identified. In a way this mode of operation is already possible, by raising or lowering the entire focal

plane detector, so that only electrons above or below the spectrometer median plane are detected. This method is possible if sufficient care is taken to provide shielding for the photomultipliers used in the focal plane detector, which will become exposed to the direct electron flux in the spectrometer.

The refinements suggested to the *tagged* photon spectrometer will allow an accurate, detailed and comprehensive measurement of the deuteron photodisintegration cross section in the intermediate energy range. This will hopefully provide a reliable testbed for new theoretical approaches explaining deuteron photodisintegration and increase our understanding of this process.

Appendix A

The kinematics of the photodisintegration of the deuteron are relatively simple, as there are none of the complications involved when a residual nucleus is present. Kinematically the break-up of the deuteron is overdetermined and when the reaction is considered in the center of mass frame, determinations of the energy and angle of the photoproducts are readily found.

In the lab frame, shown in Fig. A.1, an incoming photon of momentum $\mathbf{P}_\gamma$ is seen to produce a proton of momentum $\mathbf{P_p}$ and a neutron of momentum $\mathbf{P_n}$. To transform to the center of mass frame, shown in Fig. A.2 we must first determine a velocity which when applied to the lab frame , would bring the total momentum to zero. For convienience we put $c = \hbar = 1$. The velocity of a group (or of a single particle) can be shown to be,

$$V = \frac{P}{E}$$

So before the interaction,

$$V = \frac{P_\gamma + P_d}{E_\gamma + E_d}$$

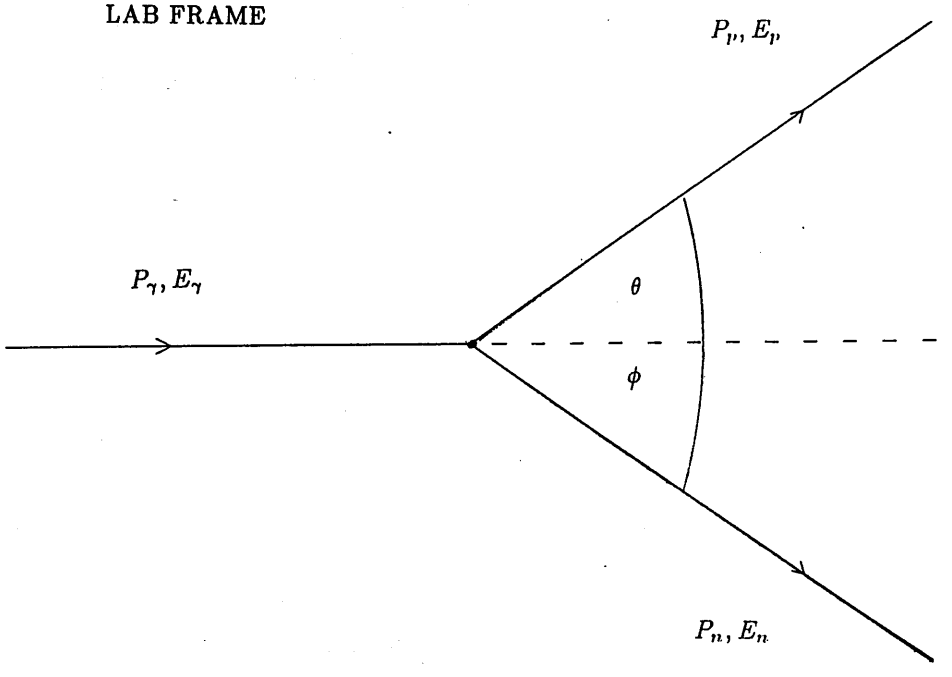

Figure A.1 The kinematics of the photodisintegration in the laboratory frame.

CENTER OF MASS FRAME

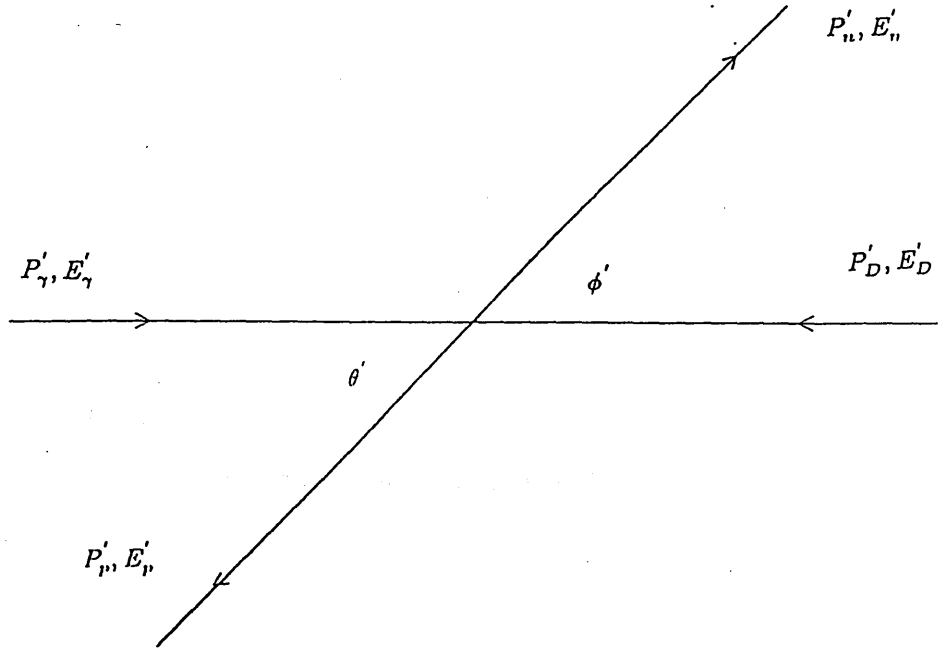

Figure A.2 The kinematics of the photodisintegration in the center of mass frame.

However, the deuteron is to a good approximation at rest so,

$$V = \frac{P_\gamma}{E_\gamma + E_{d_o}}$$

So we choose a velocity V in the z direction for the center of mass frame.

Quantities in the center of mass frame are denoted by a *dash*. Lorentz transforms of the momentum four vectors, relating lab and center of mass frames are given by,

$$E' = \gamma(E \pm V P_z)$$

$$P_x' = P_x$$

$$P_y' = P_y$$

$$P_z' = \gamma(P_x \pm V E)$$

where $\gamma = \frac{1}{(1-V^2)^{1/2}}$.

In the center of mass frame the total momentum is zero, so

$$P_\gamma{}' + P_d{}' = 0 = P_p{}' + P_n{}'$$

The total energy in the system, E_{tot}, is given by

$$E_{tot}{}^2 = E^2 - P^2$$

so,

$$E_{tot}{}^2 = 2E_\gamma{}' E_{d_o} - E_{d_o}{}^2$$

Also we know that,

$$E_{tot} = E_p{}' + E_n{}'$$

and

$$E_n{}^{2'} - E_p{}^{2'} = P_n{}^{2'} + E_{n_o}{}^2 - P_p{}^{2'} - E_{p_o}{}^2$$

using the above relations the energy of the proton and the neutron in the center of mass, can be found in terms of the energy of the incoming photon and the constants of the particles. Giving the relations

$$E_p' = \frac{E_{p_o}{}^2 - E_{n_o}{}^2 + E_{tot}}{2E_{tot}{}^2}$$

and

$$E_n' = \frac{E_{n_o}{}^2 - E_{p_o}{}^2 + E_{tot}}{2E_{tot}{}^2}$$

for the proton and neutron energies in the center of mass frame. The energy of the incoming photon is given by

$$P_\gamma{}' = \gamma(P_\gamma + V E_\gamma)$$

which reduces to

$$P_\gamma{}' = P_\gamma(1 + \frac{2P_\gamma}{E_{d_o}})$$

Using the Lorentz transforms and the above deduced equations, relations can be produced relating all center of mass quantities to lab frame quantities. The

most important of these in the context of this thesis is the conversion of lab proton emission angles to center of mass angles. So from Fig. A.2 we obtain the equations

$$P_{py}{}' = sin\theta_p{}'(E_p{}'^2 - E_{p_o}{}^2)^{1/2}$$

$$P_{pz}{}' = cos\theta_p{}'(E_p{}'^2 - E_{p_o}{}^2)^{1/2}$$

Transforming P_{pz} and P_{pz} into the center of mass frame we have

$$P_{py} = P_{py}{}'$$

$$P_{pz} = \gamma(P_{pz}{}' + VE_p{}')$$

So dividing we get

$$\frac{P_{py}}{P_{pz}} = tan\theta_p$$

Substituting for $P_{pz}{}'$ and $P_{pz}{}'$, and then simplifying we can obtain the relation

$$tan\theta_p = \frac{sin\theta_p{}' \frac{E_{tot}}{E_\gamma + E_{d_o}}}{cos\theta_p{}' + \frac{E_\gamma E_p{}'}{(E_\gamma + E_{d_o})(E_p{}'^2 - E_{po}{}^2)^{1/2}}}$$

This equation reduces to a quadratic equation in terms of $cos\theta_p{}'$, where the only unknown is the laboratory angle θ.

Bibliography

[1] J.L. Matthews, D.J.S. Findlay, S.N. Gardiner and R.O. Owens, Nucl. Phys. A267 (1976) 51.

[2] M. Anghinolfi, P Corvisiero, G. Ricco, M Taiuti and A. Zucchiatti Nucl. Phys. A399 (1983) 66.

[3] H.W. Koch and J.W. Motz, Rev. Mod. Phys. 31 (1959) 920.

[4] I. Hughes *et al*, Nucl. Phys. A267 (1976) 329.

[5] J.W Weil and B.D. McDaniel, Phys. Rev. 92 (1953) 391.

[6] R.J. Cence and B.J. Moyer, Phys. Rev. 122 (1961) 1634.

[7] J.S. O'Connell, P.A. Tipler and P. Axel Phys. Rev. 126 (1962) 228.

[8] H. Beil and R. Bergere, Report CEA-N-2144, CEN Saclay, France, (1980).

[9] L.S. Cardman, Photon Tagging, Present Practice and Future Prospects. Presented at the Magnetic Spectrometer Workshop, Williamsburg, Virginia, USA, (1983).

[10] D. Branford, Nuclear Physics Summer School, St Andrews, Scotland, (1983).

[11] G. Matone, Proceedings of the Workshop on Intermediate Energy Nuclear Physics (1980).

[12] L. Frederici, *et al*, Nuovo Cimento B59 (1980) 247.

[13] M.P. De Pascale, *et al*, Appl. Phys. B28 (1982) 151.

[14] The Fabrication of a Very High Energy Polarised Gamma Ray Beam Facility and a Programme of Medium Energy Physics Research at the National Synchrotron Light Source, Dept of Physics, Brookhaven National Laboratory (1982).

[15] J. Ahrens, Linear Polarisation of Tagged Bremsstrahlung Radiation, Internal Report of the Max Planck Institut, Mainz, West Germany, (1982).

[16] J. Arends *et al*, Nucl. Instrum. Meths. 361 (1982) 201.

[17] T. Terasawa, Laboratory of Nuclear Science Tohoko University, Japan. Submitted to Nucl. Instrum. Meths.

[18] R.L. Gulbranson, PhD Thesis, University of Illinois.

[19] T. Tamae *et al*, IEEE Trans. on Nuclear Science No 4 (1983) 3235.

[20] H. Herminghaus *et al*, Nucl. Instrum. Meths. 138 (1976) 9.

[21] J.D. Kellie *et al*, Nucl. Instrum. and Meths. A153 (1985) 161.

[22] H. Enge, Nucl. Instrum. Meths. 162 (1979) 161.

[23] S.L. Wan, Glasgow University, private communication.

[24] K.L. Brown and C.H. Iselin, CERN Report 74-2 (1974).

[25] I. Anthony, Glasgow University, private communication.

[26] P. Wallace, Glasgow University, private communication.

[27] I.J.D. MacGregor *et al*, Nucl. Instrum. and Meths. A262 (1987) 347 - 352.

[28] F. Zettl, MESS4, Data acquisition from Camac systems. Institut Für Kernphysik, Universität Mainz.

[29] G. Liesenfeld, PAUS, Data analysis and display program for Camac systems. Institute Für Kernphysik der Universität Mainz, West Germany.

[30] J. Vogt, Institüte Für Kernphysik, Universität Mainz. J.C. McGeorge, I.J.D. McGregor, I. Anthony, S.N. Dancer and A.McPherson, Glasgow University, BEAUTY, A data analysis program for the Mainz Tagged Photon Spectrometer.

[31] F. Partovi, Ann. of Phys. 27 (1964) 79.

[32] T. Hamada and I.D. Johnston, Nucl. Phys. 34 (1962) 382.

[33] A.J.F. Seigert, Phys. Rev. 52 (1937) 787.

[34] M.M. Giannini and G. Ricco, Nuovo Cimento Vol 8, N.4 (1985).

[35] J.C. Keck and A.I. Tollestrup, Phys. Rev. 101 (1956) 360.

[36] A. Whalin, B.D. Schriefer and A.O. Hansen, Phys. Rev. 101 (1956) 377.

[37] Iu.A. Aleksandrov *et al*, Sov. Phys. JETP 6 (1958) 472.

[38] L. Allen Jr, Phys. Rev. 98 (1955) 705.

[39] J. A. Galley, Phys. Rev. 117 (1960) 7631.

[40] M. Sanzone, Proceedings of the Fifth Course of the International School of Intermediate Energy Nuclear Physics, Wurll Scientific, (1985).

[41] H.P. Noyes, Nucl. Phys. 74 (1965) 508.

[42] H. Arenhövel, Nucl. Phys. A 374 (1982) 521.

[43] H. Arenhövel, Z. Phys. A 302 (1981) 25.

[44] R. Kose, W. Paul and K. Stockhorst, Z. Phys. 202 (1967) 364.

[45] P. Dougan, V. Ramsay and W. Stiefler, Z. Phys. 280 (1977) 341.

[46] H. Arenhövel , Institut Für Kernphysik, Universität Mainz private communication.

[47] J.M. Greben and R.M. Woloshyn, J. Phys. G: Nucl. Phys. 9 (1983) 643.

[48] L.N. Pandey and M.L. Rustigi, Phys. Rev. C 32 (1985) 1842.

[49] M.L. Rustigi *et al*, Phys. Rev. 120 (1960) 1881.

[50] A. Cambi, B. Mosconi and P. Ricci, Phys. Rev. Let 48 (1982) 462.

[51] A. Cambi, B. Mosconi and P. Ricci, J. Phys. G: Nucl Phys 10 (1984) L11 - L15.

[52] E. De Sanctis *et al*, Phys. Rev. Lett. 54,15 (1985) 1639.

[53] J. Chadwick and M Goldhaber Nature 134 (1934) 237.

[54] H.O. Meyer, Phys. Rev. C. 31 (1985) 309.